ABSTRACT

Title of Document: MICROCANTILEVER BIOSENSORS WITH CHITOSAN FOR THE DETECTION OF NUCLEIC ACIDS AND DOPAMINE

Stephan Koev, Master of Science, 2007

Directed By: Professor Reza Ghodssi
Department of Electrical and Computer Engineering

Abstract:

Microcantilever biosensors allow label-free detection of analytes within small sample volumes. They are, however, often limited in sensitivity or specificity due to the lack of proper bio-interface layers. This thesis presents the use of the biopolymer chitosan as a bio-interface material for microcantilevers with unique advantages. Sensors coated with chitosan were designed, fabricated, and functionalized to demonstrate two distinct applications: detection of DNA hybridization and detection of the neurotransmitter dopamine.

The first demonstration resulted in signals from DNA hybridization that exceed by two orders of magnitude values previously published for sensors coated with SAM (self assembled monolayer) interface. The second application is the first reported demonstration of using microcantilevers for detection of the neurotransmitter dopamine, and it is enabled by chitosan's response to dopamine electrochemical oxidation. It was shown that this method can selectively detect dopamine from ascorbic acid, a chemical that interferes with dopamine detection in biological samples.

MICROCANTILEVER BIOSENSORS WITH CHITOSAN FOR THE DETECTION OF NUCLEIC ACIDS AND DOPAMINE

By

Stephan Todorov Koev

Thesis submitted to the Faculty of the Graduate School of the
University of Maryland, College Park, in partial fulfillment
of the requirements for the degree of
Master of Science
2007

Advisory Committee:
Professor Reza Ghodssi, Chair
Professor John Melngailis
Professor Gregory Payne

Acknowledgements

First, I would like to thank my advisor, Prof. Reza Ghodssi, and the rest of my thesis committee members: Prof. John Melngailis and Prof. Gregory Payne. I acknowledge the Laboratory for Physical Sciences and the National Science foundation for funding this work. Next, I would like to thank our collaborators at the University of Maryland: Prof. William Bentley, Prof. Gary Rubloff, Dr. Hyunmin Yi, and Dr. Li-Qun Wu. I also thank the cleanroom staff at the University of Maryland Nanocenter and the Laboratrory for Physical Sciences for assistance with microfabrication. Next, I would like to thank my colleagues at the MEMS Sensors and Actuators Lab (MSAL) at the University of Maryland for helpful discussions. Finally, I thank my family and friends for their continued support.

Sincerely,
Stephan Koev

May, 2007.

Table of Contents

List of Tables

List of Figures

Chapter 1: Introduction

1.1 Overview

The emerging field of Bio Micro Electro Mechanical Systems (BioMEMS) has the potential to revolutionize sensors and actuators for life sciences applications. By employing fabrication techniques similar to those in the integrated circuit industry, MEMS technology makes it possible to create devices in large numbers, with small size and cost but with high sensitivity and performance [1-3]. MEMS components can manipulate matter on the size scale of biological cells and macromolecules, enabling great spatial and temporal control over biological processes. Their capabilities far exceed those of conventional benchtop laboratory techniques; they offer advantages such as high sensitivity, parallel processing, and small sample volumes. Among the successful demonstrations of BioMEMS devices are various biosensors [4-6], micro reactors [7], drug delivery platforms [8], and neural probes [9]. They have the potential to be used for fundamental biological studies (genomics, proteomics, immunology, cytology, histology), in clinical applications (point of care diagnostics, high throughput screening) and in environmental monitoring (food and water quality control, biohazard detection).

One of the major opportunities for BioMEMS lies in the field of biosensors. According to the IUPAC definition [10], a biosensor is a sensor which has biological components (e.g. cells, organelles, or macro molecules) and detects their interaction with the analyte by using a dedicated transduction mechanism (e.g. electrochemical, optical, thermal). Using MEMS can greatly increase sensor density and sensitivity while reducing the size and cost of almost all types of biosensors over their conventional macroscale counterparts. Biosensors are broadly classified by the biological components used and by

the transduction mechanism. The most common transduction mechanisms are optical, electrochemical, magnetic, capacitive, acoustic, and recently micromechanical. The main advantages of micromechanical sensors over the others is that they are label free and they can be miniaturized and arrayed by using MEMS fabrication. Although the field of micromechanical biosensors is rapidly advancing, one of the key challenges remains the integration of biological and nonbiological components. This step is critical since the biological components may lose their natural functionality when being immobilized on the microfabricated surface.

1.2 Thesis Accomplishments

This thesis presents the design, fabrication, and testing results of a micromechanical biosensor with the polysaccharide chitosan as an interface between biological and nonbiological components. The sensor is a microcantilever fabricated by conventional MEMS lithographic and etching techniques. The displacement of the cantilever is measured by optical interferometry. Chitosan is electrochemically deposited on the microcantilever and probe biomolecules are covalently coupled to it. The interaction of the analyte with the probe biomolecules is detected by the deflection of the cantilever (static mode) or the change in its resonant frequency (dynamic mode). The device is shown to successfully detect two different analytes: hybridized nucleic acid and the neurotransmitter dopamine. In each case, it is demonstrated that the use of chitosan offers unique advantages over other biointerface materials and could potentially enhance the performance and functionality of micromechanical biosensors.

1.3 Background

In this section, the context of the thesis research is established. The main biosensors transduction mechanisms are briefly reviewed and the advantages of micromechanical biosensors are discussed. Next, the different micromechanical sensors are reviewed along with the commonly used biointerface layers. Finally, the target analytes of this study (DNA and dopamine) are introduced.

1.3.1 Biosensors Review

Biosensors take advantage of an immobilized biological element (e.g. cell, nucleic acid, or antibody) with an affinity for a given analyte. The binding of the analyte (e. g. another nucleic acid or protein) to the immobilized element is typically detected by optical, electrochemical, capacitive, acoustic, or mechanical means. Each of these transduction mechanisms has its strengths and limitations, and none of them can be applied to all biological affinity systems. Some of these mechanisms are very powerful on the macroscale but cannot be implemented in microscale devices. Even when miniaturization is technically feasible, some transduction mechanisms suffer in sensitivity from being scaled down while others benefit from it.

Optical biosensors typically operate in the fluorescence detection mode. The target molecules are tagged with a fluorescent label (fluorophore). The sample is illuminated with an excitation signal and the scattered (or transmitted) light is captured and analyzed. Since the fluorophore causes a characteristic frequency shift in the collected light, its presence can be determined from the light's spectral components. This technique is based on the well-established fields of fluorescent microscopy and DNA spotted arrays, and it has been implemented in BioMEMS devices by a number of authors [4, 11, 12]. Fluorescent detection has very high sensitivity, and even single molecule detection has

been reported [13]. Its major limitation, however, is the need to label the target molecules with a fluorophore. This greatly increases sample preparation times. Additionally, labeled target species are no longer in their intrinsic state and may behave differently from their unlabeled counterparts (especially for smaller molecules).

Another optical detection technique is surface plasmon resonance (SPR) [14, 15]. A plasmon wave along a metal surface is excited by coupling light at a specific angle with a prism. The binding of biomolecules to the metal surface is detected by the change in the critical coupling angle. The advantage of SPR detection is that it does not require the target molecules to be labeled. However, it requires a bulky optical coupling and measurement setup that cannot be implemented in a microscale device with existing technologies.

Electrochemical (also called amperometric) biosensors measure electrochemical currents to detect biochemical reactions [16, 17]. Their application is typically limited to detection of biomolecules that undergo reduction or oxidation reactions and cause a net current to flow. The operation can be extended to other biomolecules if they are tagged with redox labels [18]. These labels then undergo the necessary electrochemical reactions for detection. However, as in the case of fluorescent labeling, redox labeling complicates sample preparation and affects the properties of the biomolecules being tagged.

Capacitive biosensors measure the changes in capacitance of an electrode to which target biomolecules bind [5, 19]. The capacitance variations are caused by the dielectric properties of the added molecules or by their net charge. This method can be readily implemented on the microscale by field effect transistors (FET), which are simple and highly sensitive charge detectors. The resulting devices are called CHEMFETs [20].

Another advantage of these biosensors is that they enable label-free detection of the target molecule. However, capacitive biosensors require extensive calibration. Since the capacitance changes with solution properties (e. g. pH, temperature, and ion concentration) great care must be taken to separate these secondary effects from biomolecular binding events.

Acoustic transduction is also utilized by some biosensors for label-free detection. In SAW sensors [21, 22], a surface acoustic wave is generated by a patterned piezoelectric film, which is covered by a metal layer. The propagation of the acoustic wave is influenced by the binding of biomolecules on the metal surface due to the change in acoustic impedance. This change is measured electrically and the biomolecules are detected. This method, however, requires a large footprint (a few mm) to achieve sufficient coupling between electrical and acoustic signal and cannot be readily scaled down in size. Another biosensing transduction technique which may be considered acoustic is quartz crystal microbalance (QCM) [23, 24]. In these devices, the target molecules bind to the surface of a resonant piezoelectric crystal and reduce its resonant frequency due to the increased mass. Although QCMs were traditionally fabricated of bulk crystals, thin film piezoelectric microbalances have also been reported [25]. Thin film processing enables the fabrication of miniaturized QCM devices with MEMS techniques.

One disadvantage of acoustic sensors is that neighboring devices experience considerable crosstalk and interfere with each other. This makes them inappropriate for applications where multiple devices are required to operate in parallel to detect different analytes. Another issue with this type of biosensors is that they have significant acoustic

coupling with the solution medium. Any changes in the medium's acoustic parameters will have an effect on the response that has to be separated from biomolecular binding events.

Micromechanical biosensors use a micromachined structure such as a cantilever beam or membrane to which the target biomolecules bind. There are two detection mechanisms for this type of sensors: static and dynamic. In static mode [26-28], the displacement of the microstructure is changed due to the surface stress exerted by the biomolecules. In dynamic mode [6, 29, 30], the frequency response of the structure is changed due the added mass of the biomolecules, the modified mechanical spring constant, or the damping characteristics of the biomolecules. To measure the dynamic response, the structure is actuated and its displacement as a function of time or frequency is measured. One of the key advantages of micromechanical biosensors is that they allow for label-free detection. Although some of the other technologies reviewed earlier are also label-free (e. g. SAW, QCM, and SPR), they are not easily fabricated using MEMS techniques and their sensitivity does not always scale favorably with reduced sensor size. In addition, some of them suffer from large crosstalk, which prevents them from being densely arrayed.

Micromechanical biosensors can be readily microfabricated by conventional MEMS techniques in arrays [31]. Since they do not experience crosstalk, each sensor can be biofunctionalized to detect different target molecules, thus screening for multiple analytes in parallel. In addition, micromechanical biosensors considerably benefit in sensitivity from being scaled down due to the increase in their surface to volume ratio. The measurements of displacement in both the static and dynamic mode can be implemented

either on-chip with integrated sensors (e.g. capacitive, piezoresistive) or off-chip with a simple external setup (e.g. interferometry, optical lever). The continued improvement of micromechanical biosensors can lead to compact and disposable devices with the capability to detect multiple analytes with minimal sample preparation.

One of the disadvantages of micromechanical biosensors are that they currently have lower sensitivity than labeling techniques such as fluorescence, which has been reported for single molecule detection. However, few applications (mostly fundamental research) require such levels of sensitivity. For typical clinical applications and environmental monitoring, micromechanical biosensors have sufficient sensitivity. Another drawback is that they are susceptible to fluctuations of the environment. For example, pressure or humidity changes can cause a shift in their resonant frequency which has to be decoupled from biomolecule binding events. However, proper calibration and reference measurements can account for these effects [32, 33].

1.3.2 Micromechanical Biosensors Review

The idea of using mechanical structures for detecting chemical and biochemical events dates back to the 1940's. Norton proposed a hydrogen chemical detector based on a macroscale cantilever transducer in 1943 [34]. However, the inability to fabricate miniaturized mechanical structures at the time severely limited the sensitivity of this type of sensors. In the 1960's, Nathanson et al demonstrated the resonant gate transistor [35]. This device consisted of a microfabricated metallic beam suspended over a field effect transistor, which measured the cantilever displacement capacitively. The resonant frequency of the device was high (~30 kHz) and it could potentially be used as a sensitive detector. However, the fabrication of the beams was still a major technological challenge and this type of devices was not widely accepted at the time for sensing applications. In

the 1980's MEMS micromachining processes were developed based on the batch fabrication technologies of the integrated circuit industry [1, 3, 36]. This enabled the routine fabrication of micromechanical structures in large numbers and at low cost, leading to a boom in micromechanical sensor research. Comprehensive reviews of the recent work on micromechanical detection can be found in [33, 37].

Various types of resonant or deformable microstructures have been used for micromechanical sensing. Common examples are cantilevers (singly clamped beams)[38], bridges (doubly clamped beams) [39], and membranes (diaphragms) [40]. The cantilever is the preferred structure because it is minimally constrained and thus tends to produce the largest displacement. In addition, it is typically the easiest structure to microfabricate and it has the smallest footprint for a given stiffness. For these reasons, the majority of micromechanical sensor research has been based on cantilevers. For the remainder of this document, the terms *microcantilever* and *micromechanical* will be used interchangeably, although one is a subset of the other.

Detection of various chemical and biological analytes has been demonstrated with micromechanical sensors. Strembicke et al measured relative air humidity with resonant silicon dioxide cantilevers covered with a thin hygroscopic film [41]. The absorbed water mass caused a decrease in the resonant frequency approximately linearly with humidity. Thundat et al used silicon nitride cantilevers covered with gold to detect mercury vapor. The adsorption of mercury on the gold surface causes a surface stress, which bends the cantilever, and a mass increase, which reduces its resonant frequency [42]. Illic et al measured the frequency shift of a silicon nitride microcantilever to detect the binding of a single *E. Coli* cell with a mass of less than 600fg [43]. Similarly, Gupta et al used

micromachined silicon cantilevers to detect the adsorption of a single virus particle with a mass of approximately 9fg [6].

One of the major goals for the development of micromechanical sensors has been to increase their specificity. Sensors are useful only if they produce a signal in response to the target analyte but not to others. Since micromechanical structures are not inherently specific, they must be coated with materials with selective responsivity to different analytes. Biosensors exploit the high natural specificity of biomolecular recognition. Pairs of biomolecules such as DNA-DNA and antigen-antibody bind together only if they are complementary to each other. By immobilizing one of them on the cantilever surface (probe molecule), the sensor becomes selectively responsive to the other (target molecule). For example, Fritz et al reported specific detection of Immunoglobulin antibodies binding to Protein A immobilized on gold-covered silicon cantilevers [27]. Control experiments were performed to show the cantilevers covered with other proteins were not responsive to the antibodies. A number of authors have demonstrated immobilization of short single strand probe DNA on a cantilever and detection of the complementary target DNA [28, 29, 31, 38]. For example, Zhang et al immobilized 12-base oligonucleotides on gold-coated polymer cantilevers and used them for static mode detection of target DNA with nanomolar concentration. Control cantilevers with noncomplementary DNA showed no response, confirming that the detection was specific.

1.3.3 Biointerface Materials

1.3.3.1 Self Assembled Monolayers and Soft Lithography

The fabrication of microcantilevers and measurements of their static or dynamic characteristics are now well established MEMS processes. However, the integration of biological components to achieve biological recognition is still problematic. One simple

approach would be to physically trap the probe biomolecules by making the sensor surface highly absorbing. This method would hurt the specificity to detection severely since the surface would indiscriminately trap other molecules along with the desired probes. Controlled chemical coupling between the probe and the sensor surface is needed to ensure that only the desired probes are present. At the same time, all physical absorption effects should be minimized. Another challenge is that even if the probe biomolecules are coupled to the sensor surface, they may not preserve their functionality. These molecules naturally work in aqueous solution and when they are immobilized, its ability to recognize the target may be adversely affected. Therefore, selection of an interface material between the microfabricated surface and the biological component is one of the most critical tasks in the biosensor design.

In the majority of MEMS-based biosensor studies, the biomolecules are immobilized on the surface by the formation of self-assembled monolayers (SAM). Each probe molecule is often tagged with a thiol functional group (-SH). Thiols are known to bond to gold and form highly organized monolayers on gold surfaces. Other examples of this phenomenon are silane groups assembling on silica and phosphates on TiO_2. There has been considerable research on using the thiol chemistry for integrating biomolecules in MEMS devices [44]. One limitation is that the self-assembly process provides little spatial control due to the assembly of thiol-modified biomolecules on all exposed gold surfaces. Methods such as soft lithography have been developed to spatially control the assembly [45, 46]. A compliant polymer stamp is molded from a microfabricated master. The stamp is "wetted" with the desired biomolecule solution and then printed on the device surface. By this printing process, the assembly of the biomolecules is spatially

controlled. Complicated biomolecule patterns can be achieved by using a series of stamps, each wetted with a different solution. This approach has been very successful and is relatively simple to implement. However there are still some significant limitations.

Soft lithography is an inherently planar technique. Sloped or sidewall structures cannot make conformal contact with the stamp and cannot be properly biofunctionalized. Also, fragile unsupported structures such as the cantilevers of micromechanical biosensors would be broken by attempting to print on them. Although self assembly of thiolated molecules works for these structures, patterning by soft lithography does not. For example, if each cantilever in an array needs to be functionalized with different biomolecules, this is not easily achieved with self assembly techniques. Some authors have demonstrated micromanipulator-based approaches, in which a capillary is used to deposit the desired solution on the surface of each cantilever [31]. However, this is an inherently slow and serial process and is only feasible for small arrays.

Besides spatial patterning, there are other limitations of the self assembly technique for biomolecule immobilization. Atomic-level surface smoothness and cleanliness are required for the proper formation of a SAM. The properties of the solution in to which the biosensor is exposed have to be carefully controlled to prevent disassembly of the SAM (e.g. pH, ionic concentrations, temperature). The synthesis and characterization of the SAM requires sophisticated equipment. This may not be problematic for the research environment, but would limit the practical applications of biosensors containing SAM.

1.3.3.2 Chitosan

Chitosan is an alternative to the self-assembled thiol interface. It is an amino-polysaccharide derived from chitin, the structural material of the shells of crustaceans and insects. In fact, chitin is the second most abundant natural polymer after cellulose. The

use of chitosan for the biofunctionalization of MEMS was pioneered by a collaborative team at the University of Maryland: Dr. Reza Ghodssi's group at Electrical Engineering, Dr. Gregory Payne's group at UMBI, Dr. William Bentley's group at Chemical Engineering, and Dr. Gary Rubloff's group at Materials Science. Chitosan can be electrodeposited as a thin film, which provides accurate spatial and temporal control of the biofunctionalization. Biomolecules can be coupled to chitosan's amine groups before or after the deposition by standard or enzymatic chemistries. This makes chitosan a convenient interface between biological and nonbiological components.

Chitosan is obtained from chitin by deacetylation. During this process with high temperature and high pH, the acetyl groups of chitin are converted into amine groups (Figure 1-1). Commercially available chitosan has a degree of deacetylation around 80%. The repeating unit of the chitosan polymer is glucosamine, which is an amino sugar. Chitosan is purchased as a powder and dissolved in an acidic solution, with concentrations typically around 0.5% w/v.

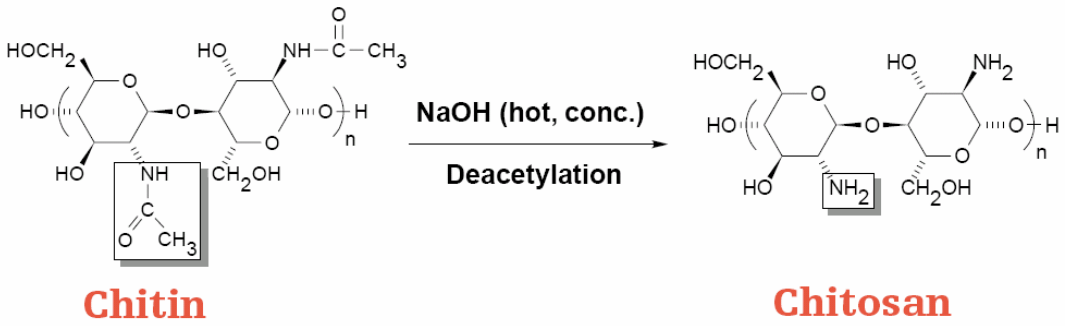

Figure 1-1. Deacetylation of chitin to convert it into chitosan. The acetyl groups become amine groups. Image from [47].

The amine groups of chitosan have a pKa of approximately 6.3. This means that below a pH of 6.3, the amines are positively charged and chitosan is soluble. The charge

density depends on the exact pH and the degree of deacetylation. At neutral and basic pH, the amines become deprotonated, making chitosan insoluble. Due to this pH dependent solubility and its positive charges, chitosan can be electrically deposited as shown in Figure 1-2. In an electrochemical cell with chitosan solution, a pH gradient is established at the cathode due to H^+ ion consumption. Since the positively charged chitosan chains are attracted to the cathode and the pH is raised above the pKa there, chitosan solidifies at the cathode surface. The compactness of the deposited film depends on the extent of the pH gradient. For large applied potentials, the pH is raised significantly and chitosan is solidified before being well compacted. This results in the formation of a thick hydrogel-like film [48]. For lower applied potentials, the pH increase is confined to a smaller region near the electrode and chitosan chains are well compacted before solidifying [49]. This results in a smooth and thin film. The electrodeposited films are stable under neutral and basic conditions, but they dissolve in acidic solutions (pH < 6.3).

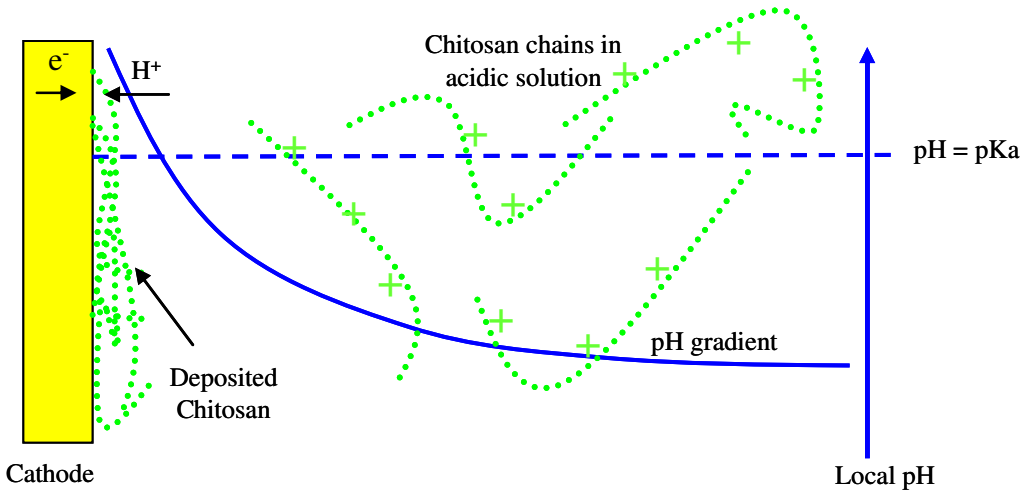

Figure 1-2. Schematic of chitosan deposition. A pH increase is created at the cathode by hydrogen ion consumption. The chitosan is attracted to the electrode and then solidified by the higher pH.

The original work on chitosan electrodeposition was performed by Wu et al using macroscopic electrodes [49]. They later showed that process has microscale resolution, and chitosan was deposited on micropatterned electrodes [50]. In addition to electrodeposition, the other significant property of chitosan is its ability to attach biomolecules to its amine groups. This attachment can be performed either before or after the deposition. Chen et al demonstrated enzymatic coupling of the protein GFP to chitosan (Green Fluorescent Protein) [51]. This protein-polysaccharide conjugate was then successfully electrodeposited. The resulting film was fluoresecent, indicating that the GFP folded correctly and preserved its properties. Yi et al demonstrated attachment of probe DNA to chitosan that is already deposited by using glutaraldehyde as a crosslinker between the amines on the chitosan and the amines on the DNA [52]. This immobilized probe was successfully hybridized with fluorescently labeled target DNA, indicating that its functionality was preserved. It was demonstrated that the DNA-chitosan coupling is extremely robust by denaturing the hybridized DNA in high-temperature urea solution and re-hybridizing.

Following the successful demonstration of biomolecule attachment on chitosan, it was used to biofunctionalize a photonic sensor by Powers et al [12]. The electrodeposition capability was exploited to place biomolecules on the sidewall of a microfluidic channel. Such a task would not be easily accomplished by soft lithography, which requires a planar surface. Kastantin et al used chitosan to biofunctionalize sites within sealed and packaged microfluidic channels [53]. The chitosan solution was flown through the channels and voltages were applied to selected electrodes. Again,

functionalization in sealed channels would not have been possible by soft lithography which requires an accessible surface.

The goal of this thesis research is to design and fabricate a microcantilever sensor taking advantage of the unique properties of chitosan. The major benefit of chitosan functionalization is that it has a large effective surface area for immobilization of biomolecules compared to SAMs due to its polymeric network. This leads to increased sensitivity of the microcantilever sensor. A second advantage of the chitosan interface for this application is that it is patterned by electrodeposition and not by printing. As previously discussed, soft lithography of SAMs is not feasible for fragile unsupported structures. Chitosan biofunctionalization only requires the structure to be electrically connected and works equally well for nonplanar or unsupported structures. This process could ultimately enable individual biofunctionalization of arrays of cantilevers that are electrically addressable. The third advantage of chitosan over SAMs is that it has improved chemical stability and does not require atomic-level surface cleanliness for its deposition. This property could lead to robust and reusable microcantilever biosensors.

1.3.4 DNA Detection

A wide variety of probe biomolecules can be coupled to chitosan by standard or enzymatic chemistries. For this study, DNA was chosen as the probe and target molecule since it is robust and forgiving to non-optimal experimental conditions. Similar methods can be used to immobilize proteins on chitosan and detect protein-antibody interactions. However, that would require considerable biological expertise and instrumentation since proteins are extremely fragile. In this section, the structure of DNA, role in the organism, and detection techniques will be briefly reviewed.

DNA (Deoxyribonucleic acid) is the molecule encoding genetic information in all known forms of life. Its structure was discovered by Watson and Crick in 1953 [54]. DNA is long polymer of 4 repeating nucleotides: Guanine (G), Adenine (A), Thymine (T), and Cytosine (C). The structure of the DNA molecule is shown in Figure 1-3. Each nucleotide consists of an aromatic ring base, a deoxyribose sugar, and a phosphate group. The phosphates and sugars link together to form the phosphate backbone of the DNA chain. The sequence of the nucleotides determines the genetic content. Groups of three consecutive nucleotides are called codons; each codon corresponds to an amino acid. Thus, DNA is a recipe for the synthesis of proteins from amino acids and uniquely identifies each living organism. The determination of the DNA sequence is of enormous importance in the fields of molecular biology, genetics, and forensics, among others.

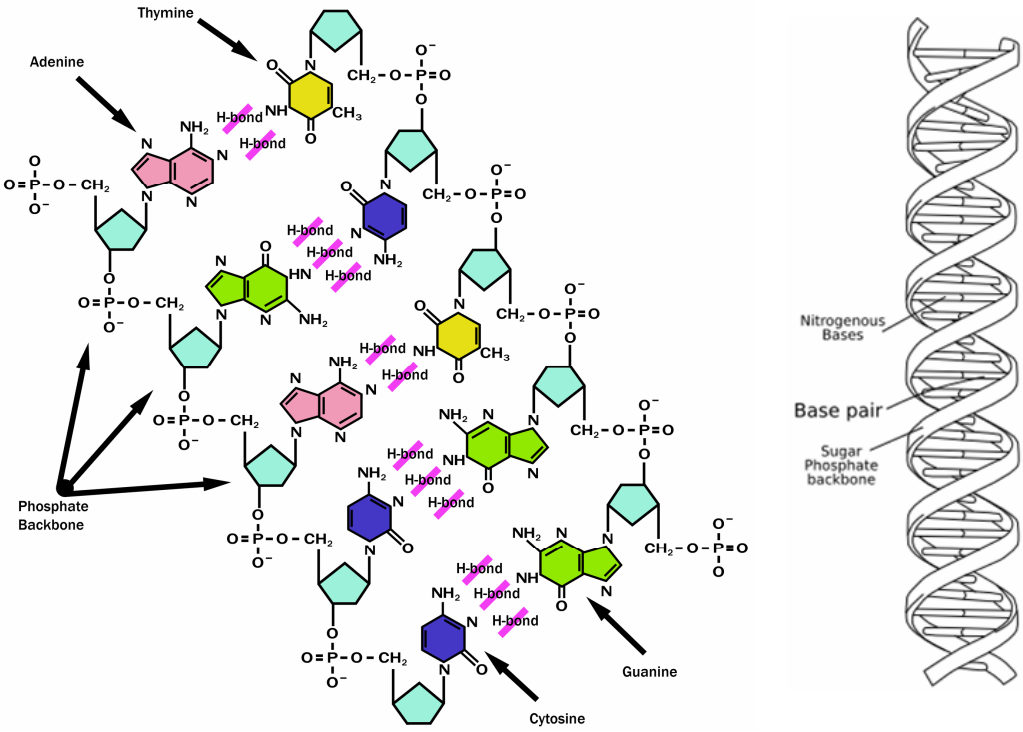

Figure 1-3. (Left) Molecular structure of each of the 4 DNA nucleotides and formation of hydrogen bonds. (Right) Double helix structure of DNA molecule formed by two complementary strands. Images reproduced from [55].

Typically, DNA occurs in the form of a double helix, in which two complementary strands are twisted together. DNA sequences are considered complementary if the A's and G's of one correspond to the T's and C's of the other, and vice versa. Since hydrogen bonds are formed between A and T nucleotides and between G and C nucleotides, complementary strands bind together and form the helix. This process is called hybridization. The helix formation facilitates replication of DNA during cell division, when the DNA of a cell has to be divided in two. During the division process, the helix is "unzipped" by enzymes, and each strand serves as a template for synthesizing a new strand, which forms a helix with the template. This results in two helices identical to the original, one for each new cell.

The binding of complementary DNA strands is used *in vitro* to check what nucleotide sequences are present in a sample. A DNA strand with a test sequence, called the hybridization probe, is exposed to the sample, also called the target. If the two sequences are complementary, the molecules hybridize. The binding of probe and target can be detected by any of the transduction methods listed in Section (1.3.1). One of the most popular techniques for hybridization detection is the DNA microarray [56], which is based on fluorescent labeling. Thousands of short probes (20 to 60 bases) with different sequences are immobilized on a chip by lithographic or printing methods. The target DNA's in the sample solution are labeled with a fluorescent marker and are introduced to the probe chip. The array is imaged with an optical scanner, and the fluorescence spatial distribution is recorded. The DNA sequences present in the sample are then determined from the fluorescence pattern.

The microarray method enables rapid detection of DNA sequences in parallel. However, it requires labeling of the probes with fluorescent markers, which makes sample preparation difficult and laboratory-intensive. As discussed previously, micromechanical transducers can potentially enable the same task without the labeling step. This would greatly simplify sample preparation and allow for DNA sequence determination outside the laboratory. Portable DNA detection would be useful for a large range of applications such as environmental monitoring, pathogen detection, and forensics.

1.3.5 Dopamine Detection

In addition to detecting DNA hybridization, the chitosan microcantilever sensor developed in this research is used to detect the neurotransmitter dopamine. In this capacity, the device is not truly a biosensor because it has no biomolecules attached to the chitosan film. It takes advantage of the crosslinking of the chitosan film by dopamine oxidation products. The crosslinking creates mechanical stress in the chitosan, causing the cantilever to bend; the presence of the dopamine is inferred from this bending.

Dopamine is one of the major neurotransmitters in the central nervous system and is being extensively studied by neurobiologists [57]. *In situ* dopamine detection techniques with high temporal resolution and specificity are still needed. The dopamine molecule is shown in Figure 1-4. It has been suggested that dopamine is part of the brain's reward mechanism and movement control. Dopamine regulation has also been linked to Parkinson's disease and drug addiction. As a neurotransmitter, dopamine is a signaling molecule between neurons. Signals travel along neurons as electrical potentials. However, when the end of the neuron is reached, neurotransmitter molecules are released into the

synapse (junction) between two neurons. The receiving neuron detects the transmitter and initiates its own electrical potential.

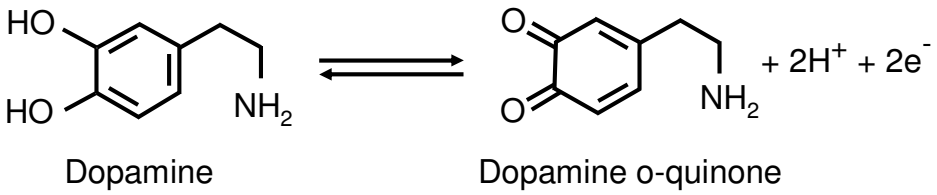

Figure 1-4. Dopamine oxidation results in o-quione. The reaction is reversible (adapted from [36])

Dopamine in nerve tissues and cultures can be detected by microdialysis. This technique consists of extracting a small sample from the tissue through a capillary and analyzing it by common laboratory methods such as chromatography. Using this approach, one can analyze the content of the sample with great accuracy. However, the temporal resolution is very poor (on the order of minutes), while the dopamine release processes occur on a time scale of seconds.

A faster dopamine detection technique is cyclic voltammetry, which is based on electrochemical oxidation and reduction of the analyte [58]. Much of the current understanding of dopamine's role in the brain was acquired using this method. A microelectrode is inserted into the sample tissue, a voltage is applied to it, and the current is measured. The voltage is swept back and forth repeatedly, while the current is being continuously recorded. Since electrically active molecules go through oxidation and reduction at characteristic potentials, the shape of the cyclic voltammogram can indicate which molecule is present and at what concentration. This technique has temporal resolution on the order of milliseconds. However, voltammetry has one major limitation: if the redox potentials of two molecules are close, it cannot recognize them from each other. For example, ascorbic acid (vitamin C), which is common in nerve tissues, has an

oxidation potential very close to that of dopamine. As a consequence, the two substances cannot be resolved by voltammetry, and large errors can occur in the determination of dopamine concentration.

This project demonstrates that micromechanical transduction can increase the specificity of dopamine electrochemical detection. Wu et al discovered that chitosan is crosslinked by the products of the electrochemical oxidation of some phenols [59, 60], including catechol and dopamine. The process is similar to the quionone tanning and hardening of insect shells, which is initiated by enzymatic oxidation of catecholic compounds. Briefly, electrodeposited chitosan on an electrode is placed in a dopamine solution and a positive potential is applied to it. The dopamine diffuses through the chitosan film and is oxidized at the electrode surface; the oxidation products react with the chitosan and crosslink it (Figure 1-5). First, the chitosan close to the electrode is crosslinked. As the oxidation continues, the crosslinking moves outward and eventually the whole thickness of the chitosan film is reacted. Wu et al demonstrated that the crosslinking changes the color and the mechanical properties of the chitosan film [59, 60]. Here, this change in mechanical properties is used to detect the electrochemical oxidation selectively. The chitosan film is deposited on the surface of a microcantilever sensor, which bends in response to changes in film stress.

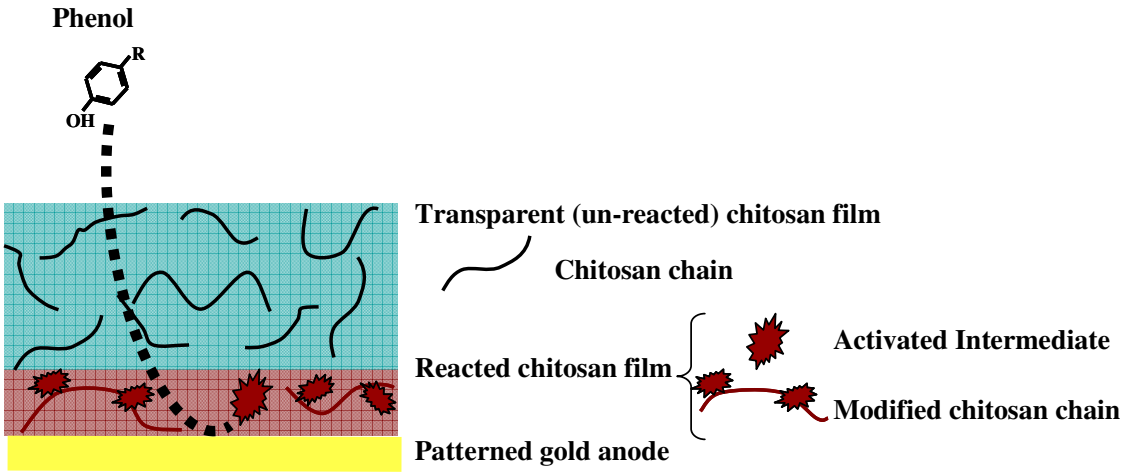

Figure 1-5. Electrochemical oxidation of phenols at a chitosan-coated anode generates products that crosslink the chitosan film at the anode surface. If the oxidation is continued long enough, the whole chitosan film is crosslinked. Adapted from [60].

Ascorbic acid is also electrochemically oxidized at the anode. However, the products of that reaction do no react with the chitosan film, its mechanical properties remain unchanged, and the microcantilever sensor does not bend. This phenomenon can be used to discriminate between the oxidation of dopamine and that of non-catecholic compounds. The mechanical detection has a temporal resolution on the order of seconds, which is sufficient for neurotransmitter release monitoring. Although this approach cannot compete with cyclic voltammetry in terms of speed, it has increased specificity. Both the voltammetry and mechanical detection methods are based on electrochemical oxidation of the analyte; therefore, they can potentially be used in parallel.

1.4 Thesis Organization

This chapter has introduced the operating principles of microcantilever biosensors and the major biointerface materials. The next chapter will present the sensor design and analysis. Chapter 3 will describe in detail the fabrication of the sensors and the experimental procedures for biofunctionalization and testing. Chapter 4 will focus on

experimental results. Finally, Chapter 5 will summarize the work and discuss potential improvements.

Chapter 2: Design

This chapter presents the design and analysis of the microcantilever biosensor. The structural materials, geometries and dimensions are introduced, and first-order analytical models of the device in both static and dynamic mode are presented. The method of measuring resonant frequency and displacement is briefly described since it influences design considerations.

2.1 Design Considerations

Micromechanical sensors can operate in static or dynamic mode. In static mode, the presence of the analyte is detected by the deformation of the structure, and in dynamic mode by a shift in resonant frequency. In this project, the sensor is designed for both modes because each has inherent advantages. In static mode, the measurements are simpler and can be performed in solution, close to physiological conditions. In dynamic mode, the samples must be dried before measurements to avoid the large damping of the liquid medium; this limits the applicability of the sensor. However, the dynamic mode is more sensitive and the experimental results are easier to interpret.

As discussed in the introduction, there are a large variety of possible micromechanical structures that can be used for sensing such as cantilevers [38], bridges [39], and membranes [40]. For this work, the cantilever was chosen because of its large compliance. A cantilever is a beam clamped at one end and free to move at the other. For a given device size and thickness, cantilevers tend to have smaller spring constants than other structures. This results in large displacements for a given force, which improves the relative measurement accuracy in both static and dynamic modes.

2.1.1 Cantilever Actuation

For the static mode of operation, a single measurement of the cantilever displacement is sufficient for detection. However, for the dynamic mode, the cantilever has to be actuated at different frequencies to find the resonant frequency. Electrostatic actuation was chosen for this purpose due to its simplicity and fast response time. For electrostatic actuation, a capacitor is formed between two electrically isolated but conducting structures. A voltage is applied between them, which causes opposite charges to accumulate on the two structures and attract each other. Since the force varies inversely with distance squared, electrostatic actuation produces negligible forces on the macroscale but works well for microscale devices. Note that this mechanism only produces attractive forces, since it is not possible to charge both plates of the capacitor with the same charge polarity [61, 62].

A first-order analysis is performed here to estimate the forces produced by electrostatic actuation. Assume that the capacitor formed by the cantilever and the substrate can be treated as an ideal parallel plate capacitor with air dielectric. This analysis assumes a uniform and constant electric field between the capacitor plates and ignores fringing fields at the edges. Also, it ignores the change in capacitor gap along the cantilever caused by bending.

Let each symbol have the following meaning: V-voltage applied between electrodes; C- capacitance; Q-charge of capacitor; W-electrostatic potential energy stored in capacitor; F – force between plates; y – separation between plates; A- area of plates; ε - dielectric permittivity of the capacitor. Equation 2-1 is a well-known expression for the

potential energy stored in a capacitor for a given voltage. Equation 2-2 shows the attractive force between the capacitor plates, derived from the spatial dependence of the potential energy. Equation 2-3 gives the capacitance of the ideal parallel plate capacitor as a function of plate separation. Using that expression, Equation 2-4 shows the attractive force between the plates for a given voltage and separation. These results are used in a later section to verify that sufficient cantilever displacement of approximately 1μm can be obtained with available actuation voltages (<100V).

Equation 2-1 $$W = \frac{1}{2}CV^2 = \frac{Q^2}{2C}$$

Equation 2-2 $$F_y = -\frac{dW}{dy} = \frac{Q^2}{2C^2}\frac{dC}{dy} = \frac{1}{2}V^2\frac{dC}{dy}$$

Equation 2-3 $$C = \frac{A\varepsilon}{y}$$

Equation 2-4 $$F_y = -\frac{V^2 A\varepsilon}{2y^2}$$

2.1.2 Structural Materials

Microcantilevers have been fabricated from many of the materials compatible with MEMS processing. Choices include various polymers [38], silicon [27, 31], silicon dioxide [63], silicon nitride [28, 30], and metals [64], to name a few. In this work, the requirements for electrostatic actuation and chitosan deposition had to be taken into consideration for the choice of materials. An electrode is needed on the cantilever and another electrode is required parallel to it to implement the electrostatic attraction. An electrode is also needed on the cantilever for chitosan deposition. One solution is to make the entire cantilever of a conductive material such as silicon; however, for static operation the chitosan has to be deposited only on one surface of the cantilever to produce a differential stress. If it is present on both sides, the two stresses will presumably cancel

each other and there will be no net displacement. Therefore, for static mode the cantilever must be conductive on one surface and not on the other.

The materials and processes chosen for the cantilever fabrication satisfy both the dynamic and static mode requirements. Figure 2-1 shows the cross section of a cantilever for dynamic mode detection of DNA hybridization. The device consists of layers of Si_3N_4, Cr, and Au on a Si substrate (with SiO_2 for stress matching). The devices for static mode detection of DNA and of dopamine are similar with the only difference being the pattern of the metal layer near the cantilever tip, as discussed in Section 2.4.

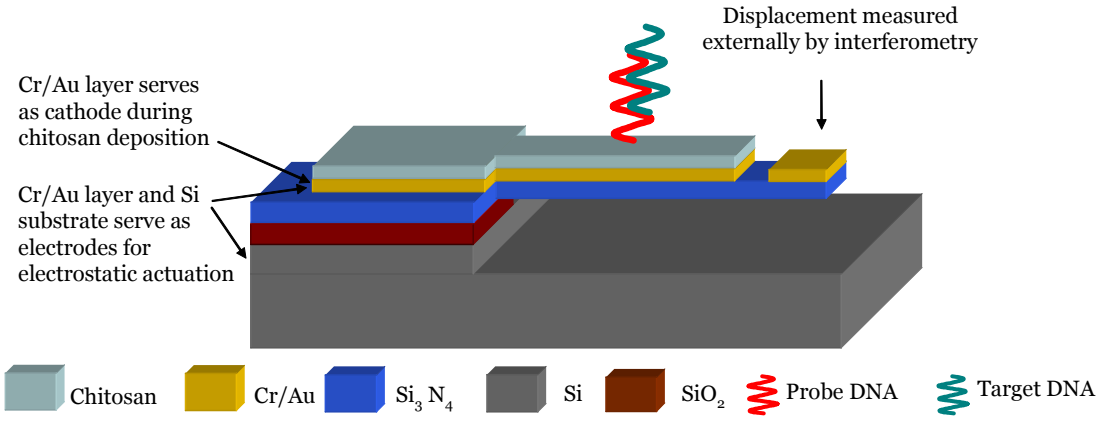

Figure 2-1. Cross section of microcantilever used for the detection of DNA hybridization in dynamic mode. Dimensions are given in Section 2.4.

2.1.3 Displacement Measurement

A number of methods have been developed to measure displacement of micromechanical structures. There are two fundamentally different approaches to this problem: integrating a dedicated displacement sensor within the device or measuring the displacement externally by optical means. Common examples of integrated displacement sensors are piezoresistive [65], capacitive [66], and optical waveguide [67, 68] devices. External measurement techniques are typically based on optical interferometry [69], laser Doppler vibrometry (dynamic only) [6], and position-sensitive optical detectors [43]. The

use of integrated sensors to measure cantilever displacement results in a compact and self-sufficient device; however it complicates device fabrication and is typically less accurate than external measurements. Since the goal of this work is to characterize the mechano-transduction with chitosan rather than to develop a standalone sensor, an external measurement method based on interferometry was chosen.

The measurements of cantilever displacement in this work are carried out using a Veeco Wyko NT1100 optical profiler (Tucson, AZ) with DMEMS (dynamic) module. This instrument is essentially a microscope with interferometric objectives (Figure 2-2). Beams reflected from the sample interfere with beams reflected from a reference mirror, creating an image with an interference pattern. The image is captured by a digital camera and analyzed in software to extract vertical heights of the sample. Dynamic samples cannot be measured real-time because of the slow response of the camera and software. Instead, they are imaged with stroboscopic illumination. A harmonically moving structure is actuated at a fixed frequency and is illuminated with a strobe light at the same frequency. The structure is then imaged as if it were stationary. Multiple measurements are taken at different actuation/strobe frequencies and phases to obtain the frequency response of the structure. The operation of the Veeco interferometer is described in more detail in Chapter 4.

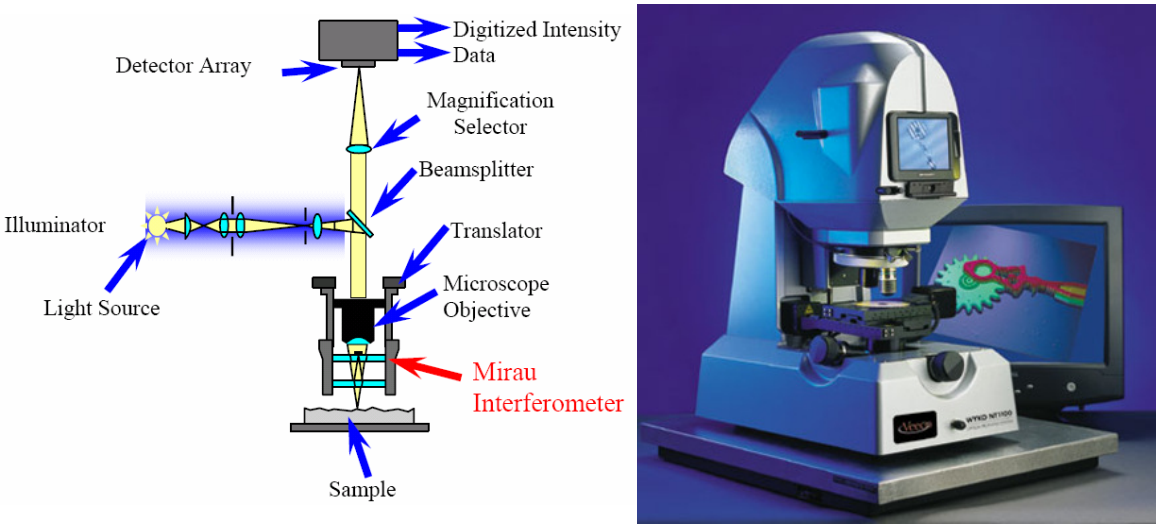

Figure 2-2. (Left) Functional schematic of Veeco Wyko interferometers. Obtained from [70] (Right) Photograph of actual Veeco Wyko NT1100 interferometer. Obtained from www.veeco.com.

The interferometric optical measurements generally require a clean reflective surface such as the chosen gold film for accurate results. Chitosan on the gold surface introduces some measurement errors because of its roughness and its low reflectivity. These errors are small in static mode but become significant in dynamic mode, as will be discussed in Chapter 4. For this reason, dynamic devices should be designed with a dedicated measurement area that is "chitosan-free". The Veeco interferometer theoretically has sub-nm measurement resolution. However, ambient vibrations in the laboratory cause a random error of several nm, limiting the useful resolution and accuracy. Both static and dynamic devices should be designed for a displacement of a few hundred nm to make the relative measurement error small.

2.2 First Order Analysis of Cantilever Beam

The analysis of cantilever mechanics was carried out using idealized beam theory [61, 71]. The basic assumptions of this theory are that the beam length is much greater than its

width and thickness, the bending of the beam is kept small compared to its dimensions, and that the beam is completely fixed at the clamping point (zero displacement). These assumptions facilitate the analysis and provide closed form solutions, but the results are only approximate for real structures. Other methods such as finite element modeling should be used if a more accurate solution is required. In this work, the exact solution of cantilever mechanics is not required and a treatment with idealized beam theory is sufficient. Since cantilever displacement and resonant frequency are experimentally measured before and after detection events, the theoretical analysis serves only as a design guideline. All the symbols and variables used in this section are defined in Table 2-1. Cantilever diagrams clarifying the notation are shown in Figure 2-3.

Table 2-1. Definitions of symbols

Symbol	Definition	Symbol	Definition
L	cantilever length	σ_t	surface mass density of target on cantilever
H	cantilever thickness	σ_s	surface stress caused by target
W	cantilever width	σ_f	film biaxial stress
I	moment of inertia about cantilever's neutral axis ($I = WH^3/12$)	Δz	displacement of cantilever tip from equilibrium
E	Young's modulus	F	Force
ρ	volume mass density	m	Mass
ν	Poisson's ratio	T	thickness of film
x	distance from cantilever base	M	moment about neutral axis of cantilever
w	displacement from neutral axis	ω	resonant frequency in rad/s
z	distance from cantilever central axis	f	resonant frequency in Hz
P	force per unit area	W_k	kinetic energy
ε	strain	W_e	elastic energy

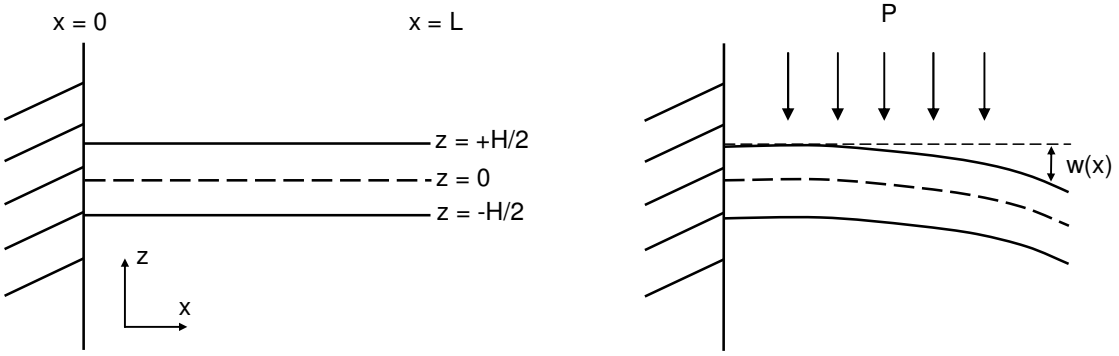

Figure 2-3. (Left) Cantilever beam without load. The distance from the neutral axis is z, and x is the distance along the cantilever. (Right) Cantilever beam under uniformly distributed transverse load. The bending of the neutral axis at point x is w(x).

According to [71] the beam displacement profile under a uniformly distributed force obeys Equation 2-5. The boundary conditions for a cantilever beam are *w(0)=0* and

dw/dx(0)=0. Using these conditions, we obtain the displacement profile of a cantilever (Equation 2-6) for a given load *P*. If the displacement of the tip only is considered, the cantilever behaves as a linear spring with a spring constant given by Equation 2-7.

Equation 2-5 $$\frac{d^4 w}{dx^4} = \frac{P}{EI}$$

Equation 2-6 $$w(x) = \frac{PWL^2}{4EI} x^2 - \frac{PWL}{6EI} x^3 + \frac{PW}{24EI} x^4$$

Equation 2-7 $$k_{eff} = \frac{F}{w(L)} = \frac{PWL}{w(L)} = \frac{8EI}{L^3}$$

The resonant frequency of a lumped mass-spring system in the absence of damping is given by the formula $\omega_o = \sqrt{k/m}$, which can be obtained from its equation of motion. However, this formula cannot be directly used for a cantilever because its mass experiences different amplitudes of oscillation at each point along the beam. The resonant frequency of a distributed mass spring system can be found by setting the maximum kinetic energy to the maximum elastic potential energy. This is known as the Rayleigh-Ritz method and is based on the observation that for an oscillating system the energy periodically transferred between kinetic and elastic [71]. The displacement of the cantilever from equilibrium at each point x is given by $w(x,t) = w(x)\cos(\omega t)$ for harmonic oscillations. The kinetic energy is obtained by integration of the point kinetic energy over the cantilever volume (Equation 2-8).

Equation 2-8 $$W_{k,\max} = \int_{volume} \frac{1}{2} \rho \left(\frac{\partial^2 w(x,t)}{\partial t^2} \right)^2 dxdydz = \frac{\omega^2}{2} \int_{volume} \rho w(x)^2 dxdydz$$

Similarly, the elastic energy is found by integrating the point elastic energy over the cantilever volume (Equation 2-9). Here, ε is the point strain and is given by Equation 2-10.

Equation 2-9 $$W_{e,\max} = \int_{volume} \frac{1}{2} E\varepsilon(x,z)^2 \, dxdydz$$

Equation 2-10 $$\varepsilon(x,z) = -z\frac{d^2 w}{dx^2}$$

Setting $W_{k,\max} = W_{e,\max}$, we can find the natural resonant frequency ω_o. This equation was solved in MATLAB symbolically, resulting in a resonant frequency given by Equation 2-11.

Equation 2-11 $$f_o = \frac{\omega_o}{2\pi} = \frac{9}{\sqrt{26}\pi}\sqrt{\frac{EI}{\rho HWL^4}} \approx 0.56\sqrt{\frac{EI}{\rho HWL^4}}$$

One complication to the analysis is that the cantilever in this case is made of multiple materials, which have different mass densities and Young's moduli. This can be taken into consideration by using an effective density and effective Young's modulus [72]. Here, E_i is the Young's modulus of each layer, I_i is its moment of inertia about the cantielver's neutral axis, ρ_i is its density, H_i is its thickness and N is the number of layers.

Equation 2-12 $$E_{eff} = \frac{\sum_{i=1}^{N} E_i I_i}{I}$$

Equation 2-13 $$\rho_{eff} = \frac{\sum_{i=1}^{N} \rho_i H_i}{H}$$

In the dynamic mode of operation the exact resonant frequency is not significant; rather the frequency shift upon loading is the essential parameter and is used for detection. Assume that the mass of target molecules is distributed uniformly on the cantilever surface with a density of σ_t. If the frequency shift Δf is small compared to the resonant

frequency, the cantilever sensitivity is given by Equation 2-14. Here we use the fact that the effect of σ_t is to change ρ. The factor *C* accounts for partial coverage of the cantilever by biomolecules (as in Figure 2-4) and becomes 1 for a completely covered cantilever.

Equation 2-14 $$\frac{\Delta f}{\sigma_t} \approx \frac{df}{d\sigma} = \frac{\partial f}{\partial \rho}\frac{\partial \rho}{\partial \sigma} = -\frac{f}{2\rho}\frac{1}{H}C$$

In the static mode of detection, bending of the cantilever is caused by biaxial stress in the chitosan film on its surface. The surface stress creates a bending moment *M* about the beam's neutral axis given by Equation 2-15 [73]. Here, the factor of (1-ν) accounts for the two components of the stress: parallel to the cantilever and perpendicular to it. The perpendicular component opposes the parallel component according to the Poisson effect. Equation 2-16 is the beam equation under a bending moment. Solving it with the cantilever boundary conditions results in Equation 2-17, which is commonly known as the Stoney equation [74]. This expression is in terms of surface stress, i.e. force per unit width of film. If the film stress is needed (i.e. force per unit cross sectional area of film), the chitosan film thickness *T* must be taken into account. Assuming that the stress is uniform throughout the film thickness, the film stress is given by Equation 2-18.

Equation 2-15 $$M = \frac{H}{2}\sigma_s(1-\nu)W$$

Equation 2-16 $$\frac{d^2w}{dx^2} = \frac{M}{E_{eff}I} = \frac{H\sigma_s(1-\nu)W}{2EI}$$

Equation 2-17 $$\Delta z = w(L) = \frac{1}{4}\sigma_s\frac{(1-\nu)HWL^2}{EI}$$

Equation 2-18 $$\sigma_f = \sigma_s / T$$

The preceding surface stress analysis assumes that the stiffness of the cantilever is determined by its structural materials, and the stiffness of the chitosan film is ignored. This assumption is justified since the Young's modulus of chitosan is much smaller compared to that of Si_3N_4. A typical value of E for chitosan is 12MPa [60], while for Si_3N_4 it is in excess of 200GPa.

2.3 Lumped Element Dynamic Model of Cantilever

To analyze the frequency response of the cantilever, it is useful to consider a lumped element model. It was already discussed that the cantilever behaves like a linear spring-mass system. If we take the effective spring constant as in Equation 2-7 and the resonant frequency to be Equation 2-11, the effective mass can be found by solving $\omega_o = \sqrt{k_{eff} / m_{eff}}$. The result for m_{eff} is given by Equation 2-19, where m is the actual mass of the cantilever.

Equation 2-19 $$m_{eff} = \frac{52}{81} m \approx 0.64m$$

In addition to the mass and spring terms, there is a damping force due to air friction and energy dissipation in the cantilever material. The damping effects are difficult to determine analytically and are usually estimated empirically. The equation of motion for the damped spring mass system is Equation 2-20, where b is the damping coefficient [75]. This can be rewritten as Equation 2-21, where Q is the quality factor ($Q = \sqrt{k_{eff} m_{eff}} / b$). Converting Equation 2-21 to the frequency domain, we obtain the transfer function given by Equation 2-22.

Equation 2-20 $$m_{eff}\, y''(t) + by'(t) + k_{eff}\, y(t) = F(t)$$

Equation 2-21 $$y''(t) + \frac{\omega_o}{Q}\, y'(t) + \omega_o^2\, y(t) = \frac{F(t)}{m}$$

Equation 2-22 $$H(j\omega) = \frac{Y(j\omega)}{F(j\omega)} = \frac{1}{m(\omega_o^2 - \omega^2 + j\omega_o\omega/Q)}$$

It can be shown [75] that if Q > 0.707, $H(j\omega)$ has a peak. The peak frequency, also called damped resonant frequency, is given by Equation 2-23 and the peak magnitude by Equation 2-24. It is $\omega_{\max}$ that is measured directly in experiments and not ω_o. However, in practice the two frequencies are very close. Q determines the width and height of the $H(j\omega)$ peak and, therefore, affects the accuracy of $\omega_{\max}$ measurement. It is desirable to maximize *Q*.

Equation 2-23 $$\omega_{\max} = \omega_o \sqrt{1 - \frac{1}{2Q^2}}$$

Equation 2-24 $$\left|H(j\omega_{\max})\right| = \frac{Q}{\omega_o^2 m \sqrt{1 - \frac{1}{4Q^2}}} \approx Q\left|H(0)\right|$$

2.4 Choice of Cantilever Dimensions

2.4.1 Dynamic Mode

Equation 2-14 shows that the cantilever sensitivity increases with increasing resonant frequency and with reducing both thickness and density of the structural material. Therefore, according to this model the cantilever should be made as thin and short as possible. However, decreasing the thickness generally leads to a reduction of the quality factor because the ratio of elastic and inertial forces to air damping forces is reduced. This, in turn, hurts the accuracy of measuring ω_{max}. An optimal design for a dynamic

mode cantilever would require empirical knowledge of the Q factor as a function of resonant frequency and thickness. The length of the cantilever also cannot be decreased arbitrarily due to fabrication and measurement limitations.

The final cantilever design is not optimized for sensitivity but rather for ease of measurement and experimentation. The total cantilever thickness was chosen to be 600nm; thinner structures are typically too fragile for handling in aqueous solution and suffer from stiction to the substrate. An array of test cantilevers with different lengths and widths was fabricated, placed in solution and dried. Cantilevers longer than 150µm consistently suffered from stiction, while devices shorter than about 100µm were increasingly difficult to measure with the interferometer due to magnification limitations. The optimal cantilever length was therefore chosen to be 100µm. Figure 2-4 shows the other relevant cantilever dimensions. All tested devices in Chapter 4 have these dimensions unless otherwise stated.

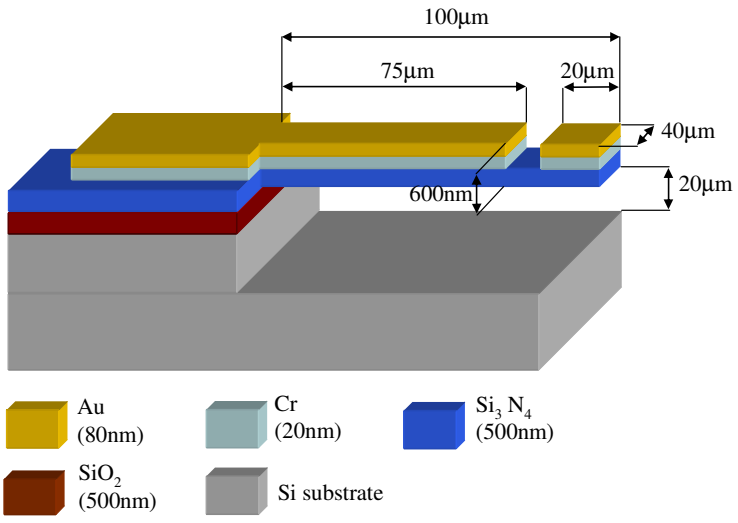

Figure 2-4. Schematic of microcantilever for dynamic mode detection with relevant dimensions indicated. Static mode devices are the same except the metal (Au/Cr) covers the cantilever completely.

At the tip of the cantilever an electrically isolated metal rectangle is defined with an area approximately 20% of the cantilever surface. This rectangle is used for displacement measurements in the dynamic mode since it does not experience deposition of chitosan and biomolecules, and it remains highly reflective. Chitosan has a rough surface, increasing error in dynamic interferometric measurements if the whole cantilever is coated. Note that this "clean spot" has a significant cost in terms of sensitivity to target biomolecule loading due to its location in the part of the cantilever with the largest displacement. The factor *C* in Equation 2-14 was found to be 0.31, i.e. the sensitivity to mass loading is decreased 3 times by the inclusion of the "clean spot". To maximize sensitivity, the clean spot could be reduced in size or moved to a different location on the cantilever.

Using the material properties commonly reported in literature (Table 2-2), the calculated resonant frequency of the cantilever is 60 kHz (from Equation 2-11), and the sensitivity is 63 Hz-cm^2/μg (Equation 2-14). The contribution of chitosan is ignored in this first-order analysis since the mechanical properties of chitosan and its surface topography vary considerably with deposition conditions. Note also that Young's modulus for chitosan (~12 MPa, [60]) and its density (<1g/cm^3) are far less than that of the structural materials and do not affect the resonant frequency significantly.

Table 2-2. Properties of structural materials of cantilever used for calculation of resonant frequency and stiffness. Values obtained from reference literature.

Material	*E* (GPa)	ρ (g/cm^3)
Si_3N_4	270	3.2
Cr	140	7.2
Au	80	19.3

The maximum voltage for electrostatic actuation of the cantilever is limited by the available high-voltage amplifier (100 Vpp max) and the breakdown voltage of the

dielectric materials. Since the breakdown field for Si_3N_4 and SiO_2 is on the order of 10 MV/cm [76] and they have a total thickness of 1μm, the amplifier is the true limitation on maximum voltage. The airgap (distance between cantilever and substrate) determines the attainable electrostatic actuation force for a given voltage (Equation 2-4). A small airgap is desirable since it results in large forces; however it should not be decreased arbitrarily because that leads to squeezed film damping and reduction of Q factor [77]. Due to cantilever fabrication process (described in a later section), the smallest attainable airgap is half the cantilever width – 20μm for this design.

It was already discussed that cantilever displacement of at least several hundred nm at the tip is desirable for measurements with the interferometer in dynamic mode. According to Equation 2-4, an AC voltage of 100V (peak-peak) provides a uniformly distributed load of approximately 440nN peak-peak. The spring constant of the cantilever is 1.2 N/m (Equation 2-7). For low frequencies, this results in a sinusoidal peak-peak displacement of 370nm of the cantilever tip. For frequencies close to resonance, this displacement is amplified by a factor of Q (Equation 2-24). From measurements on test structures with similar dimensions, it was observed that Q factors are typically > 10. Therefore, 100Vpp excitation would generate at least 3.7μm displacement of the cantilever tip at resonance, which is more than enough for dynamic optical measurement.

2.4.2 Static Mode

Equation 2-17 shows that the bending signal due to surface stress increases with length of the cantilever and with reducing thickness. However, as in the case of the resonant frequency operation, other factors such as stiction, cantilever fragility, and ease of measurement were taken into consideration when determining device dimensions. As a

result, the devices used for static operation have the same size as those for dynamic operation. They do not, however, have the isolated metal area at the tip and are entirely covered by chitosan. Since a narrowband illumination source is used for the interferometer in static mode, repeatable measurements can be taken even with chitosan on the surface. According to Equation 2-17, the expected displacement of the cantilever tip in static mode is 300nm per N/m of surface stress.

2.4.3 Mask Design

The final mask design includes a large number of cantilevers with varying dimensions and metallization patterns (in addition to the 100μm-long devices described above) to explore the design space. Some doubly clamped beams (bridges) were also included. All devices were organized in dies with dimensions 6mm x 25mm for convenient handling. Each cantilever has a metal pad with dimensions 400μm x 200μm at its base for making electrical contact with a micro probe (for chitosan deposition and actuation). Figure 2-5 illustrates the layout of two representative chips with different metallization patterns. Two optical masks (one for patterning the metal and one for patterning the Si_3N_4) were designed in L-Edit software and ordered from Microtronics (Newtown, PA).

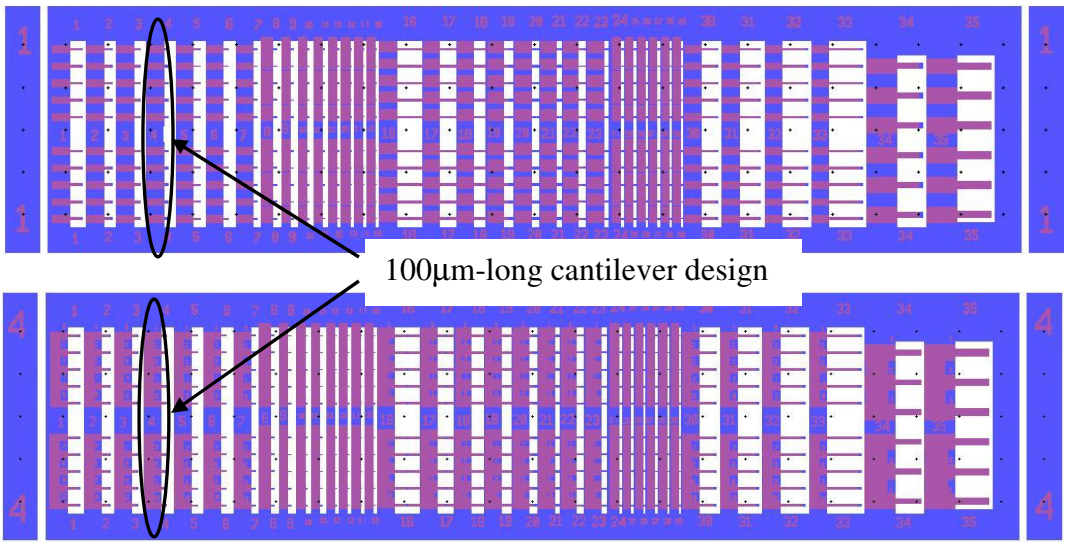

Figure 2-5. Layout of 2 dies with multiple cantilever designs in L-Edit software. The blue and red areas correspond to Si_3N_4 and metal films respectively; the white areas correspond to the Si substrate. (Above) Design with all cantilevers electrically isolated for individual testing. (Below) Design with 5 cantilever connected together for parallel testing.

2.5 Conclusion

This chapter has presented the design of the microcantilever sensor. The structural materials, actuation mechanism, and measurement method were described. The device was analyzed with a first-order model based on idealized beam theory to approximate resonant frequency, spring constant, and sensitivity to both mass loading and surface stress. In choosing the cantilever dimensions, care was taken to ensure that the device can be adequately actuated with reasonable voltages (<100V), and that it can be measured with available equipment (Veeco NT1100).

Chapter 3: Fabrication and Experimental Procedures

3.1 Introduction

This chapter presents in detail the fabrication of the microcantilever biosensor as well as the procedures for chitosan deposition, DNA functionalization and dopamine oxidation. Fabrication of microcantilevers is a mature MEMS process and a variety of methods have been demonstrated to date [33, 37]. In general, microcantilevers are fabricated from thin films on top of a "sacrificial film" deposited on the substrate [66, 78]. After patterning, the sacrificial film is etched to release the cantilever. However, sacrificial films are typically thin (a few μm) because of residual stress limitations. Thicker films tend to crack due to residual stress. As a result, the airgap (distance between released cantilever and substrate) formed by sacrificial release is small and causes squeezed air film damping [77]. Therefore, it is preferable to etch the substrate itself and form a large cantilever airgap.

Some authors remove the substrate under the cantilever completely by DRIE (Deep Reactive Ion Etching) from the back side of the wafer [79], by wet etching in KOH, or by peeling the cantilever layer from the substrate [80]. These methods overcome squeezed film damping by eliminating the airgap altogether, but the resulting structure cannot be electrostatically actuated. In this work, we remove the silicon substrate only partially by wet-etching it with KOH with a lithographic mask aligned along the [100] crystallographic direction. This allows us to enlarge the airgap considerably (20μm) to reduce squeezed film damping, while still allowing electrostatic actuation with

reasonable voltages as discussed in Chapter 2. To the best of our knowledge, this process for cantilever fabrication has not been demonstrated before.

The fabrication of the devices was performed at the MEMS Sensors and Actuators Lab (MSAL), the Institute for Research in Electronics and Applied Physics (IREAP), and the Laboratory for Physical Sciences (LPS).

3.2 Process Flow

3.2.1 Metal Patterning

The fabrication process flow of the cantilevers is summarized in Figure 3-2 at the end of Section 3.2. It begins with an n-type Si wafer (100 orientation, resistivity 0.01Ω-cm) with films of thermal SiO_2 (500nm) and LPCVD Si_3N_4 (500nm) on both sides. These custom wafers were purchased from the University of California at Berkeley fabrication facility. Next, 20nm of Cr and 80nm of Au films are deposited on the Si_3N_4 surface by sputtering. The Cr is used as and adhesion layer because Au has poor adhesion to Si_3N_4. The sputtering recipe used is shown in Table 3-1.

Table 3-1. Recipe for sputtering Cr and Au using AJA-100 Sputtering system at IREAP.

Parameter	Value
Base pressure	~1E-7 torr
Operating pressure	5 mTorr
Argon flow rate	20 sccm
Substrate distance	110 mm
Substrate clean	20 W, 1 min
Plasma DC power	200 W
Cr deposition rate	12 nm/min
Au deposition rate	49 nm/min

The sputtered metal is scanned by contact profilometry (Dektak 6M) to verify its thickness. Photoresist Shipley 1813 is then patterned to define the metal layer. The photoresist recipe is shown in Table 3-2. Note that the features on the mask are aligned

along the [100] direction of the Si wafer (at a 45° angle from the wafer flat); the reason for this is the KOH etch procedure explained later. The exposed metal (Au and Cr) is removed by wet chemical etching as described in Table 3-3. Note that the etch times are slightly longer than necessary to ensure that the metal is completely removed. The remaining photoresist is stripped with acetone followed by methanol and IPA rinse.

Table 3-2. Recipe for Shipley 1813 photoresist (PR) and processing equipment used. The nominal thickness of Shipley 1813 is 1.6 μm.

Step (Instrument model if applicable)	Parameters or chemicals used
Spin coat PR (Specialty Coating Systems P-6708D)	3000 rpm, 30s
Pre-bake (DataPlate 720 Hotplate)	100°C, 60s
Exposure (Quintel Q4000 contact aligner)	150 mJ/cm^2 @ 405 nm
Develop	Microposit 352 developer, 30 sec at 25°C
Strip PR	Acetone-Methanol-IPA

Table 3-3. Wet etching recipes used for microcantilever fabrication. The Au and Cr films were etched with specialized etchants from Transene Inc. (Danvers, MA).

Material	Thickness	Etchant	Duration of etch	Temperature	Average etch rate
Au	80 nm	TFA (Transene Inc.)	40 sec	25°C	170 nm/min (reported [81])
Cr	20 nm	TFD (Transene Inc.)	20 sec	25°C	300 nm/min (reported [81])
Si	20 μm	KOH (45% wt)	29 min	80°C	700 nm/min (measured)
SiO_2	500 nm	HF (concentrated 49% wt)	40 sec	25°C	1 μm/min (reported [82, 83])

3.2.2 Nitride Patterning

The Si_3N_4 and SiO_2 are patterned by Reactive Ion Etching (RIE). A second lithography step with Shipley 1813 (Table 3-2) is performed to define the RIE etch mask. This mask is aligned to the metal features already on the wafer with the help of alignment

markers. It is important to make sure that no metal is exposed to the RIE chamber at this step because it leads contamination of the tool. The metal is covered by PR almost everywhere on the wafer due to the overlap of metal and nitride mask patterns. However, the alignment markers at the metal and nitride levels do not overlap and some metal is exposed there. For this reason, the wafer with patterned PR is dipped in the Au and Cr etchants (Table 3-3) to remove the exposed metal. Next, the Si_3N_4 and SiO_2 films are etched using a CHF_3/O_2 RIE chemistry. The recipe for that process is given in Table 3-4. Following the RIE, the photoresist is stripped in acetone and rinsed with methanol and IPA. The wafer is then soaked in a Piranha solution for 5 min since RIE crosslinks parts of the photoresist and makes it insoluble in acetone. Piranha is a 5:1 mixture of H_2SO_4 and H_2O_2 which removes any organic residues by oxidizing them.

Table 3-4. Recipe for etching dielectric layers during cantilever fabrication using PlasmaTherm 790 Reactive Ion Etch system at LPS.

Parameter	Value
Operating pressure	40mTorr
Power	175W
CHF_3 flow rate	18 sccm
O_2 flow rate	2 sccm
Si_3N_4 etch rate	50 nm/min
SiO_2 etch rate	38 nm/min
Total etch time	28 min

3.2.3 Cantilever Release (KOH Etch)

Potassium hydroxide (KOH) etches single-crystal Si anisotropically. The etch rate of the (100) and (110) crystallographic planes is approximately 100 times faster than the etch rate of the (111) planes [61, 62]. This phenomenon is often exploited for the formation of V-grooves and vertical sidewalls by choosing a proper wafer orientation and mask alignment. KOH etching was chosen for the cantilever release here since it results in smooth planar surfaces and a uniform airgap. Isotropic Si etchants could also be used

to release the cantilever; however, their etch rate does not depend on the crystallographic orientation, the etched surfaces are not planar and the resulting airgap would not be uniform [62]. Note also that KOH does not attack Si_3N_4 and Au [82, 83]; therefore these materials do not need to be masked during the Si etch.

As mentioned earlier, the alignment of the lithographic mask is critical for KOH etching as it determines what Si crystallographic planes are exposed to the etchant. If formation of V-grooves with minimal mask undercutting is desired, the features on the mask should be aligned along the [110] direction (parallel to the wafer flat). Chuang et al [84] demonstrated release of cantilevers with similar size to the ones in this work by KOH etching with [110] aligned mask. As a result, deep V-grooves (~120μm) were formed under the cantilever after complete release; such large airgaps do not allow electrostatic actuation with practical voltages. In our work, however, the mask was aligned along the [100] direction (at a 45^o angle from the wafer flat) to maximize mask undercutting and speed up the cantilever release. Since the horizontal etch rate is approximately equal to the vertical etch rate, the minimal released cantilever airgap is approximately half the cantilever width. Airgaps of ~20 μm were realized using this technique.

A KOH bath was prepared by placing a 45% wt KOH solution on a hotplate with a magnetic stirrer and maintaining the solution temperature at $80^oC \pm 5^oC$. The wafer was immersed in the solution and periodically taken out to measure the etch depth by contact profilometry (Dektak 6M). The average measured etch rate of the Si (100) planes was 0.7 μm, and the final etch depth was 20μm ± 1μm. The complete release of the cantilevers

was confirmed by breaking several cantilevers with a micropositioning probe and scanning the silicon surface under them by contact profilometry.

Note that the release process described here results in cantilever dimensions different from what is defined on the mask. The reason is that the (111) planes in the corners near the cantilever base are etched slowly and remain exposed (Figure 3-1). This forms a triangular boundary, making the effective cantilever length approximately 20µm less than the structure on the nitride mask. This shortening was taken into account during mask design. Also, note that the nitride layer away from the cantilever is undercut by approximately 20µm due to the lateral etching of Si (Figure 3-1). As a result, the clamping condition for the fabricated cantilever is more complicated than the simple beam model of Chapter 2. However, for this work an exact prediction of cantilever mechanics is not necessary; the simple model still provides an adequate first-order estimate of the cantilever's properties, as will be shown in Chapter 4.

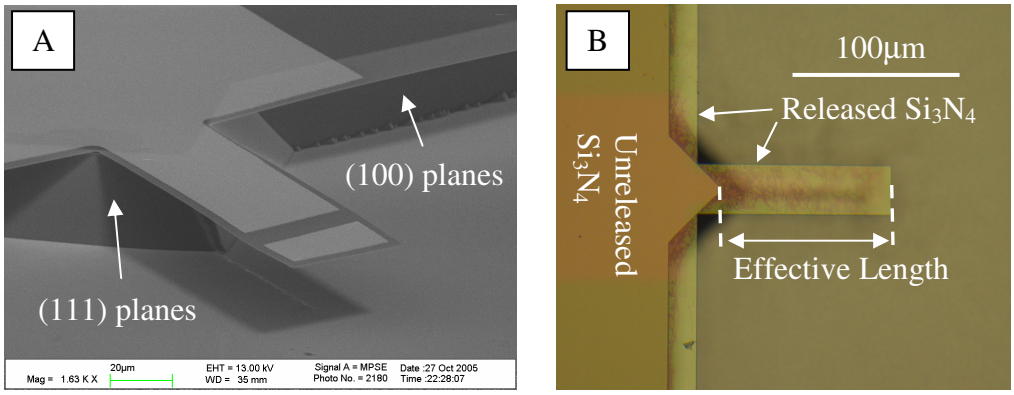

Figure 3-1. (A) SEM of fabricated microcantilever (side view). (B) Optical micrograph of cantilever (top view) with gold layer removed for clarity. Due to triangular boundary at the cantilever base after release, the effective length is decreased by ~20µm.

3.2.4 Oxide Removal

After KOH etching, the released cantilever consists of layers of SiO_2, Si_3N_4, and Cr/Au. The SiO_2 on the bottom has compressive residual stress, causing the cantilever to

bend out of plane considerably. This effect is undesirable as it complicates optical displacement measurements and makes the cantilever more likely to break during processing. The SiO_2 is etched with concentrated HF using the recipe in Table 3-3. After removing the SiO_2, the residual stress of the metal layer still causes some cantilever bending. However, that results in only 1μm upward displacement of the cantilever tip and does not impact optical measurements appreciably. The metal layer residual stress calculated from this bending is 30MPa tensile (using Equations 2-17 and 2-18).

3.2.5 Dicing

Finally, the wafer is diced in 6mm by 25mm chips to facilitate handling during the multiple biochemical reaction steps. A wafer saw (model Disco DAD321) at LPS is used for dicing. Prior to dicing, the wafer is covered in blanket photoresist (applied by squeegee) to protect the released cantilevers. After dicing, the protective photoresist is removed with acetone and the majority of cantilevers are observed to be intact. The chips are rinsed with methanol and IPA and blow-dried with nitrogen to minimize cantilever stiction to the substrate. The nitrogen flow rate is kept low to prevent cantilevers from breaking.

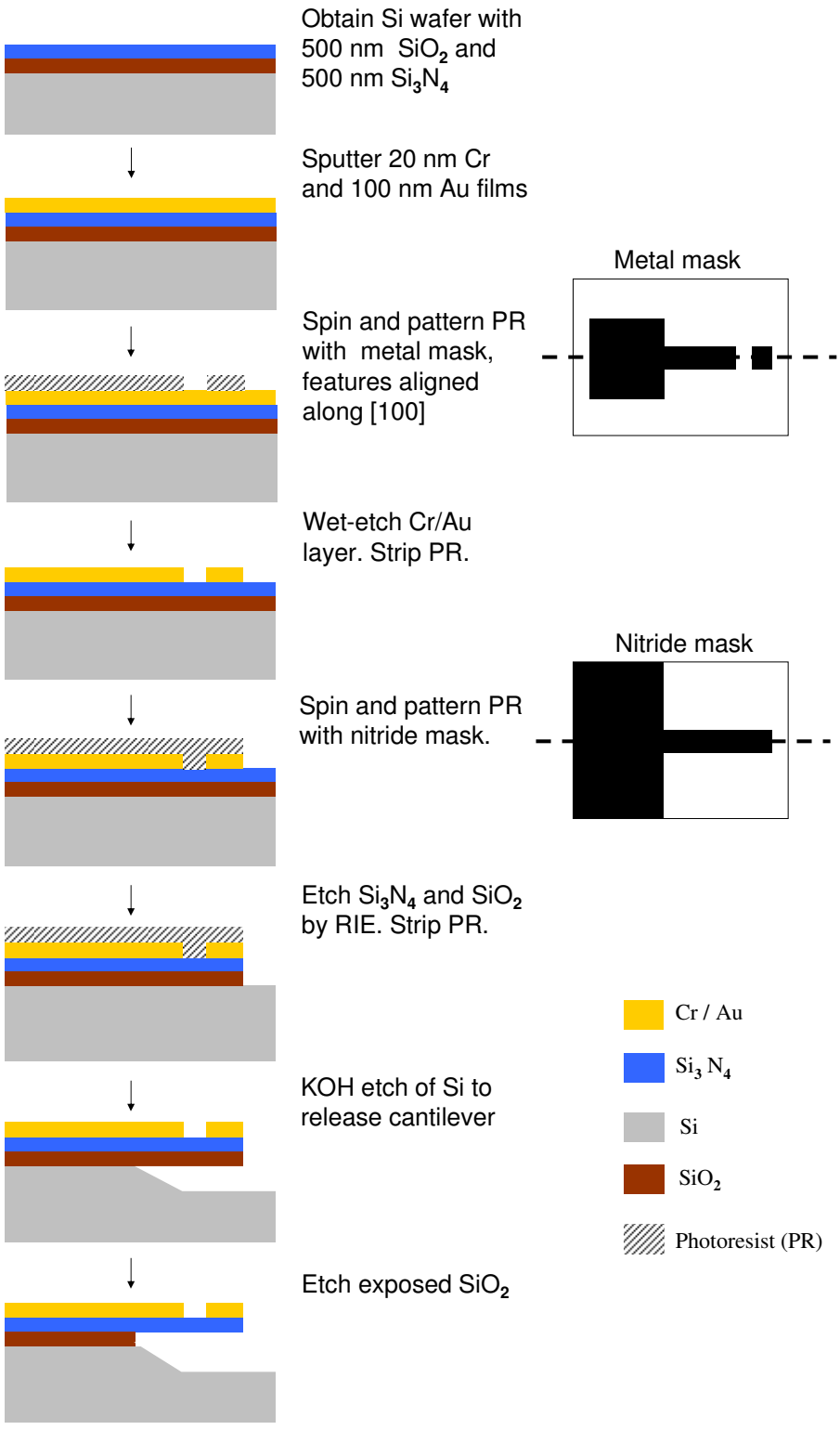

Figure 3-2. Fabrication process flow of cantilever. It consists of two lithography steps, one wet metal etch, one RIE dielectric etch, and one KOH silicon wet etch. The lithographic masks shown are for the dynamic mode cantilevers; the static mode devices do not have an isolated metal rectangle at the tip.

3.3 Fabrication Challenges and Solutions

3.3.1 Delamination of Gold

Initially, Ti was used as an adhesion layer for the gold instead of Cr. However, this resulted in delamination of the metal layer during the KOH etch (Figure 3-3A). Although the Cr is covered by Au and is not directly exposed to KOH, it may be etched at a sufficiently high rate from the sides. Note that according to [82], Ti becomes soft in KOH and fails. For further fabrication, Cr was used as and adhesion layer, and it survived all processing steps.

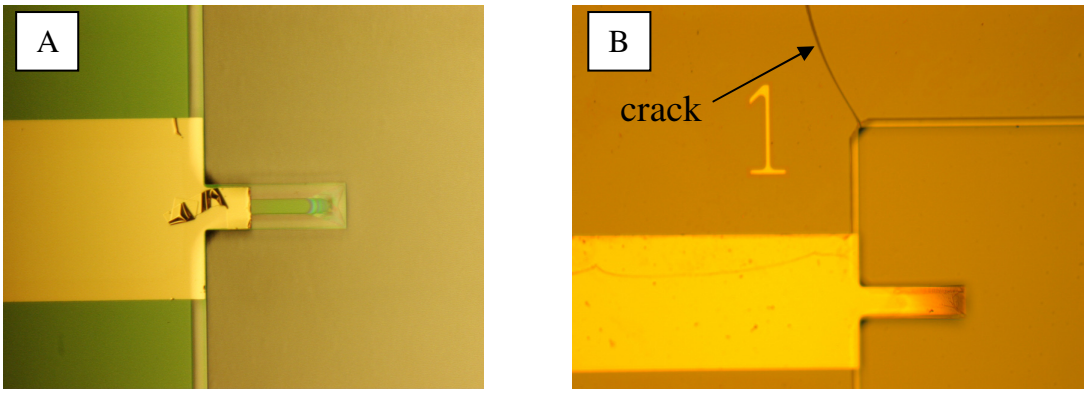

Figure 3-3. (A) Delaminated metal on partly released cantilever during KOH etch due to the use of Ti as adhesion layer. This problem was solved with use of Cr as adhesion layer. (B) Cracking of Si_3N_4 layer due to thermal stress during processing. This problem was solved by using wafers with low-stress Si_3N_4 from a different vendor.

3.3.2 Nitride Cracking

The initial supply of Si wafers with SiO_2 and Si_3N_4 did not yield satisfactory results. The films apparently had large residual stress and cracked during the RIE step (Figure 3-3B). Since the wafer temperature increases in the RIE chamber, the thermal mismatch stress of the already-stressed films causes them to fracture. Although the cantilevers themselves were rarely affected by the cracking, the cracks propagated along the gold contact pads and created continuity problems. Wafers with lower-stress films from a

different supplier (UC Berkeley) were used for further fabrication and no cracking was observed.

3.3.3 Breaking of Cantilevers During KOH Etch

Breaking of the cantilevers during the KOH etch was a considerable problem. Initially, the samples were diced prior to cantilever release, which is a common practice for MEMS devices. It was believed that the vibrations during the dicing would break cantilevers if they are already released. However, KOH etching of individual chips turned out to be problematic. The chips floated in the solution due to their small size, and the majority of cantilevers were broken by turbulence. KOH etching of an undiced wafer worked much better since it could be held in place, and the cantilevers were preserved. For dicing, the released cantilevers were protected with photoresist as described previously.

3.4 Chitosan Deposition

3.4.1 Deposition Setup

After fabrication, the cantilevers were coated with chitosan by electrodeposition. A brief description of chitosan was already given in Chapter 1, but here the deposition conditions are presented in more detail. Chitosan electrodeposition on the microscale was first demonstrated at the University of Maryland in 2002 [49] and is now a mature process. Prior chitosan electrodeposition work was successfully performed on fixed electrodes down to 20μm in size [48-50]. However, some adjustments had to be made to the deposition procedures in this project for two reasons.

First, the electrodes in this project are on top of cantilevers and are not firmly fixed on a substrate. Since residual stress in the chitosan film bends the cantilevers out of plane,

the chitosan thickness is limited to a few hundred nm (compared to several μm in "traditional" chitosan deposition). Large cantilever bending would prevent optical displacement measurements due to depth of focus limitations and also make the cantilever more likely to break (since it is already stressed).

Second, the electrode contact pads here are small (200μm) and are electrically connected to the power supply with micropositioning probes. In previous work, the contact pads were large (a few mm) and were connected with alligator clips. The small pads in this work were chosen to reduce the capacitance between the electrode and substrate (which would degrade electrostatic actuation) and to increase the number of devices per chip.

Figure 3-4A shows a functional schematic of chitosan deposition and Figure 3-4B is a photograph of the actual setup with a micropositioning probe (Cascade Microtech, Beaverton, OR). The chip is immersed in chitosan solution, and negative potential is applied to the desired cantilever-electrode. The potential, duration of deposition, and resulting thickness vary between experiments as discussed in the following sections. The chitosan solution was prepared by Dr. Hyunmin Yi at the Department of Materials Science and Engineering at UMD as described in [49]. Briefly, medium MW (molecular weight) chitosan flakes with 85% deacetylation from Sigma-Aldrich (St. Louis, MO) are dissolved in HCl overnight and the undissolved material is filtered. The solution is diluted to obtain 0.5% wt concentration of chitosan and the pH is adjusted to 5 by adding NaOH.

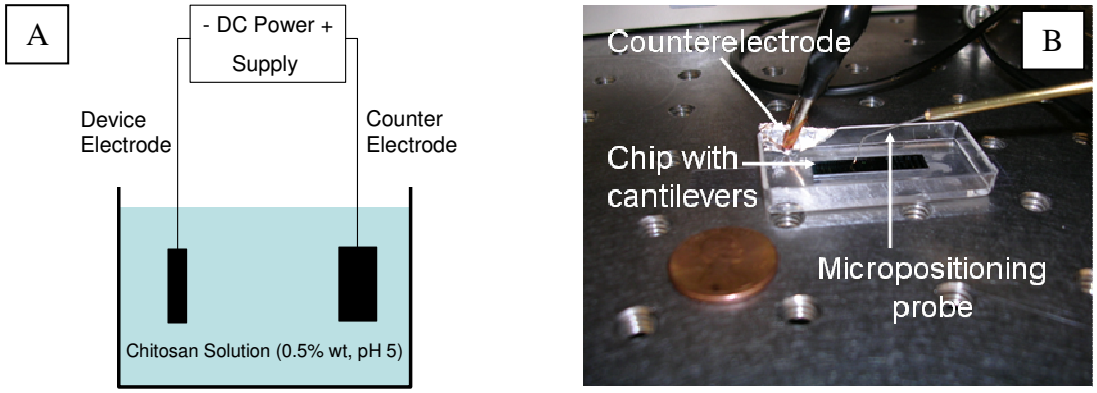

Figure 3-4. (A) Schematic of electrochemical cell for chitosan deposition. The chitosan is deposited on the cathode (device electrode). (B) Photograph of miniaturized chitosan deposition setup with micropositioning probe. A penny is shown for comparison.

3.4.2 Chitosan Thickness Measurements

As discussed above, chitosan thickness on the cantilevers must be controlled to prevent excessive cantilever bending. However, measurement of film thickness on the cantilever is a major challenge. Contact profilometry cannot be used directly on the cantilever, which is bent by the stylus force and the measurement becomes inaccurate. Optical (non-contact) profilometry also does not work due to the transparency of the chitosan film and the insufficient amount of light reflected from its surface. One possible solution is to coat the chitosan with a thin reflective film (e.g. sputtered gold) to enable optical profilometry. However, this method is destructive and prevents subsequent functionalization of the sample with biomolecules. Ellipsometry can measure the thickness of transparent films in a non-contact, non-destructive manner; however, knowledge of the refractive index is required. Chitosan's refractive index is not well known and varies with the deposition conditions.

Since chitosan thickness on the cantilever is difficult to measure, we measure the thickness on the pad at the cantilever base (Figure 3-5) by contact profilometry (Dektak 6M). This value is different from the thickness directly on the cantilever, but it is used as

an approximation. Knowledge of the exact film thickness on the cantilever is not needed as long as it is small enough to prevent excessive cantilever bending.

3.4.3 Chitosan Uniformity

Electrodeposited chitosan films are not uniform in thickness along the electrode. The electric field during deposition is higher near the electrode edges, causing higher current densities and faster deposition rates there. As a result, the chitosan film is thicker near the edges and thinner in the middle of the electrode. Figure 3-5B is a typical chitosan thickness profile and illustrates this effect. A similar geometry-dependent nonuniformity of deposited films has been observed in the process of metal electroplating [85, 86]. Some authors have proposed methods to combat this effect by shielding the electric field and improving the current uniformity at the electrode surfaces during electroplating [86]. Such methods should also be applicable to chitosan electrodeposition but were not explored in this work.

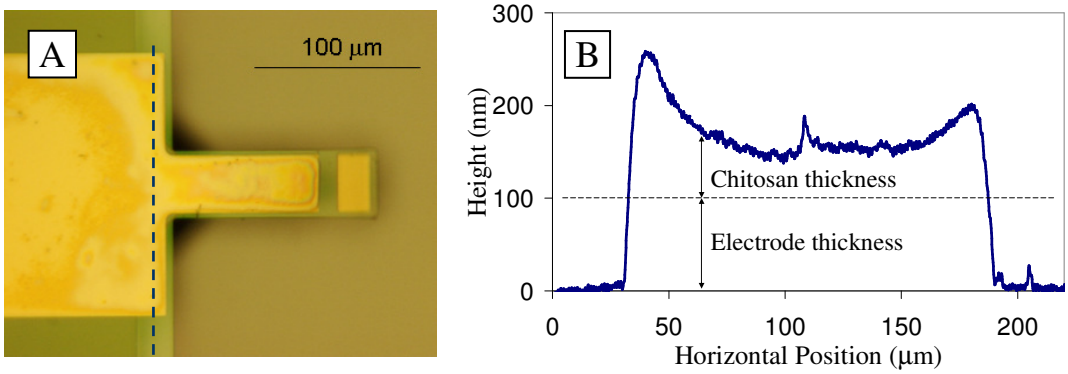

Figure 3-5. (A) Optical micrograph of cantilever after chitosan electrodeposition. The chitosan is deposited everywhere on the Au except at the electrically isolated tip. (B) Contact profiler scan of chitosan film along dashed line in A. Higher electric field near the edges increases the deposition rate and the resulting chitosan thickness there. Electrode thickness (100nm) is subtracted to obtain chitosan thickness only.

The chitosan film in this project serves as biological interface layer and is not required to be perfectly uniform. The two main requirements for the film are to have complete coverage on the cantilever (except the measurement spot at the tip) and to be thin enough to prevent excessive cantilever bending (due to residual stress). The chitosan nonuniformity, however, complicates these requirements. Due to the nonuniform rates of deposition across the electrode, the film is already tens of nm thick on some parts of the cantilever before it has even started forming on other parts. This effect limits the minimal film thickness that completely covers the cantilever.

The problem of partial coverage is illustrated in Figure 3-6. The micrographs in the figure are taken with Nomarski optics, also known as Differential Interference Contrast or DIC (Nomarski optics enhance the contrast of the transparent chitosan film by converting the optical path gradient into an intensity). The figure shows that as chitosan thickness is decreased, the spatial coverage of the electrode is reduced. The minimal film thickness that gives complete cantilever coverage (as in Figure 3-6B) is approximately 100nm (measured at the cantilever base). This thickness is acceptable as it results in cantilever upward bending of only 3μm at the tip after chitosan crosslinking. The cantilever bending should be less than 10μm for accurate displacement measurements with the optical interferometer introduced in Chapter 2.

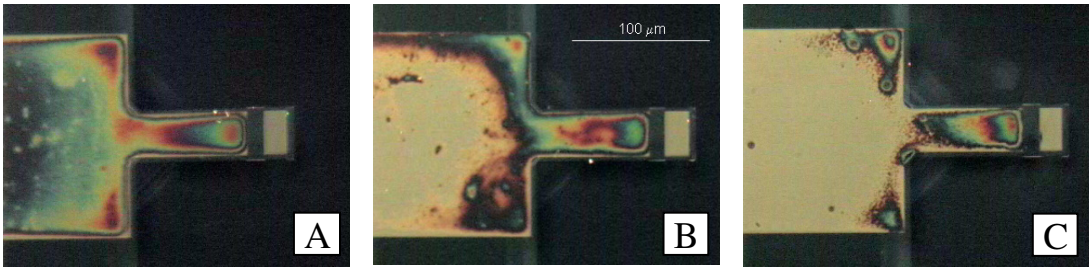

Figure 3-6. Photomicrographs (Nomarski optics) of microcantilevers with chitosan with different degrees of coverage and thickness (measured by contact profilometry). (A) Complete chitosan coverage on cantilever and contact pad, thickness ~250nm. (B) Complete chitosan coverage on cantilever and partial coverage on contact pad, thickness ~120nm. (C) Incomplete chitosan coverage on both the cantilever and the contact pad, thickness ~80nm.

3.4.4 Deposition Control and Variability

In previous chitosan deposition work, a constant current source was used to apply the potential [48, 50, 51] . This method was preferable to the use of a constant voltage source because the current density between experiments could be kept constant regardless of the potential drop across the solution. A constant current source was also used initially for this project, and the deposition current was varied to minimize the chitosan thickness on the cantilever. Table 3-5 shows chitosan thickness and roughness (measured at the cantilever base) for different experimental conditions. However, because of the small electrode sizes in this project, current control did not give consistent results. The probe tips immersed in the solution to make contact to the chip have a large area compared to the on-chip electrodes. This area varies depending on the level of the solution in the container (i.e. how deep the probes are immersed). Therefore, it is difficult to reproduce the effective electrode area between experiments; as a result the current density and chitosan deposition rate vary considerably even though the current is fixed.

Table 3-5. Chitosan thickness for different deposition conditions using constant current control. The thickness and roughness are measured at the cantilever base by contact profilometry.

Current (μA)	Duration (min)	Ave. thickness (nm)	RMS roughness (nm)	Coverage on contact pad	Coverage on cantilever
10	2	3100	130	complete	complete
10	1	2200	59	complete	complete
5	2	1300	70	complete	complete
5	1	710	41	complete	complete
2	2	400	47	complete	complete
2	1	220	32	patchy	complete
1	2	150	39	patchy	complete
1	1	90	28	patchy	patchy

The use of a constant voltage source in this project gave more consistent deposition results than the constant current source. In this approach, the same potential is applied between anode and cathode in each experiment regardless of the level of chitosan solution in the container. One complication is that the voltage drop across the solution (which depends on the electrode spacing) can change between experiments and influence the deposition rate. This is why voltage control was avoided in "traditional" chitosan deposition experiments, where the distance between the electrodes is large (a few cm) and hard to reproduce. However, in the miniaturized deposition setup (Figure 3-4B), this voltage drop is negligible due to the low currents and small distance between cathode and anode. As a result, the chitosan deposition rate is reasonably consistent between experiments. Table 3-6 shows the thickness and roughness of multiple chitosan films deposited on cantilever chips using the same electrode potential.

Table 3-6. Thickness and roughness of deposited chitosan films on cantilever chips using the same solution and the same deposition conditions (0.7V for 2min). Measured by contact profilometry at cantilever base. The standard deviation in thickness is 14 nm and in roughness 18 nm.

Depositon #	Average thickness (nm)	RMS roughness (nm)
1	150	39
2	172	32
3	155	78
4	143	54
5	147	27
6	181	58
7	154	73
8	136	34
9	170	45
10	145	33

The rate of chitosan deposition is determined not only by the applied potential but also by the solution properties (e.g salt concentration, pH, chitosan concentration, and chitosan molecular weight). The properties of the chitosan flakes used to make the solution differ from batch to batch, and they cannot be precisely controlled by the manufacturer (especially MW and degree of deacetylation). As a result, the solution properties and the chitosan deposition rates can vary considerably. For this reason, it is necessary to adjust the chitosan deposition parameters every time a new batch of solution is obtained. Multiple depositions are performed with varying potentials and times to "tune" the parameters. Although this procedure is tedious, it is needed only once for each batch of chitosan solution. When using the same solution, the deposition is reasonably consistent as shown above (Table 3-6).

3.5 DNA Functionalization

The first goal of this project is to detect the hybridization of target DNA to probe DNA immobilized on the chitosan-coated cantilever. The conjugation of probe DNA to chitosan was originally demonstrated by Yi et al [52] at the University of Maryland. The procedures used in this project are essentially the same as in the original demonstration;

the only differences are the DNA sequences and the method of detecting hybridization with target DNA (micromechanical detection in addition to fluorescent detection).

3.5.1 Oligonucleotide Samples

Figure 3-7 illustrates the DNA functionalization schematically, and Table 3-7 lists the DNA samples used. The surface probe DNA is attached to the chitosan (the chitosan and the surface probe both have amine groups, and they are covalently bonded with glutaraldehyde crosslinker). Two different sequences of surface probe DNA are used: *dnaK* and *6xHis*. The first encodes the *dnaK* gene in *E. Coli*, and the second encodes a hexahistide tag common for recombinant proteins. The target DNA has a region complementary to the *dnaK* surface probe and has little homology with the *6xHis* surface probe. Therefore, the target DNA is expected to hybridize with the *dnaK* probe but not with the *6xHis* probe. The sandwich probes are fluorescently tagged and are complementary to two regions of the target DNA. The sandwich probes hybridize with the target DNA and form a fluorescent target complex with an effective length of 110 bases and effective concentration 1.5μM. The purpose of the sandwich probes is to verify the hybridization of target to surface probe by fluorescence microscopy (in addition to quantifying the hybridization by the cantilever mechanical response). This technique is called “sandwich assay”.

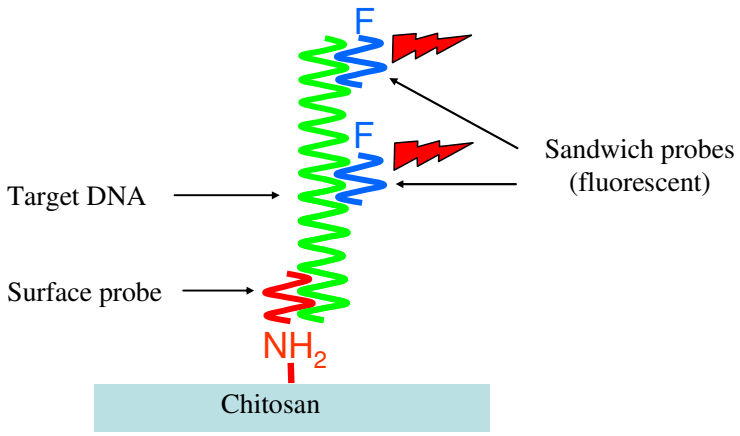

Figure 3-7. Schematic of DNA sandwich assay with fluorescent sandwich probes. The surface probe is amine-labeled and is conjugated to the chitosan via glutaraldehyde chemistry. The target DNA does not have any modifications. The sandwich probes are labeled with Fluorescein and serve to confirm the hybridization visually (in addition to the micromechanical detection).

Table 3-7. Oligonucleotides used in hybridization experiments. Sequences underlined with same style lines (dashed or solid) are complementary to each other. All sequences obtained from Gene Probe Technologies (Rockville, MD). The probe DNA is dissolved in SSC buffer and the target DNA in PerfectHyb buffer (see Table 3-8).

Oligonucleotide	Sequence and end modifications	Total bases	Concentration in solution
Surface probe (*dnaK*)	NH_2-5'-CTTTCGCGTTGTTTGCAGAA	20	20µg/mL
Surface probe (*6xHis*)	NH_2-5'- ATGATGATGATGATGATG	18	20µg/mL
Target (*dnaK*)	5'-GTAAGTTTGAAGAGCTGGTAGAA ATGTAAGTTTGAAGAGCTGGTAC AGACTTCTGCAAACAACGCGAAAG	70	1.5µM
Sandwich probe	FITC-5'-TACCAGCTCTTCAAACTTAC	20	6µM

3.5.2 Conjugation and Hybridization Procedures

The reagents used for DNA functionalization and hybridization in this project are listed in Table 3-8. The procedures followed for the surface probe conjugation to chitosan are described in Table 3-9 and those for hybridization of target to probe DNA in Table 3-10. Measurements of cantilever bending and/or resonant frequency are taken with the

optical interferometer introduced in Chapter 2. Hybridization is known to be a reversible process, and it can be undone by heating the sample in Urea solution. After hybridization, the target-probe duplex is denatured by placing the sample in a high-temperature, high ionic concentration solution (Table 3-13) and measurements are taken again. Measurement results will be presented in Chapter 4.

Table 3-8. Reagents used for the DNA functionalization and hybridization procedures.

Reagent	Properties	Source
Chitosan	medium MW (200kDa) 85% deacetylation 0.5%wt solution, pH 5	Sigma (St Louis, MO)
SSC Buffer	1x concentration 1M $MgCl_2$ added	Sigma (St Louis, MO)
PerfectHyb Plus Buffer	-	Sigma (St Louis, MO)
Glutaraldehyde	0.05% (v/v) concentration	Sigma (St Louis, MO)
Urea	4M concentration	Sigma (St Louis, MO)
NaOH (sodium hydroxide)	1M concentration	Fisher (Fair Lawn, NJ)
$NaBH_4$ (sodium borohidride)	400 μg/mL concentration	Fisher (Fair Lawn, NJ)
IPA (Isopropyl Alcohol)	99.8% concentration	Pharmco (Brookfield, CT)
DI (deionized water)	18 MΩ cm resistivity	E-Pure system, MSAL, University of Maryland

Table 3-9. Procedures for conjugation of probe DNA to electrodeposited chitosan. All steps are performed at room temperature unless otherwise noted.

Step	Procedure	Duration
1	Deposit chitosan on cantilever with micro probe (0.7V to 0.9V applied)	adjust for ~100nm thickness
2	Rinse with DI to remove excess chitosan solution	~10 sec, squirt bottle
3	Place in NaOH solution to neutralize chitosan film	5 min
4	Place in SSC buffer to stabilize pH	5 min
5	Place in glutaraldehyde solution to activate amine groups	30 min

6	Rinse with DI and place in SSC buffer to remove unreacted glutaraldehyde	10 min, rocking platform
7	Place in probe DNA solution. Schiff bases formed between DNA and chitosan.	12 hrs, 4°C refrigerator
8	Rinse with DI	~10 sec, squirt bottle
9	Place in $NaBH_4$ solution to convert Schiff bases into secondary amine bonds (more stable).	5 min
10	Rinse with DI and place in SSC buffer to remove unbound DNA	10 min, rocking platform
11	Rinse and place in DI to remove SSC buffer	10 min, rocking platform
12	(Optional) Rinse with IPA to minimize cantilever stiction upon drying	~10 sec, squirt bottle
13	(Optional) Blow-dry with nitrogen	~10 sec
14	Measure cantilever bending (in air or DI) or resonant frequency (in air)	-

Table 3-10. Procedures for hybridization of target DNA to probe DNA. All steps performed at room temperature.

Step	Procedure	Duration
1	Place in solution containing target DNA complex (target DNA and sandwich probe)	30 min
2	Rinse with DI and place in SSC buffer to remove non-hybridized target DNA	10 min, rocking platform
3	Rinse and place in DI to remove SSC buffer	10 min, rocking platform
4	(Optional) Rinse with IPA to minimize cantilever stiction upon drying	~10 sec, squirt bottle
5	(Optional) Blow-dry with nitrogen	~10 sec
6	Measure cantilever bending (in air or DI) or resonant frequency (in air)	-

Table 3-11. Procedures for denaturing hybridized target DNA. All steps performed at room temperature unless otherwise noted.

Step	Procedure	Duration
1	Place in Urea solution	30 min, 80°C water bath
2	Rinse with DI and place in SSC buffer to remove non-hybridized target DNA	10 min, rocking platform
3	Rinse and place in DI to remove SSC buffer	10 min, rocking platform
4	(Optional) Rinse with IPA to minimize cantilever stiction upon drying	~10 sec, squirt bottle
5	(Optional) Blow-dry with nitrogen	~10 sec
6	Measure cantilever bending (in air or DI) or resonant frequency (in air)	-

3.6 Electrochemical Oxidation of Phenols

As discussed in Chapter 1, the second goal of this project is to mechanically detect the neurotransmitter dopamine upon oxidation by its crosslinking of chitosan on microcantilever sensors. The reaction of chitosan with electrochemically oxidized phenols was originally demonstrated by Wu et al [60]. The same procedures are used here with minor modifications for reacting chitosan on microcantilevers. In particular, the oxidation times and voltages were reduced due to the small chitosan thickness on the cantilevers compared to that in the work of Wu et al.

The oxidation was performed in the same miniaturized electrochemical cell as the chitosan deposition (Figure 3-4) with a constant voltage source. However, for oxidation the cantilever electrode is biased as an anode (for chitosan deposition it is biased as cathode) and the container is filled with a phenol solution (instead of chitosan solution). Measurements of cantilever bending before and after oxidation were performed with the optical interferometer introduced in Chapter 2 either in air (after drying the sample) or in solution (pure DI water). The measurement results will be presented in Chapter 4.

Two different phenols were electrochemically reacted with chitosan on cantilevers in this project: catechol and dopamine. Catechol was used initially as a model analyte since its reaction with chitosan was better studied by Wu et al than that of dopamine. Next, the experimental conditions were adjusted to mechanically transduce dopamine oxidation with the chitosan-coated microcantilevers. Finally, ascorbic acid was electrochemically oxidized to show that it does not react with chitosan and does not cause a response of the chitosan-coated microcantilevers. Ascorbic acid was chosen due to its presence in common biological samples and its interference with dopamine electrochemical detection

[87]. The different reagents used for electrochemical oxidations are summarized in Table 3-12, and the experimental procedures are listed in Table 3-13.

Table 3-12. Reagents used for electrochemical oxidation and reaction with chitosan.

Reagent	Properties
Catechol solution (phenol)	0.2M catechol concentration dissolved in phosphate buffer (20mM, pH = 6.5)
Dopamine solution (phenol)	0.1M dopamine concentration dissolved in phosphate buffer (20mM, pH = 7.5)
Ascorbic acid solution	0.1M ascorbic acid concentration dissolved in phosphate buffer (20mM, pH = 7.5)

Table 3-13. Procedures for measuring the response of chitosan coated microcantilevers to electrochemical oxidation of various reagents.

Step	Procedure	Duration
1	Deposit chitosan on cantilever with micro probe (-0.7V to -0.9V applied)	varied, depending on chitosan thickness
2	Rinse with DI to remove excess chitosan solution	~10 sec, squirt bottle
3	Place in NaOH solution to neutralize chitosan film	5 min
4	Place in SSC buffer to stabilize pH	5 min
5	Rinse and place in DI to remove SSC buffer	10 min, rocking platform
6	(Optional) Rinse with IPA to minimize cantilever stiction upon drying	~10 sec, squirt bottle
7	(Optional) Blow-dry with nitrogen	~10 sec
8	Measure cantilever bending in air after drying or immersed in DI	-
9	Place in phenol or ascorbic acid solution and oxidize (1.8V applied for catechol solutions 0.9V for dopamine and ascorbic acid solutions)	30 sec for most experiments
10	Rinse and place in DI to remove excess solution	10 min, rocking platform
11	(Optional) Rinse with IPA to minimize cantilever stiction upon drying	~10 sec, squirt bottle
12	(Optional) Blow-dry with nitrogen	~10 sec
13	Measure cantilever bending in air after drying or immersed in DI	-

The voltages used for electrochemical oxidation and the solution pH were adjusted to prevent dissolving of chitosan during the reaction. Note that at the anode, the pH becomes lower than in the bulk solution; chitosan that is not crosslinked dissolves at pH

below 6.3. The conditions used for catechol oxidation (potential 1.8V, solution pH 6.5) did not dissolve the chitosan film appreciably. However, when the same conditions were applied to dopamine and ascorbic acid, the chitosan dissolved rapidly. This suggests that the crosslinking during catechol oxidation occurs fast and prevents the film from dissolving. The conditions for dopamine and ascorbic acid oxidation were adjusted to increase the pH at the anode. Experiments showed that oxidizing dopamine and ascorbic acid with 0.9V potential and solution pH 7.5 did not dissolve the chitosan measurably.

The typical oxidation time used for all three reagents was 30s. Measurements of the cantilever response showed that further oxidation did not cause further cantilever bending, suggesting that the chitosan crosslinking was completed after that time.

3.7 Conclusion

This chapter presented the microcantilever sensor fabrication and testing procedures. The fabrication process is based on two lithographic steps (metal patterning and nitride patterning) followed by KOH etching of the substrate to release the device. By aligning the features along the [100] direction of the silicon substrate, a cantilever airgap of approximately 20μm is achieved. Chitosan is electrodeposited on the cantilever using a micropositioning probe due to the small size of the electrical contact pads. After chitosan deposition, the sensor is used for the detection of DNA hybridization or dopamine electrochemical oxidation. The procedures for these experiments were described in this chapter, and the results will be presented in Chapter 4.

Chapter 4: Testing and Characterization

4.1 Introduction

The microcantilever sensors were first tested without the chitosan layer. The cantilevers' static bending, resonant frequencies, and Q factors were measured and the associated measurement errors were estimated. The same tests were also performed after chitosan deposition. Next, the sensors were used for the detection of DNA hybridization, as described in Chapter 3, in both static and dynamic modes. In static mode, measurements were performed in both air and in solution. In dynamic mode, measurements were taken only in air after drying the sample (due to the excessive damping of the liquid medium). Finally, the microcantilever sensors were used for the detection of phenol oxidation in the static mode as described in Chapter 3; measurements were performed both in air and in solution. In all studies reported in this chapter, the cantilevers are 100μm long unless otherwise noted.

The chapter begins with an in-depth description of the primary measurement instrument used in this work – the optical interferometer previously introduced in Chapter 2. Next, measurements of the cantilevers with and without chitosan are discussed. Testing results are presented for DNA hybridization detection in both static and dynamic modes. Finally, results from phenol detection with cantilevers in static mode are shown.

4.2 Detailed Description of Measurement System

4.2.1 Basic Principles of Interferometry

The optical interferometer (Veeco NT1100) used for measuring cantilever bending and resonant frequency was introduced in Chapter 2, but its operation is presented here in

more detail since it is relevant to the experimental results. Optical interferometry is a method to measure distances to a sample by using the phase shift of light reflected from its surface. Figure 4-1 shows a conceptual schematic of an optical interferometer. Light from the illumination source is split into two beams; one beam reflects from the sample (sample arm) and the other beam reflects from a reference mirror (reference arm). The two reflected beams are then added together; the optical power of the resultant beam is used to calculate the phase difference and optical path difference between the two beams as follows.

Equation 4-1 and Equation 4-2 are simplified expressions for the electric fields of the two interfering beams (here P is optical power, ω is optical frequency, θ is phase, and Z_0 is the characteristic impedance of free space). Equation 4-3 shows the power of the resultant beam, calculated from the total electric field. This power is a function of the phase difference between the interfering beams. Therefore, by measuring P, P_1 and P_2, the quantity $\theta_1 - \theta_2$ can be calculated. The optical path difference (OPD) between the reference arm and sample arm is found from the phase difference $\theta_1 - \theta_2$ by using Equation 4-4 (λ is the wavelength of light). From knowledge of the OPD and the length of the reference arm, the distance from the interferometer to the sample can be easily calculated.

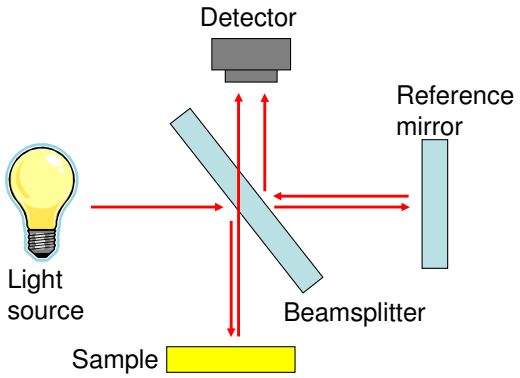

Figure 4-1. Conceptual schematic of optical interferometer.

Equation 4-1 $$E_1 = \sqrt{Z_0 P_1}\exp(j\omega t + \theta_1)$$

Equation 4-2 $$E_2 = \sqrt{Z_0 P_2}\exp(j\omega t + \theta_2)$$

Equation 4-3 $$P = \frac{(E_1 + E_2)(E_1^* + E_2^*)}{Z_0} = P_1 + P_2 + 2\sqrt{P_1 P_2}\cos(\theta_1 - \theta_2)$$

Equation 4-4 $$\theta_1 - \theta_2 = \frac{2\pi}{\lambda} OPD$$

In the Veeco NT1100, the interferometer is combined with imaging optics, a digital camera, and processing software. The simplified diagram of the instrument is shown in Figure 4-2. A continuous interference pattern is formed and projected onto the camera. The OPD is calculated for each pixel from the measured optical power as discussed above, resulting in a height map of the sample's surface.

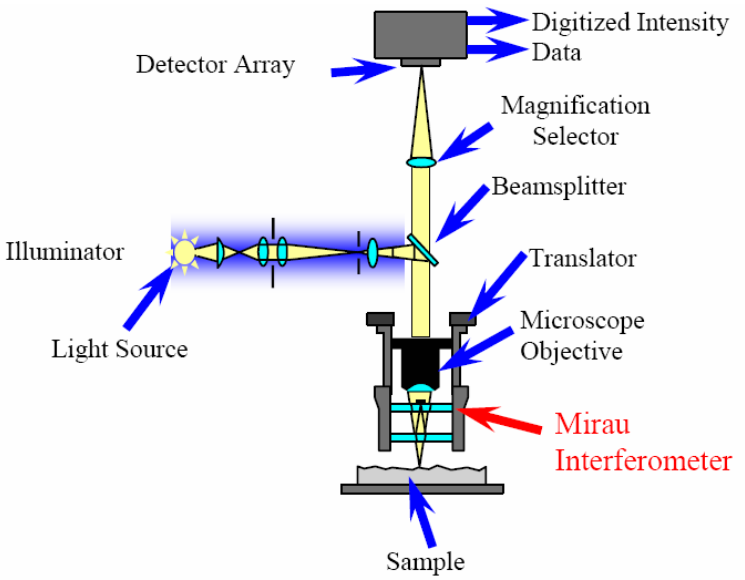

Figure 4-2. Diagram of Veeco Wyko optical interferometers. Obtained from [70].

4.2.2 PSI and VSI

The interferometric technique described above is known as Phase Shifting Interferometry (PSI). It is inherently limited in range since the measured optical power is a periodic function of phase shift (Equation 4-3). If the height difference between points on the sample corresponding to adjacent pixels exceeds $\lambda/4$, the calculated height difference could be off by any integer number of quarter wavelengths. Therefore, the maximum unambiguous step height that can be measured by PSI is $\lambda/4$ (approximately 150nm for the Veeco NT1100).

Another interferometric technique used by the Veeco NT1100 to overcome the limitations of PSI is Vertical Scanning Interferometry (VSI), also known as white light interferometry. While PSI is based on a narrowband light source to obtain a high-contrast interference pattern, VSI uses a broadband light source to intentionally degrade the interference pattern. To illustrate the effect of the broadband source, Figure 4-3 shows the combined optical intensity of two interfering beams for 4 different wavelengths of light.

This plot was made in MATLAB using Equation 4-3 and Equation 4-4. There is an interference maximum for all 4 wavelengths when the beams are in phase (0 OPD). However, away from 0 OPD, the interference maxima are in different positions for each wavelength. The total intensity of the four wavelengths should have a peak at 0 OPD, but it should decrease as OPD is increased due to non-overlapping peaks. This situation is illustrated in Figure 4-4, which was generated in MATLAB using the same equations as Figure 4-3 but for a broadband source (100nm range of closely spaced wavelengths). The plot shows the combined optical intensity of the two interfering broadband beams as a function of their OPD; as expected, the intensity has a maximum at 0 OPD.

In VSI mode, the Veeco NT1100 translates the interferometer vertically with respect to the sample. The translator position for 0 OPD at each pixel of the camera is found when the optical power at the pixel reaches maximum. This translator position information is used to create a height map of the sample. The advantage of VSI over PSI is that it has a large vertical measurement range, limited only by the translator (1mm for the Veeco NT 1100). However, VSI is inherently slower and less accurate than PSI due to the mechanical motion of the instrument involved.

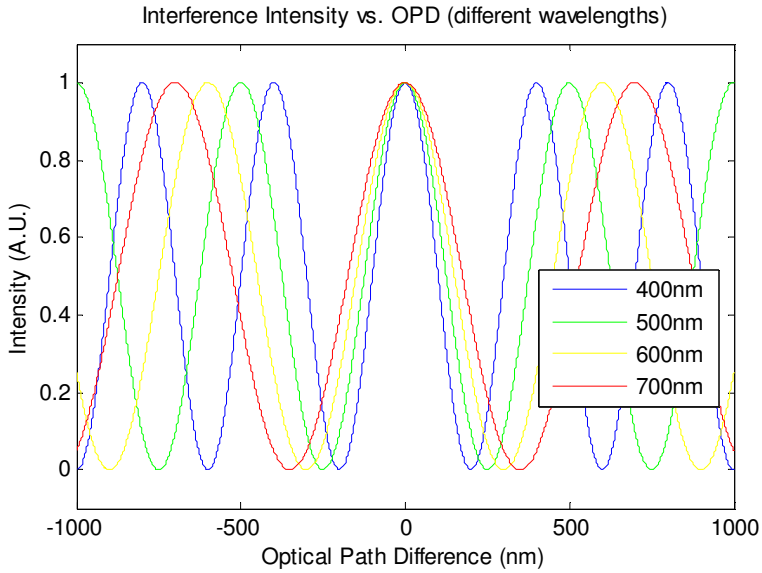

Figure 4-3. Interference intensity as a function of optical path difference for 4 different wavelengths. At 0 OPD, the maximum condition is satisfied for all wavelengths and their intensities add up. At increasing OPD, the interference patterns become different.

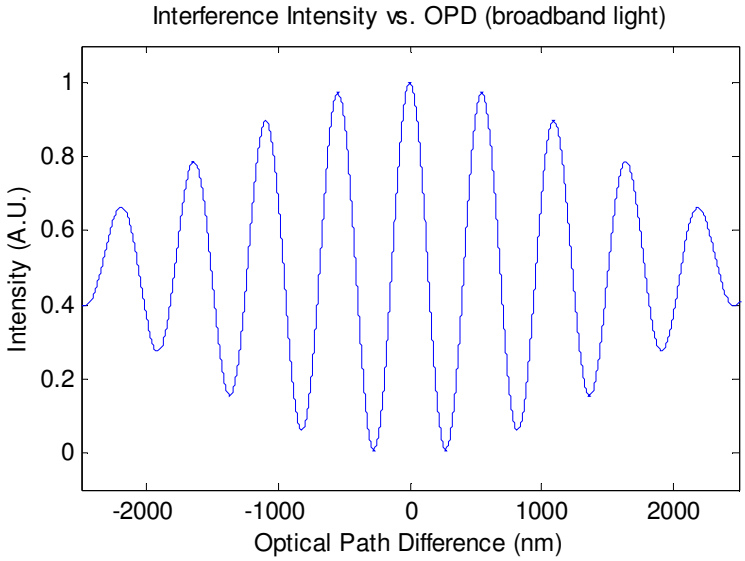

Figure 4-4. Interference intensity as a function of optical path difference for a broadband light source (100nm linewidth). The intensity is largest at 0 OPD and decreases elsewhere.

4.2.3 Custom Modification to Measure in Solution

As discussed in the introduction of this chapter, some of the static mode measurements are taken with the sample immersed in solution. Operation of the sensor in solution is preferable since the conditions are close to physiological and would preserve sensitive biological components that may be damaged by drying. In this project, the

cantilever was functionalized only with DNA, which is robust and can be readily dried. However, the ability to operate the sensor in solution allows functionalization with more sensitive biomolecules such as proteins.

The Veeco NT1100 cannot measure samples inside solution in its original configuration. The reason is that light passing through the solution experiences an increased phase shift (due to the refractive index of the solution) and therefore an increased OPD results. The imaging optics of the Veeco are set up for measurements in air; the focal distance of the objective coincides with the distance of 0 OPD of the interferometer when the sample is in air. When the sample is in solution, the 0 OPD distance shifts away from the focal distance. To form an image of the sample on the camera, the sample must be at the focal point; however, in that case the OPD is far from 0 and the interference pattern disappears, precluding any interferometric measurements.

In VSI, the interference pattern occurs only close to 0 OPD due to the use of a broadband light source (Figure 4-4). In PSI, the light source is filtered (3 nm linewidth), and the interference pattern persists up to approximately 240μm OPD (known as correlation length). However, the OPD needed for measurements through solution are much larger. For example, if the sample is immersed under only 1mm of water (refractive index 1.33), the OPD at the focal point becomes approximately 660μm and the interference pattern disappears. Note that covering the sample with only 1mm of water is difficult experimentally due to evaporation; several mm must be used in practice. Therefore, neither VSI nor PSI measurement can be taken through solutions with the original instrument configuration.

For this project, an illumination source with a narrower linewidth was added to the Veeco NT1100 to enable measurements in PSI mode through solutions (and other transparent materials). A single-mode laser diode was purchased from Mitsubishi (130mW optical power, 660nm wavelength) and its output was guided into the interferometer. The linewidth of the laser was not specified by the manufacturer and was not measured experimentally. However, it is narrow enough to produce a high-contrast interference pattern when measuring the sample through more than 5mm of water. The measured sample heights need to be adjusted to account for the refractive index of water (1.33μm) and for the different wavelength (660nm of the laser vs. 600nm of the built-in source). Note that the laser illumination does not allow VSI measurements through solution because broadband light is needed in that mode.

A major complication when using the laser illumination is caused by its spatial and temporal coherence. The laser light scatters off surface roughness on the sample and forms a "speckle pattern". This is essentially a standing interference pattern, which causes large local variations of the illumination intensity and precludes accurate PSI measurements. Figure 4-5A shows an image of a sample with the speckle pattern formed by coherent illumination. To eliminate this pattern, the laser light must be decohered.

A device commonly known as "spinning diffuser" was custom-made to decohere the laser. This device is based on a scratched plastic disk rotating at approximately 3000rpm, through which the laser light passes. Since the thickness of the disk varies at the scratches, the phase of the incident light is "scrambled" as the disk spins. This causes the speckle pattern to move around rapidly. The illumination intensity is thereby averaged over time, and it appears uniform to the camera of the interferometer. Figure 4-5B shows an image

of the same sample as Figure 4-5A but with the laser light decohered by the spinning diffuser. The speckle pattern is no longer present, and the PSI interference fringes used for height measurement are clearly visible. The spinning diffuser was assembled in a housing that contains the laser, electric motor, plastic disk, and fiber bundle. The bundle captures the light passing through the spinning disk and guides it into the illumination port of the NT1100. Figure 4-6 shows the assembly.

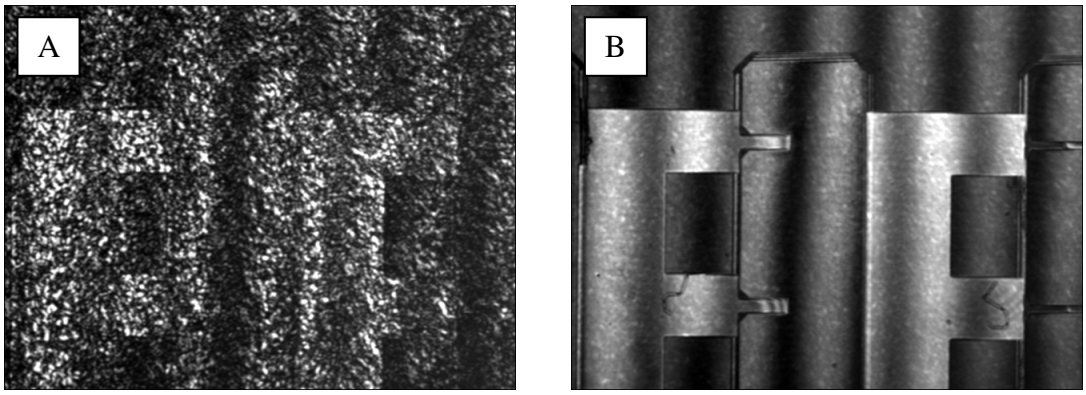

Figure 4-5. (A) Image from interferometer camera with coherent laser illumination (B) Image from interferometer camera with laser illumination decohered through spinning diffuser

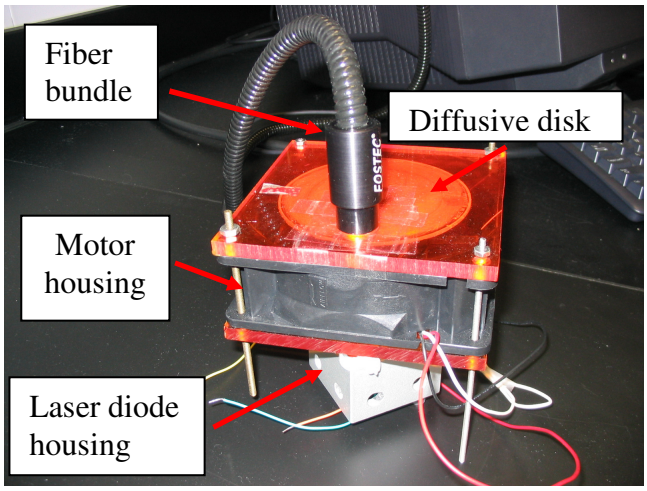

Figure 4-6. Photograph of custom-made assembly with laser diode and spinning diffuser to decohere the laser.

4.3 Measurement Procedures

4.3.1 Static Measurements of Cantilevers

All static mode cantilever measurements were taken by PSI. As explained in the previous section, PSI is more accurate than VSI but can be used only if the sample does not have a step height of more than 150nm. Note that if the feature has a gradual slope (as opposed to a step height) this limitation does not apply, and heights of a few μm can be measured. In addition, PSI is able to measure in solution with the laser illumination source.

For static mode operation, the vertical displacement of the cantilever tip is measured. The measurements were first performed for bare cantilevers in air (no chitosan). The random error was estimated by taking multiple scans of a single device. The standard deviation of the results was approximately 5nm. In theory, the Veeco NT1100 has sub-nanometer measurement precision, but environmental vibrations in the laboratory increase the random error to a few nm. The systematic error was not evaluated due to the use of differential measurements; systematic error is therefore subtracted and does not impact the results significantly.

The deposition of chitosan on the cantilever degrades the measurement precision considerably due to three different factors: humidity absorption, large cantilever bending, and optical phase shift at the surface. Chitosan absorbs moisture from the air, which changes the film stress and results in differential cantilever bending. The environmental humidity varies between experiments, causing uncertainty in the cantilever static mode measurement results (the effect on dynamic mode is discussed later). Cantilever bending variations of up to 100nm between measurements on different days were observed. This effect has the largest contribution to static mode error.

Another cause of error is the large out-of-plane bending of the cantilever after chitosan deposition. As discussed in Chapter 3, this effect is due to tensile residual stress in the chitosan film. The bending increases even more after DNA conjugation to the chitosan because the film is crosslinked by the glutaraldehyde. If the bending is very large (>10μm displacement at the tip), the cantilever position cannot be measured by the optical interferometer at all due to depth-of-focus limitations. For smaller amounts of bending, measurements are feasible but the error is significantly larger than for a perfectly straight cantilever. The reason for this is misalignments of the sample; a slightly different part of the cantilever is measured each time because the sample cannot be placed in exactly the same position within the interferometer's field of view. Due to the cantilever bending, lateral misalignment translates into a height measurement error. The greater the bending, the more sensitive the measurement is to lateral misalignment. In a typical experiment, a 100μm long cantilever with chitosan bends up by approximately 3μm at the tip. The lateral alignment tolerance of the interferometer stage is about 1μm, resulting in a height measurement error of approximately 30nm. This effect has the second largest contribution to measurement error after the humidity discussed above.

The third cause of measurement error is the optical effect of the chitosan film deposited on the cantilever. Note that for static mode, displacement measurements were taken directly on the chitosan-covered surface (dynamic measurements were taken on a chitosan-free rectangle at the cantilever tip described in Chapter 2). Chitosan is transparent and therefore increases the phase shift of light reflected from the cantilever. An increased OPD is measured by the interferometer, and it is interpreted as an increased sample height. This results in an offset error in the cantilever displacement measurements

which depends on the chitosan thickness. This error would not affect the sensor operation if the chitosan thickness were constant between experiments because differential measurements of cantilever bending are taken. The offset error would be the same before and after the detection event, and it would be cancelled. In practice, the chitosan thickness varies spatially, and slightly different parts of the cantilever are measured each time due to sample misalignment within the field of view. Therefore, in effect, the chitosan thickness varies between experiments and some random measurement error is introduced. This error, however, was observed to be small compared to the error caused by cantilever out-of-plane bending which was described above.

After testing in air with and without chitosan, the cantilever measurements in solution were evaluated. The cantilever chip was placed in a small container such that it fits under the Veeco NT1100 objectives (Figure 4-7), and it was immersed under several mm of DI (deionized water). Cantilever bending measurements through the DI were taken with the custom laser illumination source previously described.

Measurement of cantilevers with chitosan in solution is typically more repeatable than measurement in air. It is inherently immune from environmental humidity variations, and the only major source of error is lateral misalignment of the sample within the field of view. This error leads to approximately 30nm standard deviation of measurements. One complication for in-solution experiments is that they are more sensitive to environmental vibrations. Small waves are occasionally formed in the container and take several seconds to settle. These perturbations cause measurements to have excessive error (>100nm) or even fail completely (due to insufficient interference pattern contrast). For this reason, multiple measurements are taken in solution, and the “outliers” are eliminated.

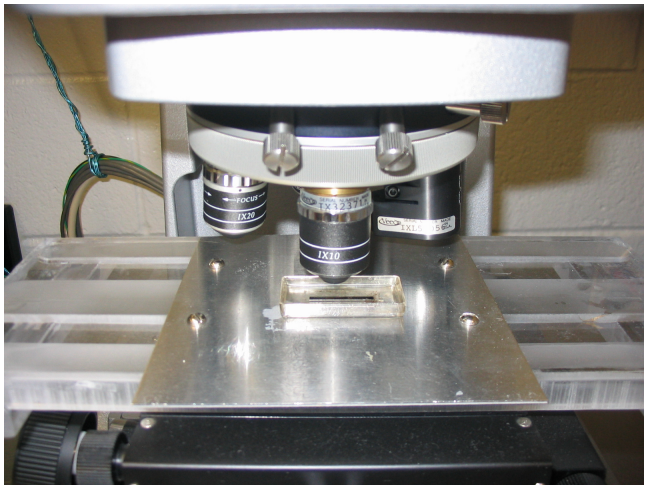

Figure 4-7. Cantilever chip immersed in container for in-solution bending measurements in static mode.

4.3.2 Dynamic Measurements of Cantilevers

All dynamic mode cantilever measurements were performed in air after drying the sample. Viscous damping in liquid would dramatically reduce the Q factor and therefore the resonant frequency measurement accuracy. The Veeco NT1100 has a dynamic measurement module called "DMEMS", which is based on the principle of stroboscopic photography. Since the cantilever oscillates fast (60kHz), its displacement cannot be measured real time (the built-in camera captures only 30 frames/sec). For this reason, the sample is illuminated with a strobe light instead of a continuous source. The strobe has a narrow duty cycle (typically 2%), and it has the same frequency as the actuation signal. When the strobe is on, the sample is always within the same position in a cycle, i.e. it appears stationary to the camera. An interferometric measurement (either PSI or VSI) is taken as if the sample were static.

Figure 4-8 illustrates the timing of the DMEMS strobe and actuation signals and the displacement of an idealized cantilever. Note that the actuation voltage applied is always positive. The reason for this is that electrostatic actuation is attractive regardless of

polarity (as discussed in Chapter 2); if the actuation signal is allowed to go negative, a frequency doubling of the cantilever displacement would be observed. In this schematic, the displacement of the sample is shown to be in phase with the actuation signal for simplicity. However, there is actually a phase shift between the two that depends on the frequency, as will be shown later in Figure 4-11.

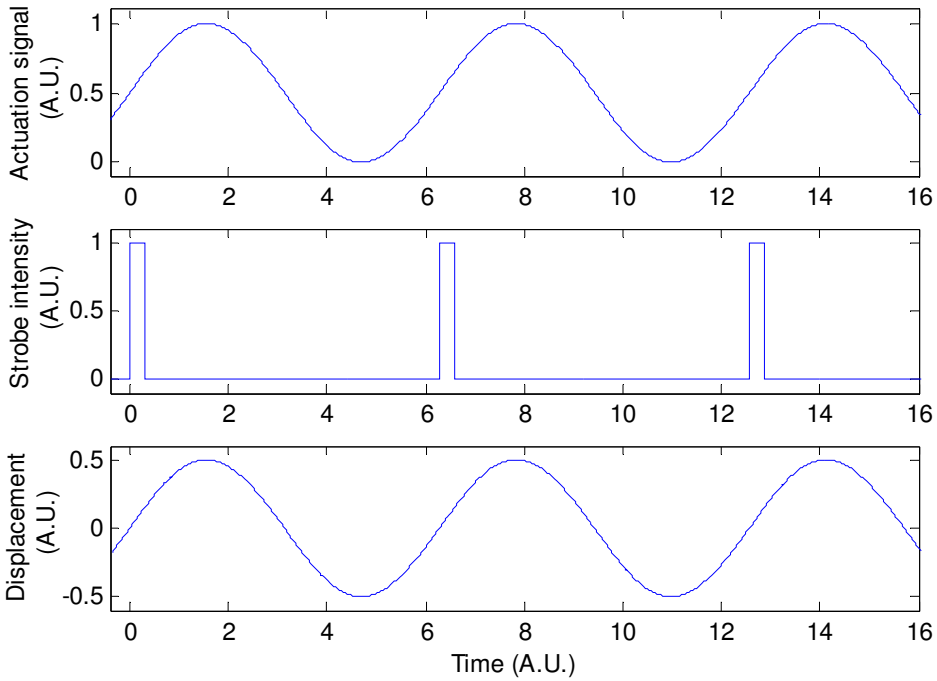

Figure 4-8. Timing diagram for excitation signal, strobe, and cantilever displacement for dynamic mode measurements (idealized system). The displacement signal is shown to be in phase with the actuation signal. This occurs if the actuation frequency is much smaller than the resonant frequency.

Although the Veeco DMEMS can work with both PSI and VSI interferometric modes, the VSI was selected for this project. The reason for this choice is the broadband emission of the illumination strobe. This strobe is implemented by a light-emitting diode (LED) and cannot be filtered with the 3nm PSI filter because of insufficient intensity. The broadband nature of the LED significantly degrades the quality of PSI measurements, especially with chitosan films on the cantilever surface that reduce the interference

contrast. The laser illumination source used for in-solution PSI is narrow, but it could not serve as a strobe because of its insufficient intensity (note that more than 90% of laser power is lost in the spinning diffuser). The VSI measurements with the LED strobe were more precise than the PSI and were therefore chosen for this project. One complication is that VSI cannot be performed with chitosan on the surface. Recall that VSI finds the translator position for 0 OPD by the peak in reflected light intensity (Figure 4-4). When chitosan film is present on the surface, this peak is both degraded and shifted, resulting in large measurement errors. For this reason, the dynamic mode cantilevers were designed with a chitosan-free rectangle at the tip (Chapter 2) for VSI measurements.

Figure 4-8 shows how the cantilever displacement is measured at a single actuation frequency and strobe phase. To obtain the position of the sample at different times within the actuation cycle, the phase of the strobe is changed (phase sweep) while keeping the frequency constant. An example phase sweep for a cantilever is shown in Figure 4-9. To find the position of the sample at different frequencies, the actuation frequency is changed (frequency sweep), while keeping the strobe phase constant. Figure 4-10 shows an example frequency sweep strobed at phase 0^{o} relative to the actuation signal.

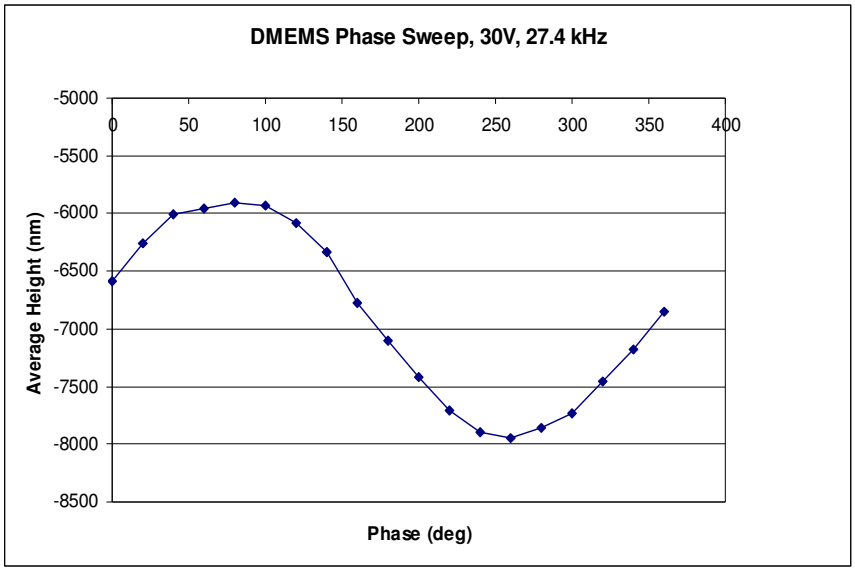

Figure 4-9. Measured displacement of cantilever at different strobe phases relative to the actuation signal.

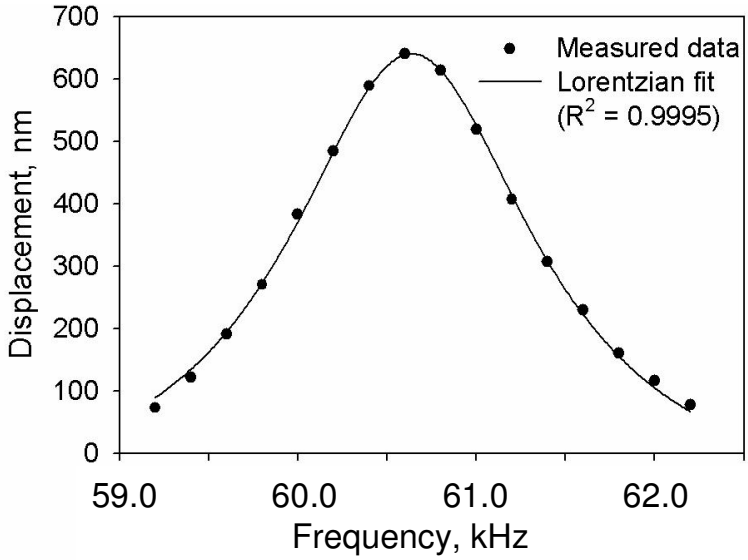

Figure 4-10. Measured cantilever displacement for different actuation frequencies. The strobe occurs at phase 0 relative to the actuation signal.

To find the resonant frequency of a cantilever, it is necessary to measure the amplitude of the cantilever over a range of frequencies. However, to measure the amplitude, the displacement at different phases has to be measured to find the maximum displacement. This requires a nested phase sweep within a frequency sweep, which is

very time-consuming and impractical. For example, to scan 20 frequencies at 20 phases each, 400 displacement measurements are needed. Each measurement takes the instrument about 5s, resulting in roughly 30min for measuring the resonant frequency of a single cantilever. In addition, multiple resonant frequency measurements need to be taken to evaluate the repeatability, making this approach impractical.

The cantilever resonant frequency can also be estimated by measuring only the displacement at 0^o phase for each frequency. As discussed previously in Chapter 2, the cantilever is essentially a mass-spring-dashpot system; consider the idealized frequency response of such a system shown in Figure 4-11. The phase of the cantilever displacement decreases with frequency. At low frequencies, the phase shift is 0^o, at resonance it is -90^o, and at high frequencies it becomes -180^o. The solid curve in the top plot shows the cantilever amplitude response, and the dashed curve is the cantilever displacement at 0^o phase relative to the actuation signal. The peaks of the two curves occur at approximately the same frequency. Therefore, frequency sweeps at 0^o phase can be used to find the resonant frequency instead of the time-consuming nested frequency and phase sweeps. As an added benefit, the peak of the dashed curve is actually sharper, and its frequency can be measured more accurately than that of the sold curve.

Strictly speaking, the resonant frequency measured using this method (peak in 0^o phase displacement) is slightly larger than the actual resonant frequency (peak in amplitude). The difference depends on the system's resonant frequency, Q factor, and any parasitic capacitances in the actuation circuit that increase the phase shift. However, for this project the exact resonant frequency is not needed; the change of cantilever resonant frequency after biological detection events is the quantity of interest. This

quantity is essentially the same whether we measure the resonant frequency as a peak in 0^o phase displacement or as a peak in amplitude.

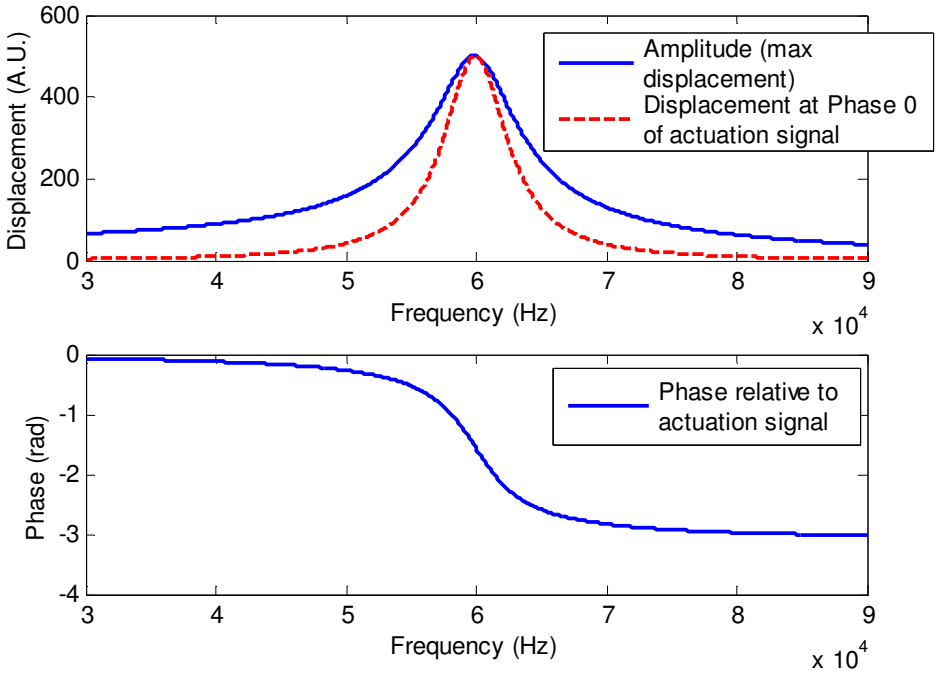

Figure 4-11. Amplitude and phase frequency response of an idealized mass-spring-dashpot system.

The measured displacement frequency response is curve-fitted using a Lorentzian function in Sigma Plot software to extract the resonant frequency (Figure 4-10). The coefficient of determination is typically very high ($R^2 > 0.999$), confirming that the cantilever behaves approximately as a linear mass-spring-dashpot system. The measured resonant frequency of cantilevers without chitosan is approximately 58 kHz, which is within 4% the calculated value of 60 kHz in Chapter 2. This close agreement suggests that the material properties, cantilever dimensions and assumptions used in the calculation are approximately valid. The measured resonant frequency of cantilevers with chitosan is typically several kHz above that of the uncoated cantilevers, depending on the chitosan thickness and coverage. To estimate the cantilever Q factor, the measured

displacement amplitude at resonance is divided by the displacement at DC (Equation 2-24). The typical measured Q factor is 20, and the addition of chitosan has no measurable effect on the cantilever Q factor.

4.3.3 Dynamic Measurement Error

The experimental error in cantilever resonant frequency is estimated by taking multiple measurements and finding the standard deviation of the results. For uncoated cantilevers (no chitosan), the standard deviation is approximately 5Hz. This error is mainly caused by ambient vibrations in the laboratory, which introduce displacement measurement error and corrupt the shape of the frequency response peak. For coated cantilevers, the measurement uncertainty is greatly increased due to humidity absorption of the chitosan film. The air humidity determines the moisture content of the film, which in turn influences the total cantilever mass, spring constant, and resonant frequency. Humidity varies between experiments, increasing the random error in resonant frequency measurements of coated cantilevers. The standard deviation of multiple measurements over different days is more than of 100Hz. Figure 4-12 illustrates the considerable resonant frequency fluctuations of a cantilever with chitosan; for comparison, Figure 4-13 shows the resonant frequency variability of a cantilever without chitosan.

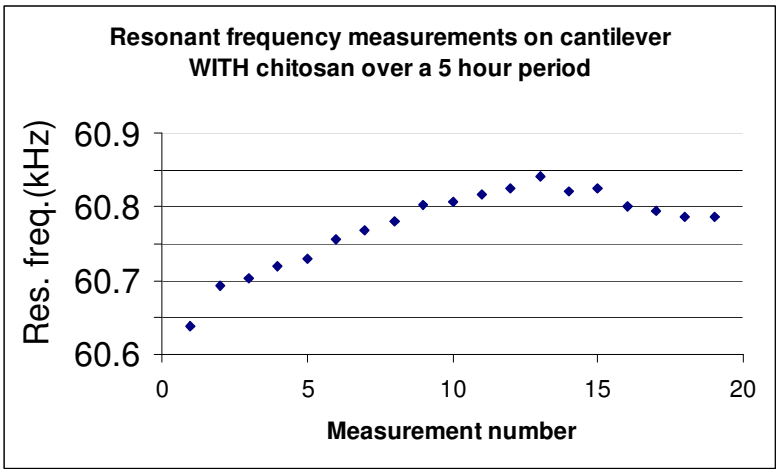

Figure 4-12. Resonant frequency variability of cantilever with chitosan due to humidity.

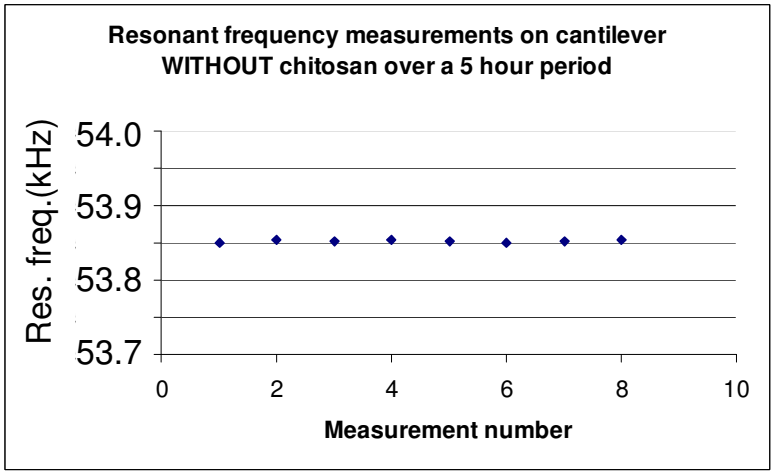

Figure 4-13. Resonant frequency variability of cantilever without chitosan. The error is caused mainly by ambient vibrations and the effect of humidity is immeasurable.

In this project, the resonant frequency shifts caused by DNA hybridization are large (over 1kHz) and the humidity-induced measurement error is acceptable. However, to improve the detection limit, this error should be minimized. Two different methods were explored to combat humidity variations: dehydration of the sample with nitrogen and the use of a reference cantilever. Neither of these methods was sufficiently developed to fully eliminate humidity variation, but they are shown here as a proof of concept.

The idea behind the dehydration method is to flow high-purity nitrogen gas over the cantilever die until the chitosan film is dehydrated before each resonant frequency measurement. The resulting humidity content of the film should be negligible, and the measurements should be repeatable. The setup for this experiment is shown in Figure 4-14. In practice, however, the chitosan quickly absorbs humidity when the nitrogen is stopped. By the time a resonant frequency measurement is performed (it takes at least 1min), the film becomes partially hydrated and the measured value changes. One way to overcome this effect is to perform the measurement while the nitrogen is flowing instead of after.

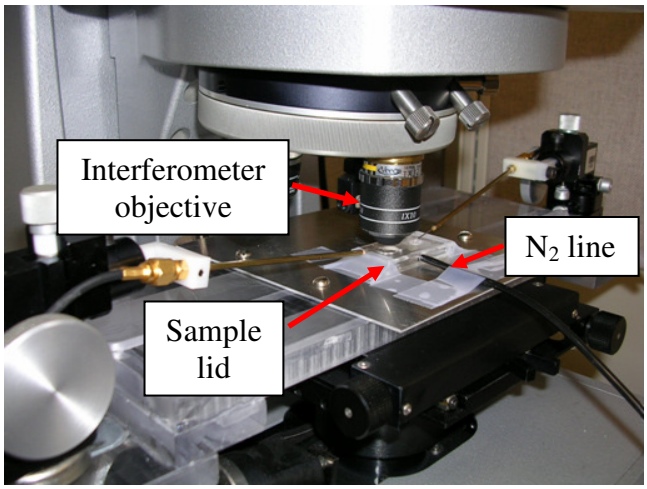

Figure 4-14. Setup for nitrogen dehydration. Sample is covered with a lid, and high-purity nitrogen from a cylinder is flown continuously under the lid. The lid has holes for optical displacement measurement and electrical connections.

Figure 4-15 shows that the resonant frequency of a cantilever measured while it is being dehydrated. The value follows an "exponential rise to max" behavior; it increases rapidly at first and then asymptotically approaches equilibrium. This equilibrium frequency in practice depends on the nitrogen flow rate because it is affected by air pressure and cantilever damping. In our setup, the nitrogen flow rate could not be

precisely controlled and the equilibrium frequency varied considerably between experiments. However, with an improved nitrogen flow setup, the equilibrium frequency should be as repeatable as measurements of uncoated cantilevers.

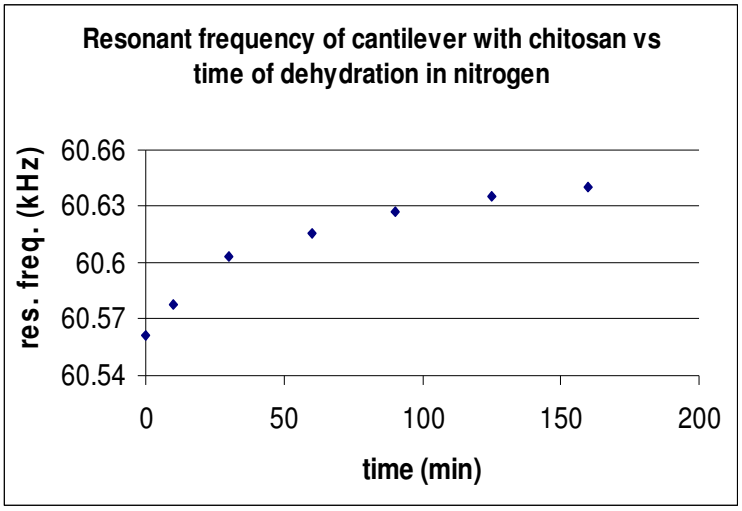

Figure 4-15. Measured resonant frequency of cantilever with chitosan being dehydrated in nitrogen. The resonant frequency asymptotically approaches an equilibrium value.

The second method explored for reducing the humidity error in resonant frequency measurements is based on a reference cantilever. The idea behind this approach is to use one cantilever for detecting DNA hybridization plus air humidity and another for detecting the air humidity only (reference). The resonant frequency of the reference can be subtracted from the resonant frequency of the DNA cantilever, canceling the effect of humidity variations on the frequency shift. This compensation approach requires that both cantilevers have the same dependence of the resonant frequency on humidity, and that both are exposed to the same humidity during measurement.

In practice, each cantilever has a slightly different chitosan coverage and thickness, and the electrodeposition is not perfectly reproducible (as discussed in Chapter 3). As a consequence, the two cantilevers have a different dependence of resonant frequency on humidity. However, if the humidity dependences of the cantilevers can be experimentally

correlated to each other, the compensation could still be performed. Figure 4-16 shows the measured resonant frequency for a pair of cantilevers with chitosan; each datapoint is obtained at different air humidity (at a different time of day). The linear regression indicates that the humidity dependences of the two cantilevers correlate well, and that Cantilever 1 is approximately 0.6 times as sensitive to humidity as Cantilever 2. With this "calibration curve" in mind, one of the cantilevers could be used to detected biological events and the other as a reference to track humidity. This method was not used for the actual detection of DNA here because of the excessive time required to generate an adequate calibration curve for each pair of cantilevers (several days). Nevertheless, Figure 4-16 demonstrates that the concept is feasible.

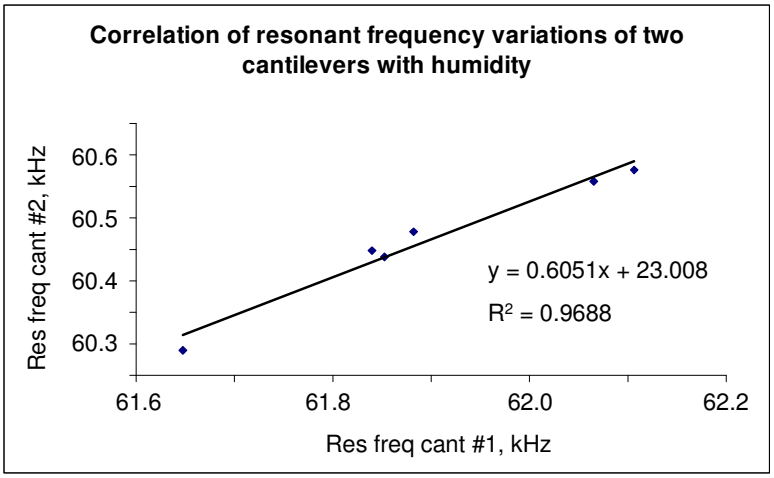

Figure 4-16. Measured resonant frequencies of two different cantilevers with chitosan. Each data point is obtained at different air humidity. The solid line is a linear regression.

With the Veeco NT1100, each resonant frequency measurement takes several minutes to set up and at least one minute to execute. Meanwhile, the humidity drifts and the two cantilevers are not subjected to exactly the same conditions during measurement. This discrepancy may be the reason why the points in Figure 4-16 do not lie exactly on the regression line. A more real-time measurement setup is required for the reference

cantilever technique to be accurate; this would also speed up the generation of the calibration curve and facilitate the experiments. Such a setup was demonstrated by Gfeller et al [32] but was not pursued in this project.

In summary, the measurements of chitosan-coated cantilevers in dynamic mode suffer from considerable variations caused by air humidity. The DNA hybridization experiments in this project result in relatively large resonant frequency shifts and the humidity variations can be tolerated. However, to improve the detection limit, these variations must be addressed. Two different methods were explored here as a proof of concept but were not employed in the actual DNA hybridization experiments due to the large signals obtained.

4.4 DNA Hybridization Measurements

DNA hybridization detection with chitosan coated-cantilevers was performed in dynamic mode in air, static mode in solution, and static mode in air. The reagents, oligonucleotides, and procedures for the DNA experiments were previously described in detail in Chapter 3. The following sections summarize the experimental results. The hybridization in each cantilever detection experiment was also verified visually by fluorescence microscopy (recall that the DNA sandwich probe is labeled with Fluorescein). However, satisfactory fluorescent micrographs could not be obtained in most cases and are not presented here. The camera in use required long exposure times at high magnification, which caused the samples to bleach before an adequate fluorescent image could be obtained.

4.4.1 Dynamic Mode in Air

For dynamic analysis, DNA hybridization is detected as a change in the cantilever's resonant frequency when measurements are made in air (viscous damping dramatically reduces resonance Q factor in liquid). Typically, the resonant frequency shift is attributed to the change in the cantilever mass upon hybridization. For these experiments, a 100nm thick film of chitosan is electrodeposited on a cantilever and functionalized with either the *dnaK* probe (complementary) or the *6xHis* probe (noncomplementary). The sample is immersed in the *dnaK* target (Table 3-7) for hybridization and later is denatured in Urea solution. Cantilever resonant frequency measurements are taken at each step after drying the sample with nitrogen as described in Tables 3-9, 3-10, and 3-11.

Figure 4-17A shows the frequency response of a cantilever functionalized with the complementary probe-target pair. Before hybridization, the resonant frequency is approximately 61.8 kHz. After hybridization, the resonant frequency is reduced to approximately 59.4 kHz. Finally, after denaturation, the cantilever resonant frequency returns to the pre-hybridized value although this return is incomplete (61.1 kHz). Presumably the observed difference in resonant frequency between the pre-hybridization and post-denaturation measurements is due either to incomplete denaturation or air humidity variations.

Figure 4-17B shows the frequency response of a control cantilever with the noncomplementary probe-target pair. The initial resonant frequency is 61.6 kHz. Upon hybridization, the resonant frequency becomes 61.0 kHz and upon denaturation 60.7 kHz. The differential changes in resonant frequency are small compared to the matching DNA case and are caused mainly by air humidity variations. This explanation is consistent with Figure 4-17A, in which the difference between pre-hybridization and post-denaturation

measurements is 0.7 kHz (ideally, it should be 0). In Figure 4-17B, the corresponding difference is very similar (0.9 kHz); note that the complementary and noncomplementary measurements are taken within a 10 min period of each other are subject to similar environmental humidity. These results suggest that using a reference cantilever in parallel with the measurements to track instantaneous humidity variations could considerably improve the detection limit [32].

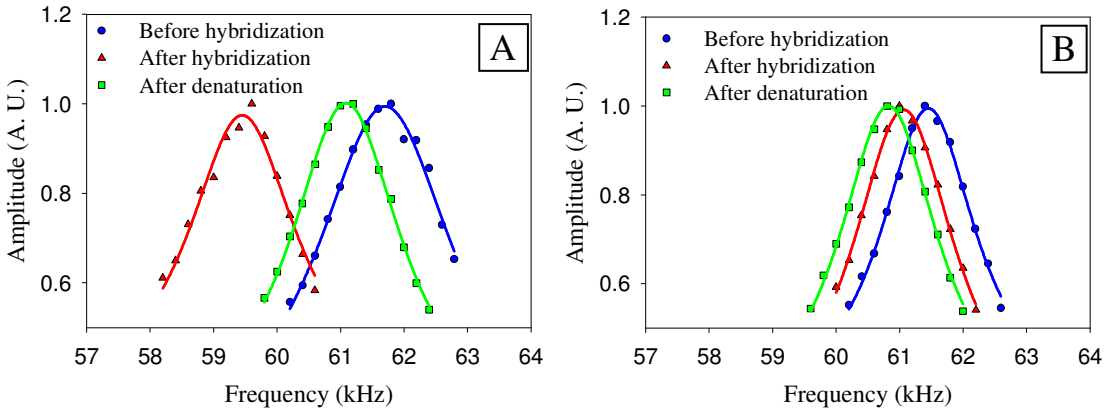

Figure 4-17. (A) Frequency response of cantilever with chitosan and *complementary* probe DNA after hybridization and denaturation (measured in air). Points are raw data and curves are fitted Lorentzian functions. Hybridization reduces the resonant frequency by 2.5kHz, and denaturation reverses the shift. (B) Frequency response of cantilever with chitosan and *noncomplementary* probe DNA after hybridization and denaturation (measured in air). Frequency shifts are <500Hz and are caused by humidity variation between measurements.

Figure 4-18 shows dynamic mode measurement results of multiple cantilevers with either complementary or noncomplementary probe-target DNA pairs. Here, only the resonant frequencies are given instead of the frequency response curves (shown in Figure 4-17). In each case, the hybridization causes a considerable resonant frequency decrease for the complementary DNA; the frequency after denaturation returns close to its initial value (Figure 4-18A). The resonant frequency shifts for the noncomplementary DNA (Figure 4-18B) are smaller by comparison and are only downward. These shifts are

caused mainly by air humidity variations, as previously discussed, and they can be potentially eliminated with the use of reference cantilever measurements. Note that each cantilever in Figure 4-18 has a different initial resonant frequency. The reason for this discrepancy is the slightly different thickness of chitosan on each cantilever.

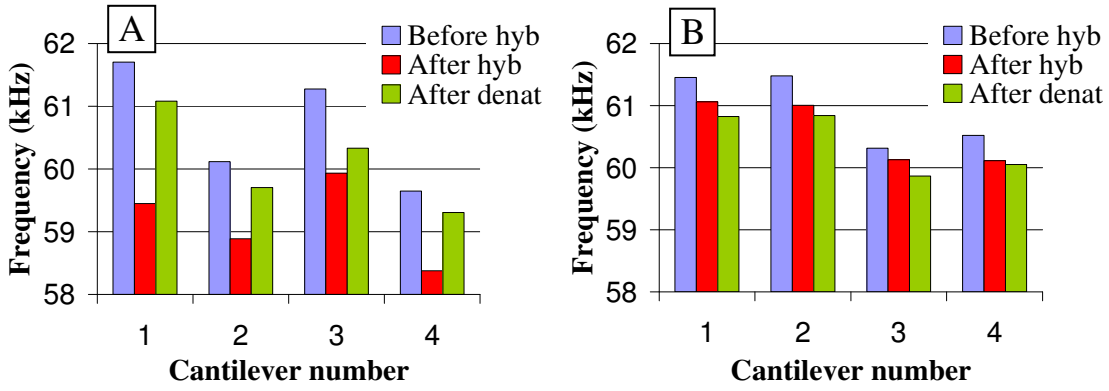

Figure 4-18. Resonant frequency of multiple cantilevers in response to hybridization and denaturation for (A) complementary DNA (B) noncomplementary DNA. All measurements are performed in air after drying the sample.

The DNA hybridization can affect the cantilever resonant frequency by three different mechanisms: change in the spring constant, increase in the mass, or change in the damping. Additional characterization is needed to determine the contributions of each effect to the observed resonant frequency shifts. In studies with DNA immobilized on resonators with SAMs (Self Assembled Monolayers), it is typically assumed that the frequency shift is caused by mass changes [37]. If we assume that the mass increase effect dominates and the DNA is distributed uniformly on the cantilever, the calculated target DNA mass is approximately 16 $\mu g/cm^2$ based on a conservative frequency shift of 1 kHz. This is equivalent to 2.8×10^{14} target molecules/cm^2, two orders of magnitude over what has been reported in studies using self assembled monolayers [24, 28]. This estimate is not rigorous; it has not been verified that the resonant frequency shift is

caused by mass change alone and that the target DNA is uniformly distributed on the cantilever. The important observation, however, is that the frequency shift caused by hybridization of chitosan-bound DNA far exceeds that caused by self-assembled DNA. The nature of the mechanism that causes the shift is not significant for this application.

4.4.2 Static Mode in Solution

In the static mode of operation, DNA hybridization is detected as differential cantilever bending caused by increased surface stress. While in dynamic mode the measurements have to be performed in air after drying the sample, in static mode they can be performed in solution. The main advantage of in-solution measurements is that they are compatible with physiological conditions; therefore, they can be extended to sensitive probe/target biomolecules that would be damaged by drying. The liquid used for measurements here is pure deionized water (DI) and serves merely as a proof of concept. However, the liquid could be any solution with low optical loss and known refractive index.

A 200nm thick film of chitosan is electrodeposited on the cantilevers and functionalized with either the *dnaK* probe (complementary) or the *6xHis* probe (noncomplementary). Note that the chitosan thickness here is larger than for dynamic measurements in air (~100nm). When measurements are performed in solution, the chitosan film is hydrated and has less residual stress (and causes less initial cantilever bending). This allows thicker chitosan films to be used in solution. The functionalized sample is exposed to the *dnaK* target solution (Table 3-7) for hybridization and later is denatured in Urea solution. Cantilever bending measurements are taken at each step with the sample immersed in DI as described in Tables 3-9, 3-10, and 3-11. The modified

Veeco NT1100 with laser illumination source is used to enable measurements through the DI.

Figure 4-19A shows the bending response of a cantilever functionalized with the complementary probe-target DNA pair. The cantilever undergoes some initial bending before DNA hybridization because of the residual stress in the chitosan film. After hybridization, the upward bending of the cantilever increases by approximately 500nm at the tip. This differential bending can be estimated from Equation 2-17 to be caused by an increase in surface stress of 1.6 N/m (tensile). After denaturation, the cantilever bending returns close to its original level. The small difference between the pre-hybridization and post-denaturation values is caused by a combination of measurement error and incomplete denaturation. Together, the results in Figure 4-19A indicate that the observed 500nm differential bending is due to specific interactions forming the hybridized DNA duplex.

Figure 4-19B shows the bending response of a control cantilever functionalized with the noncomplementary probe-target DNA pair. As in Figure 4-19A, the cantilever has some initial bending due to residual stress of the chitosan film. However, here the hybridization and denaturation cause little change in cantilever bending (<30nm). This differential bending should ideally be 0 due to the mismatching DNA sequences; the small variations observed in Figure 4-19B are caused by measurement error and possibly to some nonspecific target DNA binding. The specificity of hybridization could be improved by optimizing the rinsing and buffering conditions. Together, the results in Figure 4-19A and Figure 4-19B indicate that biological recondition between probe and target DNA occurs and is successfully transduced by the chitosan-coated cantilever.

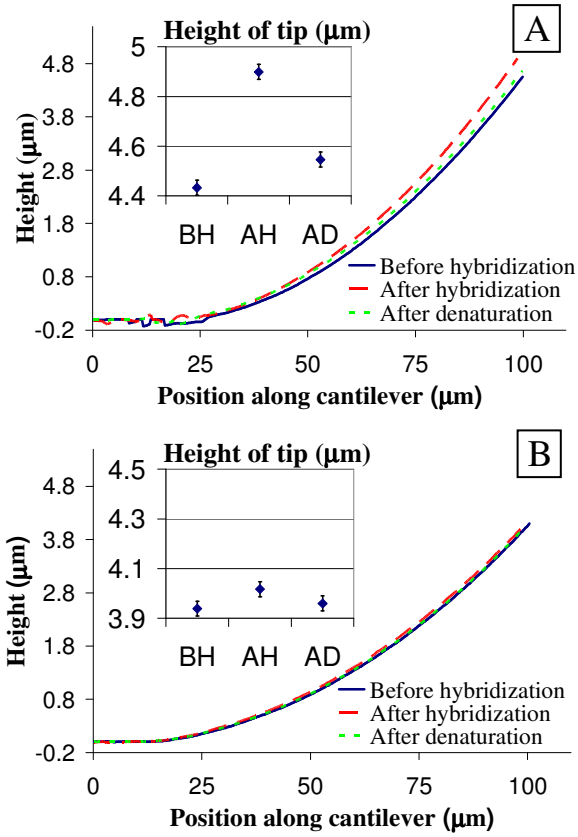

Figure 4-19. (A) Vertical profile of cantilever with chitosan and *complementary* probe DNA in response to hybridization and denaturation (measured in solution). The hybridization causes upward differential bending of ~500nm at the tip. The bending is reversed by denaturation. (B) Response of cantilever with chitosan and *noncomplementary* probe DNA to hybridization and denaturation (measured in solution). The differential bending is <30nm.

Figure 4-20 summarizes the static mode measurement results of multiple cantilevers with either complementary or noncomplementary probe-target DNA pairs. This figure shows only the displacement of the cantilever tip instead of a profile of the whole cantilever. The differential bending in response to hybridization and denaturation in each case is very similar to that in Figure 4-19, confirming the repeatability of the experiments. Note that the initial tip displacement ("before hybridization") of each cantilever in Figure 4-20 is different. The reason for this discrepancy is that the chitosan thickness in each case varies slightly, causing a different initial bending of each cantilever. However, the

differential displacement of the cantilevers upon hybridization and denaturation is repeatable.

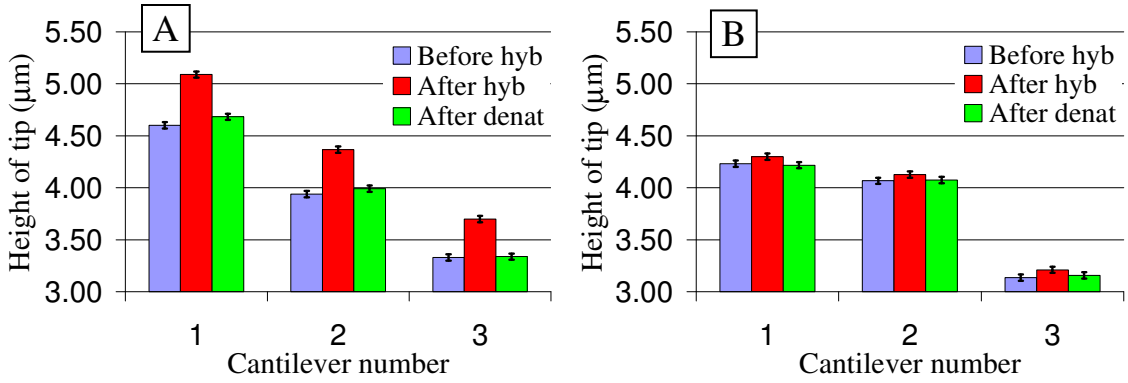

Figure 4-20. (A) Bending of multiple cantilevers with chitosan and *complementary* DNA in response to hybridization and denaturation (measured in solution) (B) Bending of multiple cantilevers with chitosan and *noncomplementary* DNA in response to hybridization and denaturation (measured in solution).

The mechanism of surface stress generation by DNA hybridization is generally not well understood. It has been explained by electrostatic and steric interactions between the DNA molecules as well as maximization of their configurational entropy [26, 27], but comprehensive models are lacking. The generated surface stress in this study significantly exceeds values reported in literature for DNA with similar concentration immobilized by self- assembled monolayer (SAM) techniques instead of on chitosan. We measured stresses of approximately 1.6 N/m, while others report 0.02 N/m for SAMs immobilized DNA [28]. The reason for this significant increase is presumably the large effective surface area of chitosan due to its 3D hydrogel structure and its high density of amine groups. Thus, we believe that micromechanical sensors can significantly benefit in sensitivity by the use of chitosan to immobilize the probe molecules.

4.4.3 Static Mode in Air

Static-mode detection of DNA hybridization was also performed with cantilever bending measurements in air (after drying the sample). This method cannot be applied to sensitive probe/target biomolecules that would be damaged by drying, and it is also influenced by air humidity variations. Nevertheless, it was explored initially in this project due to its simplicity compared to the in-solution measurement approach. It does not require the laser modification to the Veeco NT1100 that is needed to measure through liquid.

A 100nm chitosan film is deposited on a cantilever and is functionalized with either the *dnaK* probe (complementary) or the *6xHis* probe (noncomplementary). The sample is exposed to the *dnaK* target solution (Table 3-7) for hybridization and later is denatured in Urea solution. Cantilever bending measurements are taken at each step after drying the sample as described in Tables 3-9, 3-10, and 3-11. For these measurements, the Veeco NT1100 is used in PSI mode with its original illumination source. The results are heavily influenced by air humidity variations, which modulate the stress in the chitosan film and the cantilever bending. The humidity-induced error is estimated to be on the order of 100nm displacement at the cantilever tip (based on the standard deviation of multiple measurements).

Figure 4-21A shows the bending response of a cantilever functionalized with the complementary probe-target DNA pair. The hybridization generates a tensile stress, bending the cantilever up by approximately 1μm. The estimated surface stress from this bending using Equation 2-17 is 4 N/m. After denaturation, the cantilever returns almost to its initial state. The reason for the discrepancy between the pre-hybridization and post-denaturation profiles is measurement error (due to humidity variation) and incomplete

denaturation. Figure 4-21B shows the response of a cantilever with the noncomplementary probe-target DNA pair. The differential bending after "hybridization" in this case is approximately 200nm, while ideally it should be 0. This variation is caused by humidity-induced measurement error and possibly by some nonspecific binding of target DNA.

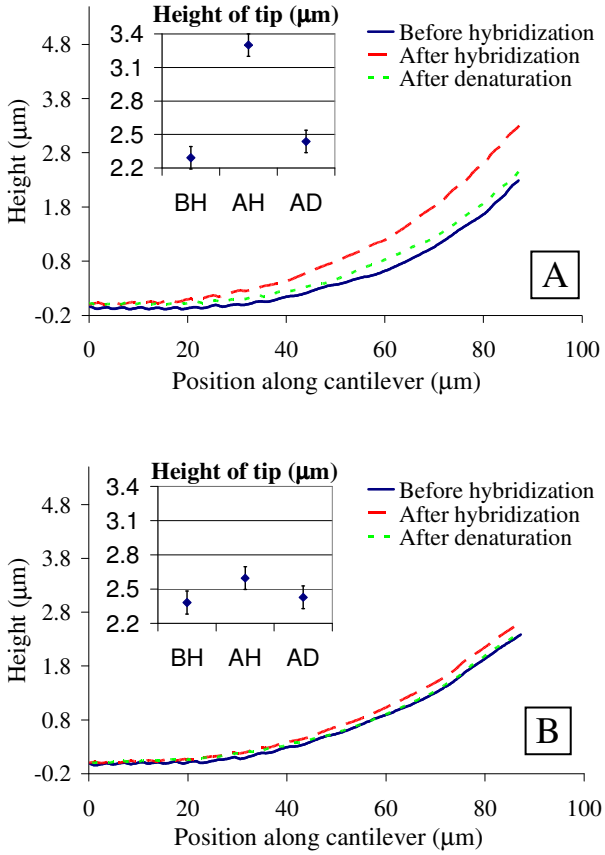

Figure 4-21. (A) Bending profile of cantilever with chitosan and *complementary* probe DNA in response to hybridization and denaturation (measured in air). The hybridization causes upward differential bending of ~1µm at the tip. The bending is almost reversed by denaturation. (B) Response of cantilever with chitosan and *noncomplementary* probe DNA to hybridization and denaturation (measured in air). The differential bending is ~200nm.

In summary, the static experiments in air result in more hybridization-induced surface stress than similar measurements in solution (4 N/m compared to 1.6 N/m). The reason for this may be that the electrostatic screening of water reduces the interactions between

probe and target biomolecules. However, measurements in air suffer from larger experimental error. As a result, the static mode operation of chitosan-coated cantilevers in solution is preferable to that in air.

4.5 Phenol Oxidation Measurements

Mechano-detection of phenol electrochemical oxidation with chitosan-coated cantilevers was performed in static mode in both air and solution. As discussed in the introduction, two different phenols were explored: catechol and dopamine. Dopamine was the analyte of interest because of its biological significance as a neurotransmitter in the central nervous system. Catechol was used as a starting point for the detection experiments since its reaction with chitosan has been better studied by Wu et al than that of dopamine [59, 60]. The procedures and reagents for the detection of phenol electrochemical oxidation were described in detail in Chapter 3. The following sections summarize the experimental results.

4.5.1 Catechol Detection

The initial catechol oxidation experiments were based on measurement in air. For this, a 100nm thick chitosan film is electrodeposited on a cantilever and the initial bending is measured with the Veeco NT1100 in PSI mode with its original illumination source. Next, the cantilever is used as the anode for electrochemical oxidation of catechol solution as described in Section 3.6. The cantilever is rinsed with DI water, dried, and its final bending is measured. Figure 4-22A shows the measurement results for multiple cantilevers before and after the oxidation; note that only bending at the tip is shown rather than a profile of the whole beam. The error bars in the figure are based on an estimated measurement error of 100nm due to humidity variations. On average, 800nm of

upward bending is caused by the catechol oxidation and chitosan crosslinking. Using Equations 2-17 and 2-18, the change in film stress estimated from this bending is 27MPa tensile.

The cantilever response to catechol oxidation was also measured in solution. A 300nm thick chitosan film is electrodeposited on a 130μm long cantilever, and the sample is immersed in DI water (note that in most other experiments 100μm long devices are used). The initial bending is measured with the Veeco NT1100, using the custom laser illumination source to enable measurements through the DI. Next, electrochemical oxidation of catechol solution is performed as described in Section 3.6 with the cantilever serving as anode. Finally, the cantilever is rinsed and immersed in fresh DI, and its bending is measured again. Figure 4-22B shows the measurement results for multiple cantilevers before and after the oxidation. The error bars are based on estimated error of 30nm, mainly caused by misalignment of the sample in the interferometer filed of view (as discussed in Section 4.3.1). On average, 500nm of upward bending is generated by the catechol oxidation and chitosan crosslinking. The associated change in chitosan film stress is estimated to be 3MPa tensile using Equations 2-17 and 2-18. Note that this stress is considerably less that the 27MPa estimated from Figure 4-22B for measurements air. The reason for the difference may be the electrostatic screening effect of water, which increases the length of crosslinks, swells the chitosan, and relieves the tensile film stress.

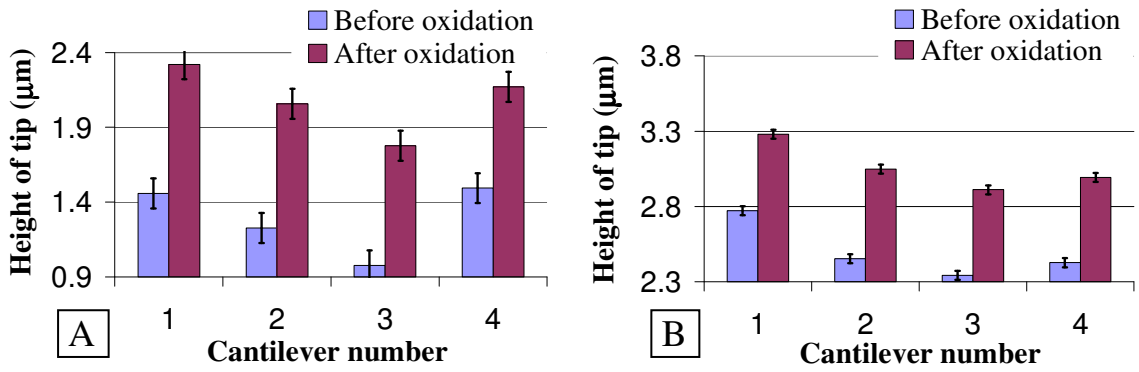

Figure 4-22. (A) Bending of cantilevers in response to electrochemical oxidation of catechol. The measurements are performed in air after drying the sample. (B) Bending of cantilevers in response to catechol oxidation, but with measurements performed in solution (DI water).

4.5.2 Dopamine Detection

After the successful mechano-transduction of catechol oxidation with chitosan-coated cantilevers, the response to dopamine oxidation in air and in solution was studied. The procedures followed in this case are essentially the same as those described previously for catechol, but the electrochemical oxidation step is performed in a dopamine solution. Figure 4-23A shows the results for bending measurements in air. The chitosan thickness in this case is 400nm, and the average cantilever bending upon dopamine oxidation is 1.7µm. Based on these values, the estimated chitosan film stress generated by the crosslinking is 14MPa.

Figure 4-23B shows results for cantilever bending measurements in solution (pure DI water). The chitosan thickness for this experiment is greatly increased (1.5µm) to generate measurable displacement upon dopamine oxidation. The differential cantilever bending caused by chitosan crosslinking is approximately 500nm; the change in film stress estimated from this value using Equations 2.17 and 2.18 is 1.2MPa tensile. This stress is considerably smaller than the 14MPa estimated from Figure 4-23A for measurements in air. Recall that a similar observation was made for catechol oxidation

experiments and was explained with the chitosan swelling in water. The same explanation should be applicable here. Note also that the measured chitosan stress due to catechol oxidation is greater than that due to dopamine oxidation for both in-air and in-solution experiments. This suggests that the chitosan crosslinking density for catechol oxidation exceeds that for dopamine oxidation.

Although the detection of dopamine oxidation in air produces larger bending signals than in solution, this approach is not applicable to living biological tissues. Drying the cantilever for measurements takes minutes, while dopamine release and uptake in nerve tissue occur on a time scale of seconds. Mechano-detection in solution has the potential to achieve the necessary temporal resolution. The experiments presented here involve electrochemical oxidation for at least 30s, thereby limiting the detection temporal response. However, the oxidation time was not optimized and was made excessively long to ensure that the chitosan is completely crosslinked. The detection response time can be greatly improved by decreasing the chitosan thickness and cantilever dimensions, and by minimizing the oxidation time.

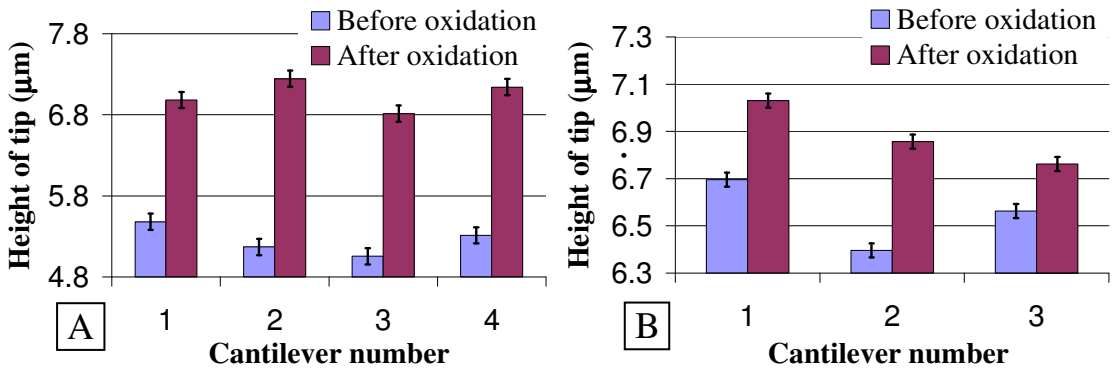

Figure 4-23. (A) Bending of cantilevers in response to electrochemical oxidation of dopamine. Measurements performed in air after drying sample (B) Bending of cantilevers in response to dopamine oxidation with measurements performed in solution (DI water).

4.5.3 Selective Detection of Dopamine vs. Ascorbic Acid

As discussed in Chapter 1, one of the common chemicals interfering with the detection of dopamine by traditional electrochemical techniques (cyclic voltammetry) is ascorbic acid. Here, it is demonstrated that the mechanical detection method with chitosan–coated cantilevers can successfully discriminate between ascorbic acid and dopamine. First, chemical evidence is provided that products generated from the electrochemical oxidation of dopamine can react with chitosan but not with ascorbic acid. These supporting experiments were carried out by Dr. Li-Qun Wu at the University of Maryland Biotechnology Institute (UMBI), and the results are reproduced here with permission. Next, the response of chitosan-coated cantilevers to the oxidation of dopamine and ascorbic acid is presented.

4.5.3.1 Supporting Experiments

Dr. Wu deposited chitosan on large (millimeter scale) electrodes and used them for oxidizing dopamine and ascorbic acid solutions. Control experiments with uncoated electrodes (no chitosan) were also performed. In each case, after the electrochemical oxidation the solution absorption spectrum was measured with a UV-Visible spectrophotometer (Genesys 2). The absorption results for dopamine are shown in Figure 4-24A, and those for ascorbic acid in Figure 4-24B. In (A), the solution's absorption is increased substantially at short wavelengths when dopamine is oxidized in the absence of chitosan. However, when dopamine is oxidized with the chitosan-coated electrode, the change in solution absorption is smaller by comparison. These results suggest that the dopamine oxidation products (which cause the increased absorption) react with chitosan if it is present and are consumed from the solution. In Figure 4-24B, the UV-Vis absorption of the ascorbic acid solution is increased by approximately the same amount

upon oxidation with and without chitosan. This suggests that the ascorbic acid oxidation products do not react with chitosan and remain in the solution.

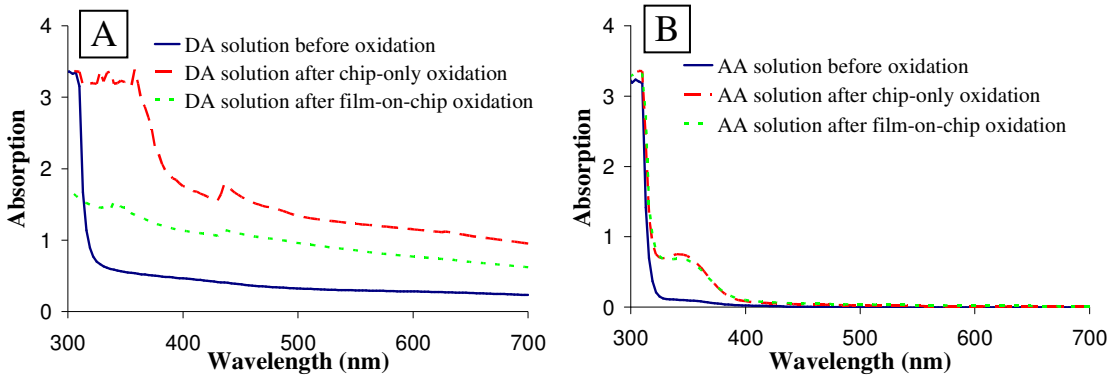

Figure 4-24. (A) UV-Visible absorption spectrum of dopamine (DA) solutions before electrochemical oxidation, after oxidation with a blank electrode (chip-only), and after oxidation with a chitosan-coated electrode (film-on-chip). (B) Absorption spectrum of ascorbic acid solutions before oxidation, after oxidation with blank electrode, and after oxidation with chitosan-coated electrode.

After measuring the absorption of the solution, the chitosan films (~30μm thick), were peeled from the electrodes, and their absorption was also measured. The chitosan film that had been incubated with dopamine was observed to be brown in color, and Figure 4-25 shows it has a broad UV-Vis spectrum. This suggests that the film was crosslinked. In contrast, the chitosan film incubated with ascorbic acid remained transparent, and the spectrum in Figure 4-25 shows little UV-Vis absorption of this film. Finally, the chitosan films were placed in an acidic solution of pH 3.5 (chitosan that is not crosslinked dissolves below pH of 6.5). The film incubated with dopamine was insoluble, suggesting that it was crosslinked; the film incubated with ascorbic acid dissolved. Together, these results provide chemical evidence that oxidation products of dopamine, but not ascorbic acid, react with the chitosan film.

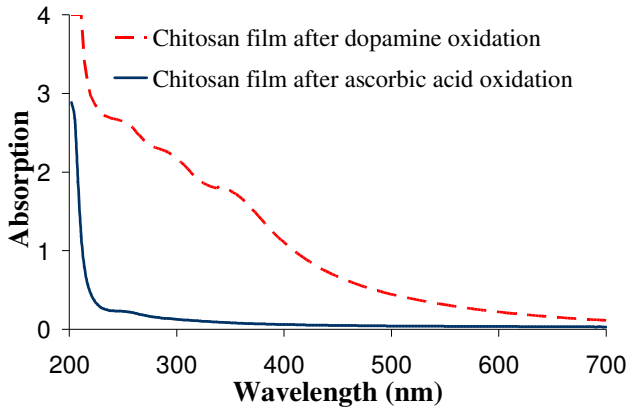

Figure 4-25. UV-Visible absorption spectra of chitosan films (30µm thick) after ascorbic acid oxidation and after dopamine oxidation. Chitosan exposed to ascorbic acid remains transparent, while chitosan exposed to dopamine has significantly increased absorption.

4.5.3.2 Cantilever Detection

This section presents bending results for chitosan-coated cantilevers in response to ascorbic acid oxidation and dopamine oxidation. A 1.5µm thick chitosan film is electrodeposited on a cantilever, and it is used as the anode for oxidation of ascorbic acid as described in Section 3.6. The sample is rinsed, immersed in DI water, and the cantilever bending is measured with the modified Veeco NT1100 through the DI. Next, the electrochemical oxidation is repeated with the *same* cantilever in dopamine solution, and the bending is measured again in the DI water. The measurement results are summarized in Figure 4-26. Note that the cantilever exhibits some initial bending due to residual stress in the chitosan film. Upon ascorbic acid oxidation (Figure 4-26A), the bending does not change much; the small shift observed is caused mainly by measurement error. Upon dopamine oxidation, the cantilever bends up by approximately 800nm due to the crosslinking of chitosan by the dopamine oxidation products. These results show that the device successfully discriminates between the oxidation of ascorbic acid and dopamine. As discussed in Chapter 1, purely electrochemical detection

techniques (e.g. cyclic voltammetry) cannot discriminate between the two analytes because of their similar oxidation potential.

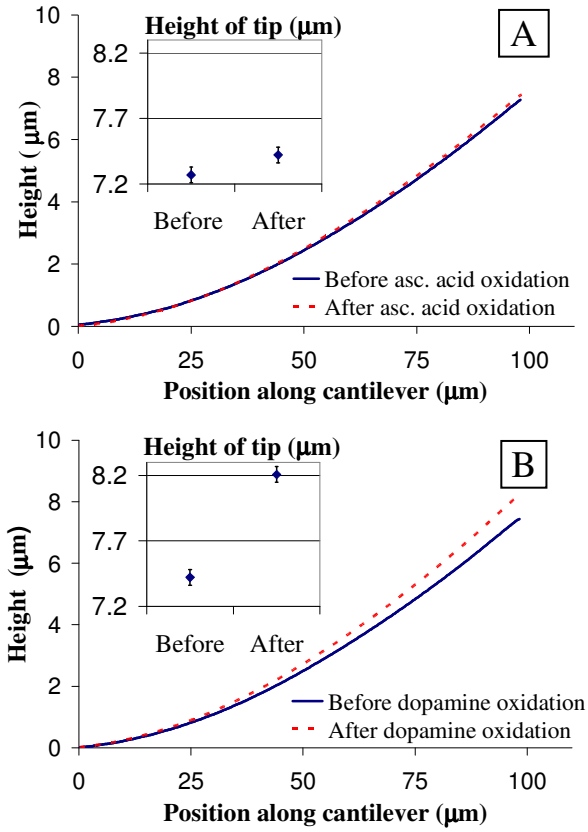

Figure 4-26. (A) Response of cantilever with chitosan to *ascorbic acid* electrochemical oxidation (measured in solution). The small bending at the tip is due to measurement error and nonspecific interactions. (B) Response of cantilever with chitosan to *dopamine* electrochemical oxidation (measured in solution). The cantilever bends up considerably (~800nm at the tip).

Figure 4-27 shows the results of multiple experiments with ascorbic acid oxidation followed by dopamine oxidation. Note that only displacement of the cantilever tip is given here instead of a complete cantilever profile. In each case, the dopamine oxidation produces significant bending, while the ascorbic acid oxidation produces bending within the measurement error bounds.

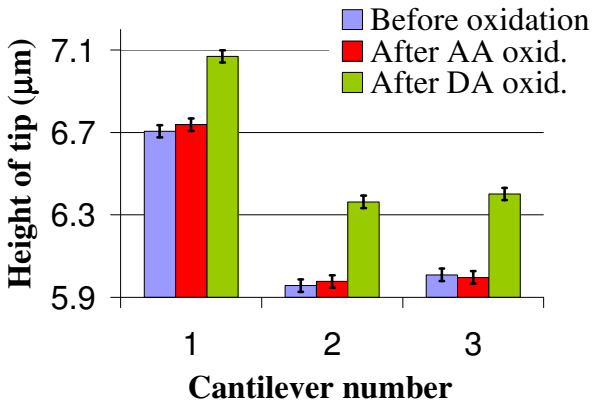

Figure 4-27. Response of chitosan-coated cantilevers to ascorbic acid oxidation and dopamine oxidation (measured in solution).

4.5.4 Limitations of Microcantilever Dopamine Detection

Note that real biological samples often contain both dopamine and ascorbic acid simultaneously with the concentration of ascorbic acid being higher [57, 87]. Currently, our method is not capable of detecting dopamine mixed with appreciable amounts of ascorbic acid; the dopamine oxidation products are reduced by the ascorbic acid and are not allowed to react with the chitosan. In experiments where the concentration of ascorbic acid was 10 times lower than that of dopamine, the chitosan crosslinking still occurred. However, when the two concentrations were comparable, no chitosan crosslinking was observed. Well-established electrochemical methods for dopamine detection such as fast-scan cyclic voltammetry are also impacted by the interference of ascorbic acid when it is present in dopamine samples [57].

4.6 Conclusion

This chapter presented the experimental results from testing of the microcantilever sensors with DNA and phenols (catechol and dopamine). First, the principle of operation of the optical interferometer used for measurements was described and the major sources of experimental error were discussed. Next, results of DNA hybridization detection in

both dynamic and static mode were presented. In dynamic mode, the measurements were performed in air after drying the devices; in static mode the measurements were performed in air or in liquid (using custom modifications of the optical interferometer).

Finally, phenol detection results with the microcantielver sensors in static mode were presented. The phenols catechol and dopamine were detected upon their electrochemical oxidation. The measurements were performed either in air after drying the device or in liquid. It was also shown that the microcantilever sensor can successfully discriminate between ascorbic acid and dopamine.

Chapter 5: Conclusion and Future Work

5.1 Conclusion

This thesis research has demonstrated the use of the polysaccharide chitosan as a bio-interface material for microcantilever sensors. The microcantilever sensors detect binding of biomolecules as a shift in resonant frequency (dynamic mode) or as differential bending (static mode). In comparison with other types of biosensors, such as optical, electrochemical, capacitive, or acoustic devices, microcantilever sensors have the combined advantages of label-free detection and small footprint. These characteristics make them attractive for portable, low-cost biodetection that requires minimal sample preparation (since no labeling of the analyte is required).

In this study, microcantilever sensors with chitosan for both static and dynamic mode of operation were designed, fabricated, and tested. Two demonstrations of detecting biochemical events were given. The first one is DNA hybridization; this is a conventional application for microcantilever sensors, and it has been previously demonstrated by a number of authors [28, 29, 31, 38]. The novelty here is the use of chitosan to attach probe DNA on the cantilever surface, while in previous studies it was attached by self-assembled monolayers (SAMs). The second demonstration is a new one, and it has not been investigated by others: mechano-detection of the neurotransmitter dopamine. Dopamine is typically detected by electrochemical techniques such as cyclic voltammetry [58]; here, it was shown that electrochemical oxidation of dopamine can be transduced by a chitosan-coated cantilever.

5.1.1 DNA Hybridization

The previously developed procedures for chitosan electrodeposition by Wu et al [49, 50] were adjusted here to allow for thin chitosan films (100nm) and small electrode sizes (40μm width) on the cantilevers. A miniaturized deposition setup using a micropositioning probe was developed for this purpose. The cantilevers were functionalized with probe DNA using procedures previously developed by Yi et al [52, 88], and hybridization with target DNA was detected from the cantilever response. This is the first demonstration of micromechanical detection of DNA hybridization with probes attached to chitosan.

Both dynamic and static cantilever sensor modes were explored for detecting the hybridization. Dynamic mode measurements were performed in air after drying the sample, while static mode measurements were taken both in air and in solution (DI water). The measurements in air were severely affected by humidity variations and, as a result, had large experimental error. Since the cantilever response in this project was large, the hybridization could still be detected despite the measurement error. However, to improve the detection limit, the humidity variation must be addressed. Two different approaches to this problem were explored here, and their feasibility was demonstrated (particularly for dynamic mode). One approach is based on nitrogen drying of the sample during measurements, and the other on using a reference cantilever to subtract the effect of humidity variations. Static mode measurements in solution exhibited much less experimental error than those in air as they are immune from humidity effects. To enable these in-solution experiments, custom modifications were made to the Veeco NT1100 interferometer used for measuring cantilever displacement.

The results from both static and dynamic mode testing showed the potential advantages of chitosan as a biointerface layer for microcantilever sensors. The estimated surface mass density of target DNA molecules bound to the chitosan was two orders of magnitude higher than that reported for studies using self-assembled monolayers (SAMs) as the interface. The estimated surface stress upon hybridization from the static mode measurements was also two orders of magnitude higher than that reported for DNA attached to SAMs. These results suggest that chitosan has a large effective surface area due to its polymeric network, which allows more biomolecules to be attached to the sensor surface than the SAMs interface. This property of chitosan has the potential to greatly increase the sensitivity of microcantilever biosensors, contributing to low-cost portable devices.

5.1.2 Dopamine Oxidation

The dopamine mechano-detection was motivated by previous studies by Wu et al [59, 60] showing that the electrochemical oxidation of some phenols crosslinks chitosan. For this work, chitosan was electrodeposited on cantilevers and their static mode bending was measured in response to dopamine oxidation (dopamine is a phenol). The crosslinking of chitosan caused a residual stress and cantilever displacement, thereby providing a detection mechanism for the dopamine electrochemical oxidation. The measurement results showed that the dopamine-induced crosslinking of chitosan produces film stress of approximately 2MPa when measured in solution and 14MPa when measured in air. It was demonstrated that ascorbic acid, which typically interferes with the detection of dopamine by cyclic voltammetry, does not react with the chitosan upon oxidation and does not generate measurable cantilever bending. Thus, the mechano-detection of

dopamine has improved selectivity in comparison to conventional electrochemical detection techniques.

5.2 Potential Improvements and Future Work

5.2.1 Arrayed Hybridization Sensors

When screening a sample for a large number of DNA sequences, it is necessary to use an array of hybridization sensors with different DNA probes. This idea has been implemented with printed microarrays based on fluorescence as described in Section 1.3.4. Multiple DNA probes are immobilized at different locations on a surface by printing of a self-assembled monolayer (SAM) interface. Complementary target DNA binds to the probe, causing a fluorescent signal at that location. Although this kind of arrays work well, they require the sample to be fluorescently labeled. A similar array can be potentially implemented with cantilever sensors instead, allowing for label-free detection. The problem, however, is that cantilever sensors are not compatible with printing of the SAM interface because they would easily break. Localizing the SAM on individual cantilevers therefore requires highly precise micromanipulators and is a prohibitively slow, expensive process.

The chitosan biointerface can be used to easily functionalize cantilever arrays because of its ability to be electrodeposited at specific locations. Chen et al [51] have demonstrated that chitosan can be conjugated with biomolecules before deposition instead of after the deposition. Multiple solutions of chitosan conjugated with different DNA probes can be prepared. An electrically addressable array of cantilevers can be exposed to the different chitosan solutions sequentially, biasing one cantilever for each solution. As a result, each cantilever would be functionalized with a different DNA probe.

The cantilevers can be integrated with microfluidic channels to deliver the solutions rapidly and minimize the required volume. Figure 5-1 shows a schematic for this concept. Each color of probe DNA on the cantilevers corresponds to a different sequence. This functionalization approach may still be slow due to the flushing of many different chitosan solutions. However, it does not require any high-precision micromanipulation, and it can be automated easily and cheaply.

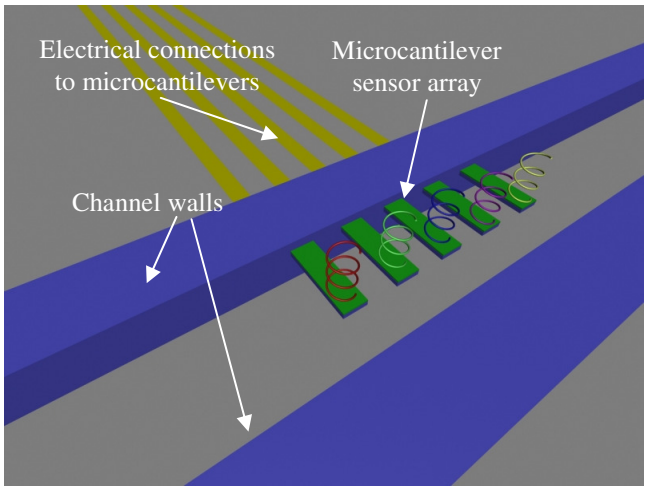

Figure 5-1. Conceptual microcantilever array device. A microfluidic channels delivers chitosan conjugated with probe molecules to the cantilevers. The chitosan is deposited only where a voltage is applied. This enables functionalization of each cantilever in the array with different probe biomolecules.

5.2.2 Integrated Displacement Sensors

The Veeco NT1100 interferometer used to measure cantilever bending in this project can only operate on one device at a time, and it takes almost 5 min to reposition the sample to measure another device. Clearly, large arrays of cantilevers as envisioned in the previous section would require a parallel measurement approach. One way to meet this requirement would be to integrate piezoresistive displacement sensors within the cantilevers. Figure 5-2 shows a design concept for such a "smart" cantilever. The device can be fabricated from an SOI wafer (Silicon On Insulator). Piezoresistors are implanted

near the base of the Si cantilever, where the largest stress is expected upon cantilever bending. The change in displacement is read out as a change in resistance of the piezoresistors. Metal is deposited on the cantilever to serve as the electrode for chitosan deposition and also to contact the piezoresistors. Note that the metal is isolated from the Si by SiO_2 to prevent chitosan from depositing on the bottom surface of the cantilever. Recall that static mode operation requires biomolecules to be present only one side of the cantilever to maximize surface stress. For measurements in solution, the metal contacts to the piezoresistors would have to be insulated to prevent leakage currents.

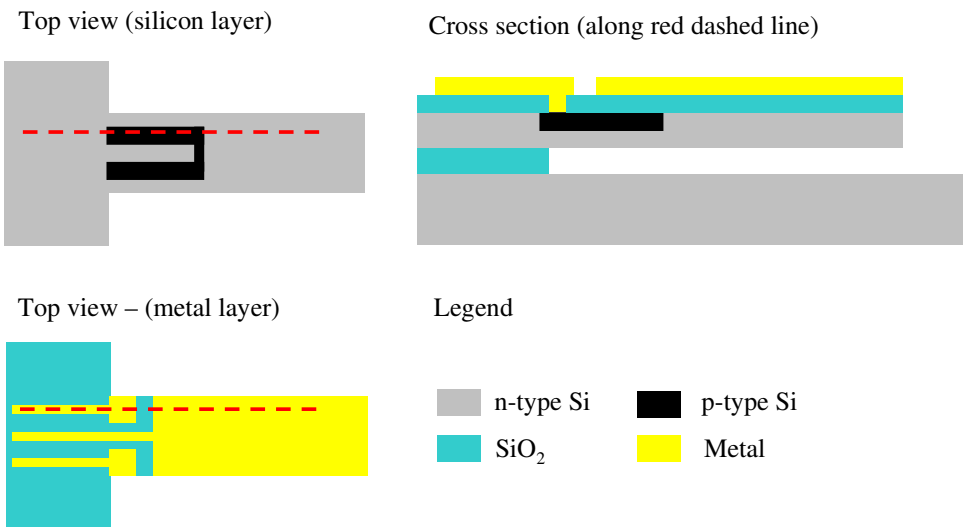

Figure 5-2. Top view and cross section schematics of proposed cantilever sensors with built-in piezoresistors.

Similar "smart cantilever" designs have been implemented by a number of authors [65, 89, 90]. Piezoresistive displacement sensors are not as accurate as optical measurement techniques (e.g. interferometry). However, considering the large displacements and resonant frequency shifts measured in this project due to the chitosan biointerface, these sensors are expected to have sufficient accuracy. In addition, the piezoresistive readout has some advantages over optical measurement, particularly for

experiments in solution. Piezoresistive sensors are not affected by the optical properties of the solution such as refractive index and attenuation. Also, they do not require accurate alignment with optical beams; recall that sample misalignment was one of the major sources of error in optical measurements for this project. Finally, the response of piezoresistive displacement sensors is expected to be real-time, allowing for accurate compensation of humidity variations as discussed in Section 4.3.3.

5.2.3 Dopamine Concentration Analysis

For DNA hybridization detection, the researcher typically needs to know whether a certain gene is expressed in the sample or not. Evaluating its concentration is not of critical importance. However, for dopamine detection, knowing the concentration of dopamine in the nerve tissue is essential to understanding its role. The cyclic voltammetry detection technique can give quantitative dopamine concentration data, provided there are no interfering chemicals (e.g. ascorbic acid). The micromechanical detection method demonstrated here determines the presence of dopamine but not its concentration; this is clearly a major limitation.

The mechano-detection of dopamine can be extended to determine concentration if temporally resolved cantilever displacement data are available. During electrochemical oxidation, dopamine reaches the anode by diffusion through the chitosan, and diffusion rate depends on concentration. Therefore, the rate of chitosan crossliking should depend on the concentration of dopamine in the solution. Consequently, the bending of the microcantilever sensor as a function of time should depend on dopamine concentration. The exact dependence can be calibrated empirically by performing experiments in dopamine solutions with different concentrations.

This approach was not pursued here because of the poor temporal resolution of displacement measurements. The electrochemical reaction changes the color of the solution near the cantilever; this causes severe optical measurement error. Therefore, the sample had to be rinsed and immersed in fresh DI water for each measurement, making it impossible to measure the displacement as a function of reaction time. However, the integrated piezoresistive sensor described in the previous section is insensitive to optical properties of the solution, and the cantilever displacement can be measured real-time. This could enable quantitative determination of the dopamine concentration with chitosan-coated microcantilevers.

Bibliography

[1] National Materials Advisory Board, "Microelectromechanical Systems: Advanced Materials and Fabrication Methods," *National Academy Press*, Washington, D.C., 1997.

[2] I. Amato, "May the Micro Force Be with You," *Techology Review*, September 1999.

[3] J. Bryzek and K. Petersen, "Micromachines on the March," *IEEE Spectrum*, pp. 20-31, May 1994.

[4] J. Hubner, K. B. Morgensen, A. M. Jorgensen, P. Friis, P. Tellman, and J. P. Kutter, "Integrated optical measurement system for fluorescence spectroscopy in microfluidic channels," *Review of Scientific Instruments*, vol. 72, no. 1, 2001.

[5] M. Hedstrom, I. Y. Galaev, and B. Mattiasson, "Continuous measurements of a binding reaction using a capacitive biosensor," *Biosensors and Bioelectronics*, vol. 21, pp. 41-48, 2005.

[6] A. Gupta, D. Akin, and R. Bashir, "Single virus particle mass detection using microresonators with nanoscale thickness," *Applied Physics Letters*, vol. 84, no. 11, 2004.

[7] X. Yu, T. Li, L. Hao, and D. Zhang, "PCR Microchip Array Based on Polymer Bonding Technique," *Transactions of the ASME*, vol. 127, pp. 38-42, March 2005.

[8] Y. Li, R. S. Shawgo, B. Tyler, P. T. Henderson, J. S. Vogel, A. Rosenberg, P. B. Storm, R. Langer, H. Brem, and M. J. Cima, "In vivo release from a drug delivery MEMS device," *Journal of Controlled Release*, vol. 100, pp. 211-219, 2004.

[9] J. Muthuswamy, M. Okandan, A. Gilletti, M. S. Baker, and T. Jain, "An Array of Microactuated Microelectrodes for Monitoring Single-Neuronal Activity in Rodents," *IEEE Transactions on Biomedical Engineering*, vol. 52, no. 8, 2005.

[10] A. D. McNaught and A. Wilkinson, *IUPAC Compendium of Chemical Terminology*. Cambridge, UK: Royal Society of Chemistry, 1997.

[11] S. Balslev, B. Bilenberg, O. Geschke, A. M. Jorgensen, A. Kristensen, J. P. Kutter, K. B. Mogensen, D. Snakenborg, "Fully Integrated Optical System for Lab-on-a-Chip Applications", *17th IEEE International Conference on Micro Electro Mechanical Systems*. Maastricht, 2004.

[12] M. A. Powers, S. T. Koev, A. Schleunitz, H. Yi, V. Hodzic, W. E. Bentley, G. F. Payne, G. W. Rubloff, and R. Ghodssi, "A Fabrication Platform for Electrically Mediated Optically Active Biofunctionalized Sites in BioMEMS," *Lab on a Chip*, vol. 5, pp. 583-586, 2005.

[13] L.-Q. Li and L. M. Davis, "Single photon avalanche diode for single molecule detection," *Review of Scientific Instruments*, vol. 64, pp. 1524-1529, 1993.

[14] R. Wang, M. Minunni, S. Tombelli, and M. Mascini, "A new approach for the detection of DNA sequences in amplified nucleic acids by a surface plasmon resonance biosensor," *Biosensors and Bioelectronics*, vol. 20, pp. 598-605, 2004.

[15] S. Y. Wu, H. P. Ho, W. C. Law, and C. Lin, "Highly sensitive differential phase-sensitive surface plasmon resonance biosensor based on the Mach–Zehnder configuration," *Optics Letters*, vol. 29, no. 20, 2004.

[16] K. Kerman, M. Kobayashi, and E. Tamiya, "Recent trends in electrochemical DNA biosensor technology," *Measurement Science and Technology*, vol. 15, pp. R1-R11, 2004.

[17] E. Komarova, M. Aldissi, and A. Bogomolova, "Direct electrochemical sensor for fast reagent-free DNA detection," *Biosensors and Bioelectronics*, vol. 21, pp. 182-189, 2005.

[18] W. A. Wlassoff and G. C. King, "Ferrocene conjugates of dUTP for enzymatic redox labelling of DNA," *Nucleic Acids Research*, vol. 30, no. 12, 2002.

[19] M. J. Schoning, M. Arzdorf, P. Mulchandani, W. Chen, and A. Mulchandani, "A capacitive field-effect sensor for the direct determination of organophosphorus pesticides," *Sensors and Actuators B*, vol. 91, pp. 92-97, 2003.

[20] E. A. Moschou and N. A. Chaniotakis, "Ion-Partitioning Bulk Membrane CHEMFET as Highly Sensitive Calcium Probe," *Electroanalysis*, vol. 15, no. 15-16, 2003.

[21] K. Lange, G. Blaess, A. Voigt, M. Rapp, E. Hansjosten, U. Schygulla, "Packaging of Surface Acoustic Wave (SAW) based Biosensors: an Important Issue for Future Biomedical Applications", IEEE International Ultrasonics, Ferroelectrics, and Frequency Control Joint 50th Anniversary Conference, 2004

[22] G. Kim, W. Chong, S. Kim, K. Kim, S. Jeong, T. Kwon, N. Kim, C. Hong, "Development of Biosensor Using Surface Acoustic Wave", *The 30th Annual Conference of the IEEE Industrial Electronics Society.* Busan, Korea, November 2 - 6, 2004.

[23] F. Shen, K. H. Lee, S. J. O'Shea, P. Lu, and T. Y. Ng, "Frequency Interference Between Two Quartz Crystal Microbalances," *IEEE Sensors Journal*, vol. 3, no. 3, 2003.

[24] T. H. Ha, S. Kim, G. Lim, and K. Kim, "Influence of liquid medium and surface morphology on the response of QCM during immobilization and hybridization of short oligonucleotides," *Biosensors and Bioelectronics*, vol. 20, pp. 378-389, 2004.

[25] Y. K. Hong, H. Park, S. Q. Lee, K. S. Moon, M. Levy, "Fabrication of a piezoelectric biosensor based on a PZN-PT/PMN-PT single crystal thin film", *SPIE International Conference on Opto-mechatronic Actuators, Sensors and Control*, vol. 5602, pp. 140-147. Philadelphia, USA, 2004.

[26] G. Wu, H. Ji, K. Hansen, T. Thundat, R. Datar, R. Cote, M. F. Hagan, A. K. Chakraborty, and A. Majumdar, "Origin of nanomechanical cantilever motion generated from biomolecular interactions," *PNAS*, vol. 98, no. 4, 2001.

[27] J. Fritz, M. K. Baller, H. P. Lang, H. Rothuizen, P. Vettiger, E. Meyer, H.-J. Guntherodt, C. Gerber, and J. K. Gimzewski, "Translating Biomolecular Recognition into Nanomechanics," *Science*, vol. 288, pp. 316-318, 2000.

[28] M. Alvarez, L. G. Carrascosa, M. Moreno, A. Calle, A. Zaballos, L. M. Lechuga, C. Martinez-A, and J. Tamayo, "Nanomechanics of the Formation of DNA Self-Assembled Monolayers and Hybridization on Microcantilevers," *Langmuir*, vol. 20, pp. 9663-9668, 2004.

[29] M. Su, S. Li, and V. P. Dravid, "Microcantilever resonance-based DNA detection with nanoparticle probes," *Applied Physics Letters*, vol. 82, no. 20, 2003.
[30] B. Illic, D. Czaplewski, H. G. Craighead, P. Neuzil, C. Campagnolo, and C. Batt, "Mechanical resonant immunospecific biological detector," *Applied Physics Letters*, vol. 77, no. 3, 2000.
[31] R. McKendry, J. Zhang, Y. Arntz, T. Strunz, M. Hegner, H. P. Lang, M. K. Baller, U. Certa, E. Meyer, H.-J. Guntherodt, and C. Gerber, "Multiple label-free biodetection and quantitative DNA-binding assays on a nanomechanical cantilever array," *PNAS*, vol. 99, no. 15, 2002.
[32] K. Y. Gfeller, N. Nugaeva, and M. Hegner, "Micromechanical oscillators as rapid biosensor for the detection of active growth of Escherichia coli," *Biosensors and Bioelectronics*, vol. 21, pp. 528-533, 2005.
[33] H. P. Lang, M. Hegner, E. Meyer, and C. Gerber, "Nanomechanics from atomic resolution to molecular recognition based on atomic force microscopy technology," *Nanotechnology*, vol. 13, pp. R29-R36, 2002.
[34] F. J. Norton, US Patent Number 2307800, 1943
[35] H. C. Nathanson, W. E. Newell, R. A. Wickstrom, and J. R. Davis, "The Resonant Gate Transistor," *IEEE Transactions on Electron Devices*, vol. 14, no. 3, 1967.
[36] I. Amato, "New Chemical Lows in Brain Surveillance," *Chemical and Engineering News*, vol. 84, no. 8, pp. 12-15, 2006.
[37] N. V. Lavrik, M. J. Sepniak, and P. G. Datskos, "Cantilever Transducers as a Platform for Chemical and Biological Sensors," *Review of Scientific Instruments*, vol. 75, no. 7, pp. 2229-2253, 2004.
[38] X. R. Zhang and X. Xu, "Development of a biosensor based on laser-fabricated polymer microcantilevers," *Applied Physics Letters*, vol. 85, no. 12, 2004.
[39] R. T. Howe and R. S. Muller, "Resonant-Microbridge Vapor Sensor," *IEEE Transactions on Electron Devices*, vol. 33, no. 4, 1986.
[40] B. Cunningham, M. Weinberg, J. Pepper, C. Clapp, R. Bousquet, B. Hugh, R. Kant, C. Daly, and E. Hauser, "Design, fabrication and vapor characterization of a microfabricated flexural plate resonator sensor and application to integrated sensor arrays," *Sensors and Actuators B*, vol. 73, no. 2-3, 2001.
[41] D. Strembicke, A. M. Robinson, F. E. Venneulen, M. Seto, K. B. Brown, "Humidity Measurement Using Resonating CMOS Microcantilever Structures", *Proceedings of the 1999 IEEE Canadian Conference on Electrical and Computer Engineering*. Edmonton, Alberta, Canada, 1999.
[42] T. Thundat, E. A. Wachter, S. L. Sharp, and R. J. Warmack, "Detection of mercury vapor using resonating microcantilevers," *Appl. Phys. Lett.*, vol. 66, no. 13, 1995.
[43] B. Illic, D. Czaplewski, M. Zalalutdinov, H. G. Craighead, P. Neuzil, C. Campagnolo, and C. Batt, "Single cell detection with micromechanical oscillators," *J. Vac. Sci. Techol.*, vol. 19, no. 6, 2001.
[44] F. Schreiber, "Self-assembled monolayers: from 'simple' model systems to biofunctionalized interfaces," *J. Phys.: Condens. Matter*, vol. 16, pp. R881-R900, 2004.
[45] B. Michel, A. Bernard, A. Bietsch, E. Delamarche, M. Geissleer, D. Juncker, H. Kind, J.-P. Reanult, H. Rothuizen, H. Schmid, P. Schmidt-Winkel, R. Stutz, and

H. Wolf, "Printing meets lithography: Soft approaches to high-resolution patterning," *IBM J. Res. & Dev.*, vol. 45, no. 5, 2001.

[46] R. S. Kane, S. Takayama, E. Ostuni, D. E. Ingber, and G. M. Whitesides, "Patterning proteins and cells using soft lithography," *Biomaterials*, vol. 20, pp. 2363-2376, 1999.

[47] Sigma Aldrich Inc., "Chitosan - A Technologically Important Biomaterial", http://www.sigmaaldrich.com/img/assets/3900/Chitosan.pdf, Accessed: Apr 26, 2006.

[48] R. Fernandes, L.-Q. Wu, T. Chen, H. Yi, S. Li, G. W. Rubloff, R. Ghodssi, W. E. Bentley, and G. F. Payne, "Electrochemically-Induced Deposition of a Polysaccharide Hydrogel onto a Patterned Surface," *Langmuir*, vol. 19, pp. 4058-62, 2003.

[49] L.-Q. Wu, A. P. Gadre, H. Yi, M. J. Kastantin, G. W. Rubloff, W. E. Bentley, G. F. Payne, and R. Ghodssi, "Voltage-Dependent Assembly of the Polysaccharide Chitosan onto an Electrode Surface," *Langmuir*, vol. 18, pp. 8620-25, 2002.

[50] L.-Q. Wu, H. Yi, S. Li, G. W. Rubloff, W. E. Bentley, R. Ghodssi, and G. F. Payne, "Spatially-Selective Deposition of a Reactive Polysaccharide Layer onto a Patterned Template," *Langmuir*, vol. 19, pp. 519-524, 2003.

[51] T. Chen, D. A. Small, L.-Q. Wu, G. W. Rubloff, R. Ghodssi, R. Vazquez-Duhalt, W. E. Bentley, and G. F. Payne, "Nature-Inspired Creation of Protein-Polysaccharide Conjugate and Its Subsequent Assembly onto a Patterned Surface," *Langmuir*, vol. 19, pp. 9382-9386, 2003.

[52] H. Yi, L.-Q. Wu, R. Ghodssi, G. W. Rubloff, G. F. Payne, and W. E. Bentley, "A Robust Technique for Assembly of Nucleic Acid Hybridization Chips based on Electrochemically Templated Chitosan," *Analytical Chemistry*, vol. 76, pp. 365-372, 2004.

[53] M. J. Kastantin, S. Li, A. P. Gadre, L.-Q. Wu, G. W. Rubloff, W. E. Bentley, G. F. Payne, and R. Ghodssi, "Integrated Fabrication of Polymeric Devices for Biological Applications," *Sensors and Materials*, vol. 15, pp. 295-311, 2003.

[54] J. D. Watson and F. H. C. Crick, "A structure for Deoxyribose Nucleic Acid," *Nature*, vol. 171, pp. 737-738, 1953.

[55] http://en.wikipedia.org/wiki/DNA, Accessed: Apr 26, 2006

[56] P. O. Brown and D. Botstein, "Exploring the new world of the genome with DNA microarrays," *Nature Genetics Supplement*, vol. 21, January 1999.

[57] B. J. Venton and R. M. Wightman, "Psychoanalytical electrochemistry: dopamine and behavior," *Analytical Chemistry*, vol. 75, pp. 414A-421A, 2003.

[58] V. Beni, M. Ghita, and D. W. M. Arrigan, "Cyclic and pulse voltammetric study of dopamine at the interface between two immiscible electrolyte solutions," *Biosensors and Bioelectronics*, vol. 20, pp. 2097–2103, 2005.

[59] L.-Q. Wu, M. K. McDermott, R. Ghodssi, and G. F. Payne, "Mimicking Biological Phenol Reaction Cascades to Confer Mechanical Function," *Advanced Functional Materials, In Press*, 2006.

[60] L.-Q. Wu, R. Ghodssi, Y. A. Elabd, and G. Payne, "Biomimetic Pattern Transfer," *Advanced Functional Materials*, vol. 15, pp. 189-195, 2005.

[61] M. Gad-el-Hak, *The MEMS Handbook*. Boca Raton, FL: CRC Press, 2002.

[62] M. J. Madou, *Fundamentals of microfabrication: the science of miniaturization*, Second ed. Boca Raton, FL: CRC Press, 2002.
[63] Y. Mitsuoka, T. Niwa, S. Ichihara, K. Kato, H. Muramatsu, K. Nakajima, M. Shikida, and K. Sato, "Microfabricated silicon dioxide cantilever with subwavelength aperture," presented at 6th International Conference on Near-Field Optics and Related Techniques, Enschede, Netherlands, 2001.
[64] A. Chand, M. B. Viani, T. E. Schaffer, and P. K. Hansma, "Microfabricated small metal cantilevers with silicon tip for atomic force microscopy," *Journal of Microelectromechanical Systems*, vol. 9, no. 1, 2000.
[65] P. A. Rasmussen, J. Thaysen, O. Hansen, S. C. Eriksen, and A. Boisen, "Optimised cantilever biosensor with piezoresistive read-out," *Ultramicroscopy*, vol. 97, pp. 371-376, 2003.
[66] E. Forsen, G. Abadal, S. Ghatnekar-Nilsson, J. Teva, J. Verd, R. Sandberg, W. Svendsen, F. Perez-Murano, J. Esteve, E. Figueras, F. C. Campabadal, L. Montelius, N. Barniol, and A. Boisen, "Ultrasensitive mass sensor fully integrated with complementary metal-oxide-semiconductor circuitry," *Applied Physics Letters*, vol. 87, no. 043507, 2005.
[67] C. Kocabas and A. Aydinli, "Design and Analysis of an Integrated Optical Sensor for Scanning Force Microscopies," *IEEE Sensors Journal*, vol. 5, no. 3, 2005.
[68] M. W. Pruessner, N. Siwak, K. Amarnath, S. Kanakaraju, W.-H. Chuang, and R. Ghodssi, "End-coupled optical waveguide MEMS devices in the indium phosphide material system," *Journal of Micromechanics and Microengineering*, vol. 16, pp. 832-842, 2006.
[69] M. Helm, J. J. Servant, F. Saurenbach, and R. Berger, "Read-out of micromechanical cantilever sensors by phase shifting interferometry," *Applied Physics Letters*, vol. 87, no. 064101, 2005.
[70] J. C. Wyant, "White Light Interferometry", *Aerosense Conference*, Orlando, FL, April 1-5, 2002.
[71] S. D. Senturia, *Microsystem Design*. Boston: Kluwer Academic Publishers, 2001.
[72] S. A. Smee, M. Gaitan, D. B. Novotny, Y. Joshi, and D. L. Blackburn, "IC Test Structures for Multilayer Interconnect Stress Determination," *IEEE Electron Device Letters*, vol. 21, no. 1, 2000.
[73] Y. Zhang, Q. Ren, and Y.-p. Zhao, "Modelling analysis of surface stress on a rectangular cantilever beam," *J. Phys. D: Appl. Phys.*, vol. 37, pp. 2140-2145, 2004.
[74] G. G. Stoney, *Proc. R. Soc. London*, vol. 82, pp. 172, 1909.
[75] N. S. Nise, *Control Systems Engineering*, 3rd ed. New York: John Wiley & Sons, Inc., 2000.
[76] M. Arps and A. Markwitz, "Improved current-voltage characteristics of downstream plasma enhanced chemical vapor deposition SiN deposited at low temperature by using He as a dilution gas," *J. Vac. Sci. Techol. A*, vol. 15, no. 4, 1997.
[77] C. Zhang, G. Xu, and Q. Jiang, "Characterization of the squeeze film damping effect on the quality factor of a microbeam resonator," *Journal of Micromechanics and Microengineering*, vol. 14, pp. 1302-1306, 2004.

[78] J. Arcamone, G. Rius, G. Abadal, J. Teva, N. Barniol, and F. Pe´rez-Murano, "Micro/nanomechanical resonators for distributed mass sensing with capacitive detection," *Microelectronic Engineering*, vol. 83, pp. 1216-1220, 2006.

[79] N. E. Jenkins, L. P. DeFlores, J. Allen, T. N. Ng, S. R. Garner, S. Kuehn, J. M. Dawlaty, and J. A. Marohna, "Batch fabrication and characterization of ultrasensitive cantilevers with submicron magnetic tips," *J. Vac. Sci. Techol. B*, vol. 22, no. 3, 2004.

[80] M. Calleja, J. Tamayo, A. Johansson, P. Rasmussen, L. Lechuga, and A. Boisen, "Polymeric Cantilever Arrays for Biosensing Applications," *Sensor Letters*, vol. 1, no. 1, 2003.

[81] Transene Inc, "Semiconductor and Thin Film Etchants for Microelectronic Circuits", http://www.transene.com/etchants.html, Accessed: Jun 10, 2006

[82] K. R. Williams, K. Gupta, and M. Wasilik, "Etch Rates for Micromachining Processing - Part II," *Journal of Microelectromechanical Systems*, vol. 12, no. 6, 2003.

[83] K. R. Williams and R. S. Muller, "Etch Rates for Micromachining Processes," *Journal of Microelectromechanical Systems*, vol. 5, no. 4, 1996.

[84] W.-H. Chuang, T. Luger, R. K. Fettig, and R. Ghodssi, "Mechanical Property Characterization of LPCVD Silicon Nitride Thin Films at Cryogenic Temperatures," *JOURNAL OF MICROELECTROMECHANICAL SYSTEMS*, vol. 13, no. 5, 2004.

[85] Y.-J. Tan, "Studying Non-uniform Electrodeposition Using the Wire Beam Electrode Method," *Journal of Modern Physics B*, vol. 16, no. 1&2, 2001.

[86] J. T. Hachman, J. J. Kelly, and A. C. West, US Patent Number 6802950, 2004

[87] L. Zhang and X. Jiang, "Attachment of gold nanoparticles to glassy carbon electrode and its application for the voltammetric resolution of ascorbic acid and dopamine," *Journal of Electroanalytical Chemistry*, no. 583, pp. 292-299, 2005.

[88] H. Yi, L.-Q. Wu, R. Ghodssi, G. F. Payne, and W. E. Bentley, "Signal-Directed Sequential Assembly of Biomolecules onto Patterned Surfaces," *Langmuir*, vol. 21, pp. 2104-2107, 2005.

[89] H. Sone, A. Ikeuchi, T. Izumi, H. Okano, and S. Hosaka, "Femtogram Mass Biosensor Using Self-Sensing Cantilever for Allergy Check," *Japanese Journal of Applied Physics*, vol. 45, no. 3B, pp. 2301-2304, 2006.

[90] A. Johansson, M. Calleja, P. A. Rasmussen, and A. Boisen, "SU-8 cantilever sensor system with integrated readout," *Sensors and Actuators A*, vol. 123-124, pp. 111-115, 2005.